Vertical Carrier Transport Properties and Device Application of InAs/$InAs_{1-x}Sb_x$ Type-II Superlattice and a Water-Soluble Lift-Off Technology

by

Cheng-Ying Tsai

A Dissertation Presented in Partial Fulfillment
of the Requirements for the Degree
Doctor of Philosophy

Approved November 2020 by the
Graduate Supervisory Committee:

Yong-Hang Zhang, Chair
Dragica Vasileska
Shane Johnson
Yuji Zhao

ARIZONA STATE UNIVERSITY

December 2020

ABSTRACT

The first part of this dissertation reports the study of the vertical carrier transport and device application in InAs/$InAs_{1-x}Sb_x$ strain-balanced type-II superlattice. It is known that the low hole mobility in the InAs/$InAs_{1-x}Sb_x$ superlattice is considered as the main reason for the low internal quantum efficiency of its mid-wave and long-wave infrared photodetectors, compared with that of its HgCdTe counterparts. Optical measurements using time-resolved photoluminescence and steady-state photoluminescence spectroscopy are implemented to extract the diffusion coefficients and mobilities of holes in the superlattices at various temperatures from 12 K to 210 K. The sample structure consists of a mid-wave infrared superlattice absorber region grown atop a long-wave infrared superlattice probe region. An ambipolar diffusion model is adopted to extract the hole mobility. The results show that the hole mobility first increases from 0.2 cm^2/Vs at 12 K and then levels off at ~50 cm^2/Vs as the temperature exceeds ~60 K. An InAs/$InAs_{1-x}Sb_x$ type-II superlattice nBn long-wavelength barrier infrared photodetector has also been demonstrated with a measured dark current density of 9.5×10^{-4} A/cm^2 and a maximum resistance-area product of 563 Ω-cm^2 at 77 K under a bias of -0.5 V. The Arrhenius plot of the dark current density reveals a possible high-operating-temperature of 110 K.

The second part of the dissertation reports a lift-off technology using a water-soluble sacrificial MgTe layer grown on InSb. This technique enables the seamless integration of materials with lattice constants near 6.5 Å, such as InSb, CdTe, PbTe, HgTe and Sn. Coherently strained MgTe with a lattice constant close to 6.5 Å acts as a sacrificial layer which reacts with water and releases the film above it. Freestanding CdTe/$Mg_xCd_{1-x}Te$

double-heterostructures resulting from the lift-off process show increased photoluminescence intensity due to enhanced extraction efficiency and photon-recycling effect. The lifted-off thin films show smooth and flat surfaces with 6.7 Å root-mean-square roughness revealed by atomic-force microscopy profiles. The increased photoluminescence intensity also confirms that the CdTe/$Mg_xCd_{1-x}Te$ double-heterostructures maintain the high optical quality after epitaxial lift-off.

ACKNOWLEDGMENTS

I would like to thank my advisor Dr. Yong-Hang Zhang for his guidance and supervision in my research topic and funding to support my scientific experiments. I have benefited significantly from his knowledge in physics and the way he thinks and approaches he adopts for problem solving. His vision toward semiconductor area inspires me to think widely and have a big picture in my research. I also would like to thank Dr. Shane Johnson for sharing his valuable knowledge in molecular beam epitaxy and helping the growers with machine maintenance, and Dr. Michael Goryll and Dr. Yuji Zhao for being my committee members and their advice for my research. Special thanks to Dr. Dragica Vasileska for her valuable inputs on the simulation of vertical carrier transport.

I would like to thank my seniors and previous group members, Dr. Yang Zhang, Dr. Preston Webster, Dr. Xin-Hao Zhao, Dr. Zhaoyu He, Dr. Jacob Becker, Dr. Calli Campbell, and Dr. Maxwell Lassise for guiding and training me to become a capable MBE grower and an independent researcher. I would also like to thank current group members, Stephen Schaefer, Jia Ding, Tyler McCarthy, and Zheng Ju for their helps in material characterization, MBE growth, and machine maintenance.

I would like to thank the ASU NanoFab staff, Kevin Hilgers, Kevin Norquist, Arthur Handugan, Jaime Quintero, Carrie Sinclair, and Scott Ageno who have provided professional semiconductor processes, mask design, and valuable discussions.

Finally, I am grateful to my parents for their endless love and supports throughout my graduate study.

This work was financially supported partially by Center for Semiconductor Modeling at the Boston University and the U.S. Army Research Laboratory (Grant No. W911NF-18-2-0027), the U.S. Army Research Office (Grant No. W911NF-10-1-0524 and W911NF-19-1-0277), and Northrop Grumman Corporation. I also acknowledge the use of high-resolution X-ray diffraction system in the LeRoy Eyring Center for Solid State Science at Arizona State University.

TABLE OF CONTENTS

Page

CHAPTER Page

LIST OF TABLES

Table Page

LIST OF FIGURES

Figure Page

Figure Page

Figure Page

Figure Page

Figure Page

LIST OF ACRONYMS

DH – double-heterostructure

ELO – epitaxial lift-off

IR – infrared

LWIR – long-wave infrared

LWSL – long-wave infrared superlattice

MWIR – mid-wave infrared

MWSL – mid-wave infrared superlattice

MBE – molecular beam epitaxy

MQW – multiple-quantum well

SL – superlattice

SSPL – steady-state photoluminescence

TRPL – time-resolved photoluminescence

T2SL – type-II superlattice

XRD – X-ray diffraction

1. INTRODUCTION

1.1 Background

Since the invention of semiconductor heterostructures [1] and superlattices (SL) [2], many scientific research and technology applications have been developed based on the wide variety of possible band alignments. These structures enable such as high electron mobility transistors (HEMTs), light-emitting diodes (LEDs), quantum cascade lasers (QCLs), interband cascade lasers (ICLs), quantum-well infrared photodetectors (QWIPs) [3], and solar cells. All of these types of devices were made possible by epitaxial growth techniques including molecular beam epitaxy (MBE) [4] and metal-organic chemical vapor deposition (MOCVD).

In order to obtain high quality and dislocation-free epitaxial films, lattice-matching of the grown films to the substrate is required. From the bandgap vs. lattice constant diagram shown in Figure 1, one can see that there is always a commercially available substrate for a group of lattice-matched binaries. For example, ZnTe and CdSe can be grown atop InAs or GaSb substrates since each features a lattice constant around 6.1 Å. Also, another notable group is CdTe, MgTe, and HgTe which can all be grown on InSb substrate with a lattice constant around 6.5 Å. As a result of this heterovalent epitaxial growth, the monolithic integration of III-V, II-VI, and even IV-VI semiconductors becomes achievable, offering desirable band alignment or bandgap energy for a particular device design. It is important to note that due to different electron configurations between IV, II-VI and III-V compound semiconductors, a heterovalent interface will have some interesting properties such as

electrical field induced topological insulator, which was predicted by Alex Zunger's team at the University of Colorado, Boulder [5].

The direct bandgap property in most of the III-V and II-VI materials makes them favorable for high efficiency optoelectronics device because of their large absorption coefficients. Also shown in Figure 1, the optoelectronics device based on III-V and II-VI materials can operate in many spectral ranges from ultra-violet (UV) to infrared (IR) by using GaN and InSb, respectively. Although ternary III-V and II-VI alloys can provide wide, continuous spectral range, the challenge is also the commercially available substrate

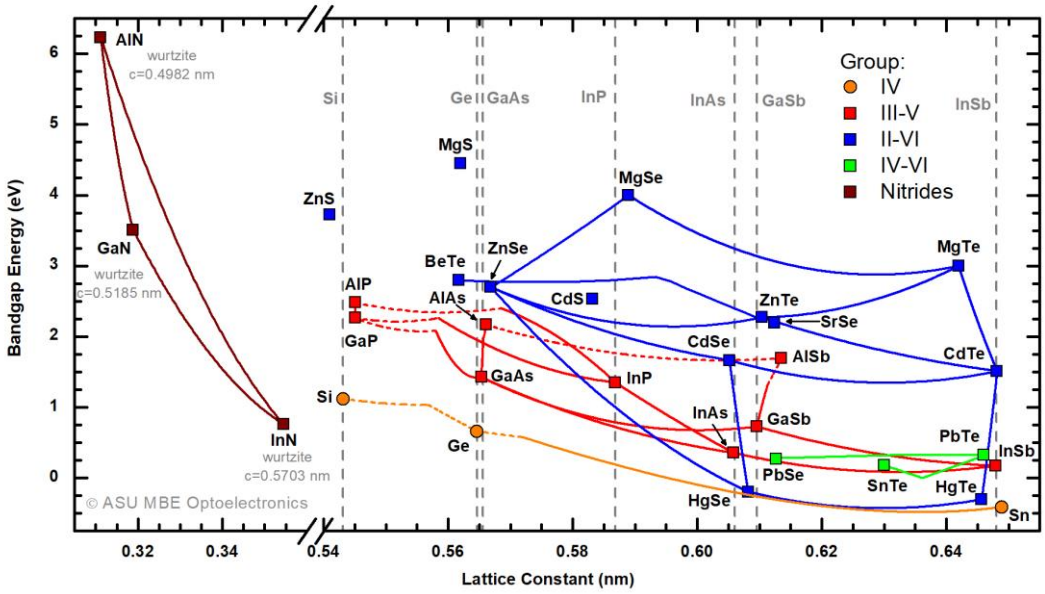

Figure 1. Bandgap energy vs. lattice constants diagram. The dashed grey line indicates the corresponding lattice constants of commercially available substrates, on which a group of lattice-matched binaries can be grown epitaxially.

due to limited choice of lattice constant, which makes the optoelectronics device designers difficult to find materials with desired bandgap and band offset for their applications.

1.2 Infrared Photodetector Technology

Infrared (IR) radiation is defined as electromagnetic radiation with wavelength longer than 780 nm up to 1 mm. Different wavelength range can be categorized into the followings: (1) near infrared (NIR), 0.78 μm to 1 μm; (2) short-wavelength infrared (SWIR), 1 μm to 3 μm; (3) mid-wavelength infrared (MWIR), 3 μm to 8 μm; (4) long-wavelength infrared (LWIR), 8 μm to 15 μm; (5) very long-wavelength infrared (VLWIR), 15 μm to 30 μm; (6) Far infrared (FIR), 30 μm to 100 μm; (7) submillimeter (SubMM), 100 μm to 1000 μm. Every object emits IR radiations due to the vibration of atoms when the ambient temperature is greater than 0 K. The radiation intensity and its spectral distribution are predicted by Plank's law, which describes the spectral density of radiation per unit wavelength per unit area from a blackbody in thermal equilibrium at a certain temperature. The Plank's law is formulated in the followings:

$$B_\lambda(\lambda, T) = \frac{2\pi hc^2}{\lambda^5} \frac{1}{e^{hc/\lambda kT} - 1} \ (Wcm^{-2}\mu m^{-1}) \tag{1}$$

$$B_p(\lambda, T) = \frac{2\pi c}{\lambda^4} \frac{1}{e^{hc/\lambda kT} - 1} \ (photons\ s^{-1}cm^{-2}\mu m^{-1}), \tag{2}$$

where λ is the wavelength, T is the temperature, h is the Plank's constant, c is the speed of light, and k is the Boltzmann's constant. From equations (1) and (2), as temperature increases, the total amount of energy emitted at any wavelength increases while the wavelength of peak emission decreases, which is given by the Wien displacement law:

$$\lambda_{mw}T = 2898\ (\mu m\ K) \quad \text{For maximum energy} \quad (3)$$

$$\lambda_{mp}T = 3670\ (\mu m\ K) \quad \text{For maximum photons.} \quad (4)$$

The sun is a perfect example of blackbody at 6000 K at which it emits a continuous spectrum with a peak at visible light. For the object at ambient temperature of 300 K, λ_{mw} and λ_{mp} are at 9.66 and 12.2 μm, respectively. Therefore, the use of LWIR photodetectors with cut-off wavelength longer than 13 μm is needed to see room temperature object without illuminating light.

IR photodetector technology has been widely used in many applications such as national defense system, scientific instrument, medical diagnostics, gas remote sensing, agriculture, environmental monitoring, and human body surface temperature screening which plays an important role during COVID-19 pandemic, over the past few decades. For example, night vision camera takes real-time NIR images to observe objects in the night without using a visible flashlight; wearable devices such as Apple Watch use red and NIR lights to monitor blood oxygen level by comparing the reflectivity of these two lights in

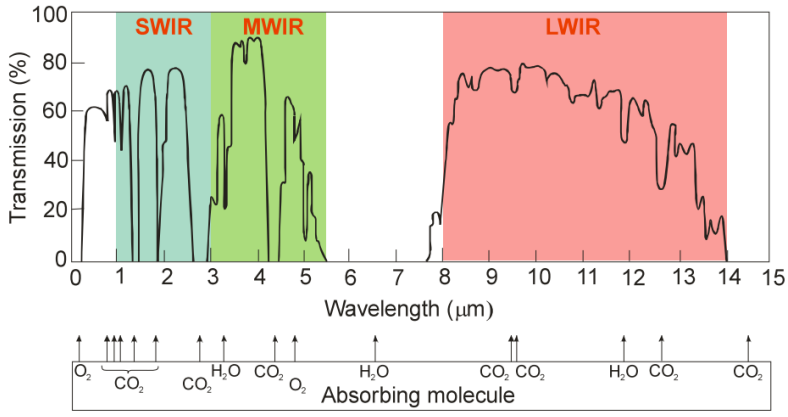

Figure 2. Transmission percentage of IR radiation traveling horizontally at sea level for 6000 ft [6].

the blood through skin, which is a non-invasive method. For applications such as remote sensing and monitoring, the IR radiation must transmit through air for a long distance. Some molecules suspending in the air such as water vapor and carbon dioxide (CO_2) absorb specific IR energy. This causes only a few IR bands can be utilized with lowest impact. Figure 2 illustrates the transmission curve of the IR radiation traveling 6000 ft horizontally in the air at sea level [6]. Obviously, the absorption of H_2O, CO_2, and oxygen molecules separates the IR spectrum into MWIR 3-5 and LWIR 8-14 μm bands, on which most of the research efforts focus.

The significant material development history of IR photodetector is summarized in Figure 3 [7]. In 1959, Lawson *et al.* discovered $Hg_{1-x}Cd_xTe$ alloys with tunable bandgaps by changing Cd composition, which showed superior performance than the extrinsic silicon

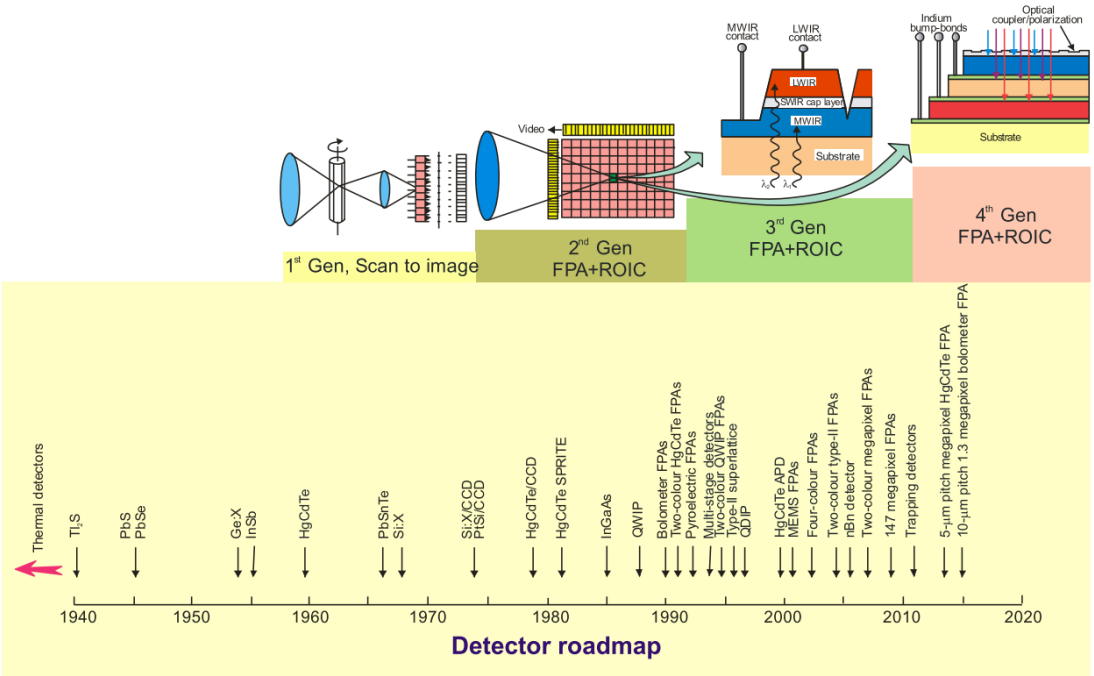

Figure 3. History of infrared photodetector development [7].

and lead-tin telluride ($Pb_{1-x}Sn_xTe$) devices at that time and still are the most prominent materials for IR photodetectors nowadays [8]. The HgCdTe ternary alloy system, whose bandgaps can be tailored from SWIR, MWIR to LWIR and even VLWIR, has many degrees of freedom in detector design since its binary components, HgTe and CdTe, are nearly lattice matched and sharing similar coefficient of thermal expansion [9], enabling them to be grown on $Cd_{1-x}Zn_xTe$ substrate easily with arbitrary Cd composition. The discovery inspired and generated tremendous IR detector research and applications since then. After being studied and developed for over 60 years, the growth and fabrication of HgCdTe ternary alloy system have been well established, understood and improved as the crystalline quality and doping have been substantially advanced and the physics such as the surfaces passivation and band offset are well interpreted [10]. The minority carrier lifetime of HgCdTe detectors is usually limited by intrinsic Auger recombination, and small effective mass results in elevating tunneling current, preventing the device from performing at high operation temperature [11].

1.3 Type-II Superlattices

Since the first paper published by Esaki and Tsu in 1970, the concept of a one-dimensional periodic potential or superlattice in monocrystalline semiconductor has emerged and attracted enormous attentions [2]. From physics point of view, electrons tunneling through the periodic potential barriers and the large period thickness with respect to the lattice constant reduces the size of the Brillouin zone in the growth direction. In other words, with the period of the superlattice being shorter than the electron mean free path,

electrons will be able to tunnel through the periodic potential barriers. This allows the energy states in the individual wells to couple with each other to form subbands. By adjusting either the composition or the layer thickness of the superlattice, one can manipulate the mechanism of the formation of electron and hole subbands which can be indeed considered as the effective bandgap engineering. Type-II superlattices (T2SLs) are firstly reported in 1977 authored by Sai-Halasz *et al.* and realized by Sakaki *et al.* from the IBM T. J. Watson Research Center [12], [13]. In the paper, the author proposed theoretically by Bloch functions, and analyzed a new concept of bilayer semiconductor superlattices in which the band alignment of the two materials is type-II, meaning both the conduction band edge and the valence band edge of one material is lower than the corresponding band edges of the other material and therefore electrons are confined in one material while holes are confined in the other material. Hence, the position of conduction miniband and valence miniband can be tuned independently. It was suggested that the T2SLs can be realized by using closely lattice-matched materials including InAs/GaSb and InGaAs/GaAsSb. Although the band alignment of InAs/GaSb was found to be type-III (broken gap, the conduction band minimum of InAs is 150 meV lower than the valence band maximum of GaSb), the T2SLs still distinguished themselves from type-I superlattices originally proposed by Esaki and Tsu in 1970 [2], in which the bandgap of one material entirely overlaps that of the other. Furthermore, the InAs/GaSb T2SLs have several properties which makes them suitable for infrared detector and an alternative low-cost approach than traditional HgCdTe. For example, the bandgap of the T2SLs can be tailored as small as possible due to their broken gap alignment, and they are also more

immune to band-to-band tunneling compared with bulk materials [14]. However, the drawbacks of InAs/GaSb T2SLs have hindered their progress in recent years due to the facts that the carrier lifetime is not long enough as expected [15], [16]. Also, it is difficult to grow thick T2SL absorber on either InAs or GaSb substrates without the help of metamorphic buffer layers or strain-compensated structure to avoid strain relaxation [17].

Strain-balanced InAs and $InAs_{1-x}Sb_x$ can be grown on a GaSb substrate because the former is tensile while the latter (with $x > 0.09$) is compressive strained. $InAs/InAs_{1-x}Sb_x$ T2SLs consist of alternate fixed thickness of InAs and $InAs_{1-x}Sb_x$ layers for multiple repeats to achieve certain total thickness and effective bandgap. Since the T2SLs are strain-balanced, the absorber can be grown unlimited thick theoretically on GaSb substrate with extremely low defect density, opening up enormous research topics over conventional InAs/GaSb T2SLs in recent years. They have shown superior quality in terms of carrier lifetimes and photoluminescence efficiency, and have been used in many applications such as photodetectors, lasers, and LEDs in the IR wavelength ranges between 4 μm to 12 μm [15], [18]–[20]. T2SLs enable bandgap engineering which leads to larger hole effective masses and greater Auger recombination suppression than those of its II-VI counterpart HgCdTe [21]. These advantages give T2SLs the opportunity to operate at higher temperatures and to have much closer performance compared to the state-of-the-art HgCdTe detectors [22], whose small electron effective mass causes large leakage current due to tunneling. HgCdTe has a high degree of sensitivity of the bandgap energy to the Cd composition, meaning a small change in the Cd composition causes large difference in the bandgap, which adds another uncertainty to growth and device cut-off wavelength. Due to

the type-II band alignment between InAs and $InAs_{1-x}Sb_x$, it is possible to achieve a much narrower bandgap than that of the constituent III-V bulk compound semiconductors by changing the period thickness and Sb composition [23]. The schematic band edge diagram of an InAs/$InAs_{1-x}Sb_x$ T2SLs is shown in Figure 4.

1.4 Unipolar Barrier Photodetectors

Typical structures of semiconductor IR photodetector include pn or pin photodiode, avalanche diode, QWIP, T2SLs, and barrier detectors etc., in which materials can be chosen from HgCdTe, InGaAs, InSb, PbS and PbSe as shown in Figure 1 and 3. Among all structures, pn or pin diode is the most prevalent structure in real-world application. Nonetheless, no matter which structure is used, the key to achieve high performance IR photodetector contains low dark current, high quantum efficiency, low noise, and high dynamic range. With proper designs and improved growth techniques, the optically thick absorber layer with high absorption coefficient and quantum efficient can be achieved by MBE or MOCVD nowadays. Therefore, suppressing the dark current becomes a major

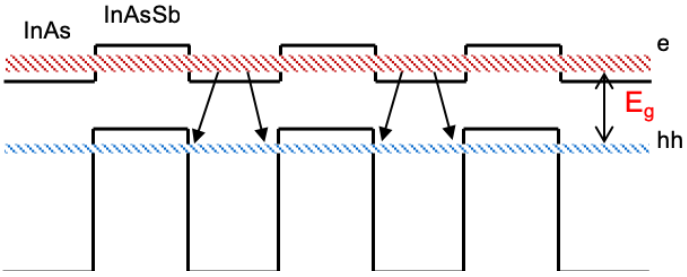

Figure 4. Band edge diagram and mini-bands of InAs/$InAs_{1-x}Sb_x$ type-II superlattices (T2SLs). The transition energy is tunable by changing period thickness and Sb composition. Due to the type-II band alignment, it is possible for InAs/$InAs_{1-x}Sb_x$ T2SLs to achieve narrower bandgap than that of constituent III-V compound semiconductors.

challenge for MWIR and LWIR photodetectors due to their narrow bandgaps. The dark current mechanisms include Shockley-Read-Hall (SRH) process, causing the generation-recombination (G-R) dark current in the depletion region, diffusion dark current in the quasi-neutral region, surface leakage, Auger recombination process, and band-to-band tunneling under high voltage bias.

As discussed in the previous section, the T2SLs have successfully reduced the Auger recombination and tunneling dark currents due to their heavy electron effective mass and the substantial splitting of the light- and heavy-hole bands [24]. The Barrier IR Detector, sometimes called BIRD or unipolar barrier photodetector, has received a lot of attentions since the concept was reported by Maimon and Wicks in 2006 [25] and Klipstein and Yaacov in 2003 [26]. The term “unipolar barrier” describes a barrier layer with larger bandgap is used to block one carrier type (electron or hole) while allowing the other one to flow through freely. The unipolar barrier was made possible by hetero-structure epitaxy [27], which has been widely used in lasers, LEDs, and solar cells. The unipolar barrier device is also usually called XBn for short where the first X represents either n- or p-type contact (window) layer, B represents barrier layer, and the last n stands for n-type absorber. The schematic band diagram of a typical nBn device, is shown in Figure 5. The hetero-structure barrier layer has a conduction band barrier to block electron while the valence band is aligned to the absorber.

The unipolar barrier device further reduces the SRH process since when applied voltage bias, the depletion region and voltage drop are confined in the wide-bandgap barrier layer, leading to suppressed G-R dark current, which is proportional to

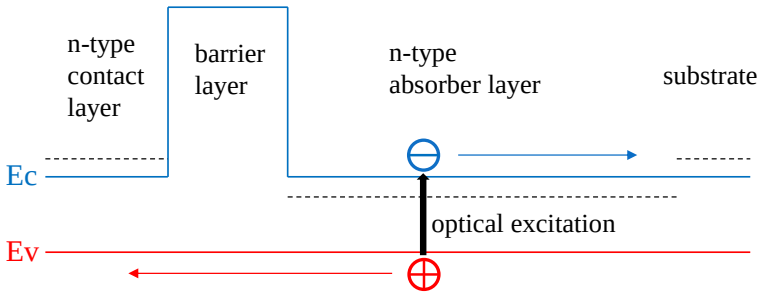

Figure 5. Schematic band edge diagram of nBn structure. The horizontal dash line represents the Fermi-level.

exp $(-E_g/2kT)$ (assuming mid-gap defect level) [28]. In addition, it is known that the surface states or the surface Fermi-level pinning result in surface leakage especially for InAs which surface state is higher than its conduction band edge. Inserting the electron barrier as shown in Figure 5 essentially cuts off the electron conduction channel to the surface, further reducing the dark current by eliminating the surface leakage [25].

Combining all the aforementioned benefits of InAs/InAsSb T2SLs and XBn structure, it is promising to fabricate an InAs/InAsSb T2SL nBn IR photodetector, which is highly desired because of reduced G-R, tunneling, Auger, and surface dark current. The diffusion dark current is similar to another IR photodetectors of different types or materials with the same bandgap energy since it major contribution is from the quasi-neutral region and is proportional to exp $(-E_g/kT)$ [25].

1.5 Water-soluble Epitaxial Lift-off Technology and Its Application to Solar Cells

Apart from the photodetectors, solar cells are the most critical optoelectronic devices due to the needs for renewable energy recently. The optimum bandgap for a single-junction solar cell as determined by the detailed-balance model is around 1.4 eV [29], which can

result in a power conversion efficiency of 33 % under the AM 1.5G spectrum. Recently, the demonstration of a monocrystalline CdTe solar cell with an open-circuit voltage of over 1.12 V and an active-area efficiency of 20% has been reported by using MBE [30], [31]. Further improvement in short-circuit current generation can be achieved by bandgap reduction, from 1.5 eV, the bandgap of CdTe, to 1.4 eV, through using CdSeTe alloys with lower bandgaps. However, due to a very large lattice mismatch of 5.86% between CdSe and CdTe and lack of commercially available substrate for lattice constant between 6.1 and 6.5 Å as shown in Figure 1, it is very challenging to grow thick, high quality monocrystalline CdSeTe random ternary alloys with bandgap of 1.4 eV on InSb substrates. Further challenges to the formation of a digital CdSeTe alloys are the high vapor pressure of group-VI elements and the low sticking coefficient of Se in CdTe, and large miscibility gap [32], making it difficult to grow high quality CdSe in a CdSe/CdTe digital alloy [33], [34]. Due to these difficulties, the removal of light-absorbing InSb substrate and the addition of metal back reflector would be the feasible way for the further improvement of monocrystalline CdTe solar cell. Therefore, a promising solution to the CdTe solar cell lift-off challenge has been demonstrated by using water-soluble, single-crystal MgTe as the sacrificial layer to enable epitaxial lift-off (ELO). The highly-selective etching rate of MgTe to CdTe in water means this material is primed to be the II-VI contemporary to AlAs, a material which has been used for decades as a sacrificial layer to enable free-standing GaAs/AlGaAs thin-film solar cells [35]. Developing free-standing CdTe and MgCdTe solar cells enables a whole world of possibilities not limited to back mirrors, light scattering features, and tandem-cell integration on even flexible panels. This dissertation also reports

a detailed study of the ELO process using MgTe layers, the demonstration of metal back reflector to enhance light extraction and photon recycling, and its feasibility for future high-efficiency thin-film solar cells or tandem-cell integration.

The ELO technology also opens up a lot of opportunities for other optoelectronic devices including multi-color photodetector by combining state-of-the-art CdTe nBn and InSb photodetectors to achieve visible and mid- to long-wave IR detection [36], and resonant-cavity IR LED and photodetector applications by adding a lifted III-V/II-VI distributed Bragg reflector (DBR), with over 90 % reflectivity and much thinner thickness than that of conventional GaSb/AlGaSb DBR [37], on top of InAs/$InAs_{1-x}Sb_x$ T2SLs active layer. Furthermore, it is known that the high-cost of a HgCdTe IR photodetector is due to the availability of large-area CdTe and ZnCdTe substrate, whose prices are still much higher than the other commercially available III-V substrates. The ELO method creates an area in which the low-cost HgCdTe IR photodetector is widely available by growing HgCdTe on nearly lattice-matched large-area InSb substrate with MgTe sacrificial layer in the middle.

Since the newly invented water-soluble lift-off process only uses water as the etchant to dissolve MgTe sacrificial layer, the InSb substrate is intact and can be reused numerous times before it degrades and needs additional polishing. The large area up to 6 inch in diameter InSb substrate and the reuse of it can reduce the overall cost significantly.

1.6 Organization of the Dissertation

In this dissertation, the detailed MBE growth procedure and material characterization of InAs/$InAs_{1-x}Sb_x$ T2SLs are discussed in chapter 2, including photoluminescence (PL) and X-ray diffraction (XRD). The study of vertical carrier transport dynamics in the InAs/$InAs_{1-x}Sb_x$ T2SLs by using steady-state and time-resolved photoluminescence is discussed in chapter 3. Based on chapter 2 and 3, the InAs/InAsSb T2SL nBn, pBn, and pBp barrier photodetector application is discussed in chapter 4. A lift-off technology using water-soluble MgTe sacrificial layer is discussed in chapter 5. Finally, the conclusion and outlook of the present work are included in chapter 6.

2. GROWTH AND CHARACTERIZATION OF InAs/InAs$_{1-x}$Sb$_x$ TYPE-II SUPERLATTICES

2.1 Basics of Molecular Beam Epitaxy

Molecular beam epitaxy enables the deposition of high crystalline quality thin film due to its ultra-high vacuum (UHV) chamber, which is characterized by pressures lower than 10^{-9} torr. UHV is achieved by pumping the gas and particles out of a chamber. At these low pressures, the mean free path of a molecule is extremely long, indicating the molecule can travel such a long distance in one direction linearly without collision and interaction with the other particles. The mean free path is defined as following:

$$\lambda = \frac{RT}{\sqrt{2}\pi d^2 N_A P}, \tag{5}$$

where R is the gas constant, T is the temperature, d is the diameter of the particle, N_A is Avogadro's number, and P is the pressure. A schematic MBE chamber is illustrated in

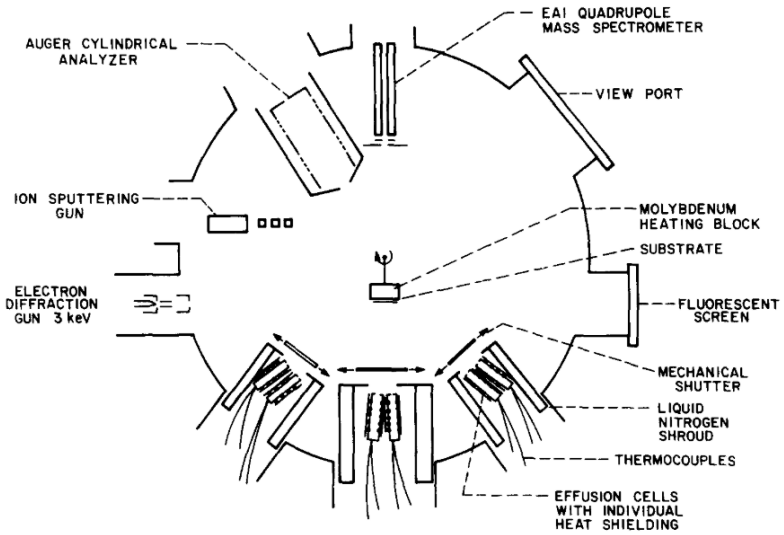

Figure 6. Schematic cross-section view of molecular beam epitaxy chamber [4].

Figure 6. Different source materials are loaded in individual pyrolytic boron nitride (PBN) or Graphite crucible inside separated effusion cells. According to the equation (5), for a typical MBE chamber with pressures at 10^{-10} torr, the mean free path for a molecule in the chamber is 1 km to 10^5 km, depending on the diameter of molecule. This indicates that the molecule beam of source material, which is vaporized due to heating, in the effusion cell can travel directly from crucible to the substrate and 'grow' on the substrate surface. In addition, to minimize the impurities and unwanted particles in the source material and chamber, the use of 5N (99.999%) or higher purity source material is highly desired.

Figure 7 shows the schematic drawing of the dual-chamber MBE system in ASU MBE Optoelectronics Group. The III-V chamber consists of Al, Ga, and In effusion cells, and P, As, Sb, Bi valved cells. In particular, the P, As, and Sb cells have cracking zones to produce group-V monomers and dimers. A tri-dopant cell is used, consisting of Si, Te, and Be dopants. The II-VI chamber consists of Be, Mg, Cd, and Zn effusion cells, and Se and Te valved cells. The two separate chambers are connected by a preparation chamber, allowing

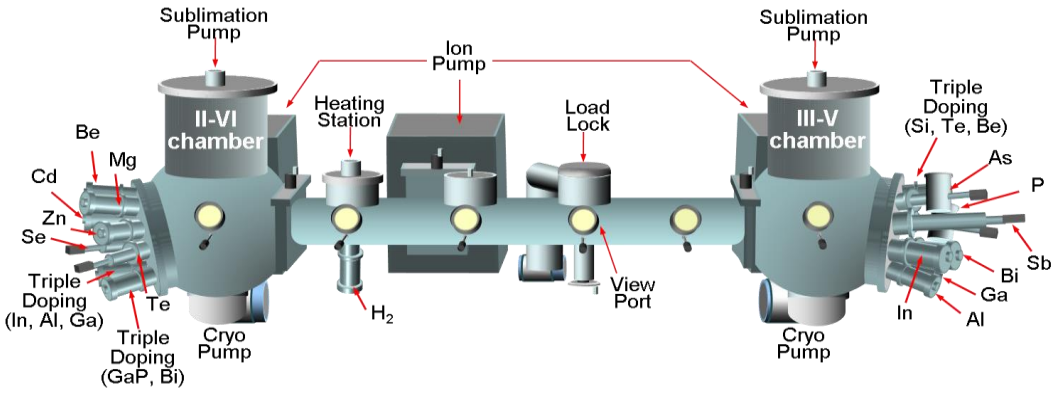

Figure 7. Schematic drawing of dual-chamber MBE system. The III-V and II-VI chambers are connected by a preparation chamber, allowing samples to be transferred under ultra-high vacuum.

samples to be transferred from each other under UHV. The substrate heater temperature is measured and controlled by the thermocouple, located on the back side of the substrate holder, and a close-loop Eurotherm controller, while the temperature of sample surface is monitored by a pyrometer. The temperature of each cell is also measured and controlled by thermocouple and Eurotherm. Shutters, in front of all cells, are used to control the beam flux, which is measured by a beam flux monitoring (BFM) ion gauge. The substrate holder keeps rotating during the growth to smooth out any nonuniformity. Reflective high energy electron diffraction (RHEED) is used to monitor the sample surface by confirming surface reconstruction during the growth.

All samples presented in this dissertation were grown by the dual-chamber MBE system at ASU. For the II-VI samples discussed in chapter 5, oxide removal of InSb substrate and the growth InSb buffer were performed in III-V chamber. Samples were then transferred into II-VI chamber to complete the II-VI material growth.

2.2 Molecular-beam-epitaxy Growth of InAs/$InAs_{1-x}Sb_x$ Type-II Superlattices

InAs has slightly smaller lattice compared to that of GaSb, while $InAs_{1-x}Sb_x$ with $x > 0.09$ has larger lattice constant than that of GaSb, making InAs is tensile strained but $InAs_{1-x}Sb_x$ is compressively strained when these two materials are grown on GaSb substrate. Since either InAs or $InAs_{1-x}Sb_x$ is strained when growing on GaSb substrate, if the layer thickness is too large, the layer becomes relaxed and a substantial amount of misfit dislocations would destroy the crystalline quality of the epitaxial thin film. Matthews and Blakeslee calculated the critical thickness of the interface structure in multilayers, within

which the layer can be grown fully-strained, based on two forces: the force exerted by the misfit strain, and the tension in the dislocation line [38]. The expression for a zincblende (001) structure is the following:

$$h_c = \frac{a_S\left(1-\frac{\nu}{4}\right)\left[\ln\left(\frac{\sqrt{2}h_c}{a_S}\right)+1\right]}{\sqrt{2}\pi|\varepsilon|(1+\nu)} \tag{6}$$

$$\nu = \frac{C_{12}}{C_{11}+C_{12}} \tag{7}$$

$$\varepsilon = \frac{a_S - a_L}{a_L}, \tag{8}$$

where h_c is the critical thickness, a_S is the substrate lattice constant, a_L is the layer thickness, ν is the Poisson's ratio, C_{11} and C_{12} are the elastic constants of the layer, and ε is the strain of the layer. The critical thickness for different multi-layer structure is summarized in Table 1.

The critical thickness calculated by equation (6) limits the maximum thickness which can be grown on a substrate without generating misfit dislocations. If two or more layers with different types of strain, compressive or tensile, grow alternatively on a substrate, it is possible to balance out the strains. There is no in-plane shear force to generate misfit dislocations and therefore the in-plane stress is zero, suggesting that the alternative multi-

Table 1. Critical thickness of various multi-layer structures calculated by equation (6).

Multi-layer structure	Critical thickness
Superlattices	h_c
Quantum well	$h_c/2$
Single layer	$h_c/4$

layers can be grown infinite thick on the substrate [39]. The aim of the strain-balance is to achieve zero average in-plane stress in the alternative tensile and compressively strained layer combination. As described by Ekins-Daukes *et al.* [39], there are three methods for attaining strain-balance condition, including average lattice method, thickness weighted method, and zero-stress method. The thickness and freestanding lattice constant of the compressive and tensile strain layers can be defined as t_1, a_1, and t_2, a_2 and the substrate lattice constant is defined as a_S. For average lattice method, it basically just calculates the average lattice constant of the two layers to be the same as that of substrate, and assumes the identical elastic properties for both layers, resulting in the expression as shown below:

$$a_S = \frac{t_1 a_1 + t_2 a_2}{t_1 + t_2}. \tag{9}$$

The thickness weighted method suggests the strain-balance condition is achieved by having equal strain-thickness product for the two layers. The expression is shown in equation (10), which is not taking elastic constant into account.

$$t_1 \varepsilon_1 + t_2 \varepsilon_2 = 0\,, \tag{10}$$

where ε_1 and ε_2 are the compressive and tensile strain in the two layers, respectively. As the strain is defined as in equation (8), equation (10) can be rearranged as:

$$a_S = \frac{(t_1 + t_2) a_1 a_2}{t_1 a_2 + t_2 a_1}. \tag{11}$$

when considering the difference of the elastic constant in the two layers, equations (10) and (11) can be written as followings by including elastic parameter A,

$$A_1 t_1 \varepsilon_1 + A_2 t_2 \varepsilon_2 = 0 \tag{12}$$

$$a_S = \frac{(A_1 t_1 + A_2 t_2) a_1 a_2}{A_1 t_1 a_2 + A_2 t_2 a_1}, \tag{13}$$

where $A = C_{11} + C_{12} - 2C_{12}^2/C_{11}$.

The zero-stress method considers the lowest energy state of the tensile/compressively strained layers, at which no average stress present. The key idea is that when the corresponding lattice constant is equal to that of the substrate, no further in-plane stress or strain is introduced [39]. This approach calculates the strain-balance condition from classical elasticity theory and the results are shown as following:

$$A_1 t_1 \varepsilon_1 a_2 + A_2 t_2 \varepsilon_2 a_1 = 0 \tag{14}$$

$$a_S = \frac{A_1 t_1 a_1 a_2^2 + A_2 t_2 a_2 a_1^2}{A_1 t_1 a_2^2 + A_2 t_2 a_1^2}. \tag{15}$$

The thickness-weighted and zero-stress methods differ by a factor or a_1/a_2, which arises from the different definition of the strain, either using substrate lattice constant or average lattice constant in the denominator in equation (8) [39]. If the strict definition of strain and the in-plane force due to bi-axial strain are allowed, the results from these two methods should be the same. The zero-stress method is based on the strain-balanced double layers. It is suitable for the structures grown on virtual substrates, given the films themselves are still pseudomorphic. Therefore, for the T2SLs presented in the dissertation, thickness-weighted method is adopted to calculate the strain-balance condition.

InAs/$InAs_{1-x}Sb_x$ superlattice samples with or without strain-balanced design were grown by MBE on (001) GaSb substrates at temperature of 410 to 450 ℃. The layer structure of the samples consisted of a superlattice of alternating InAs and $InAs_{1-x}Sb_x$ layers totaling a thickness between 0.5 to 2 μm which was sandwiched between two 10-nm-thick

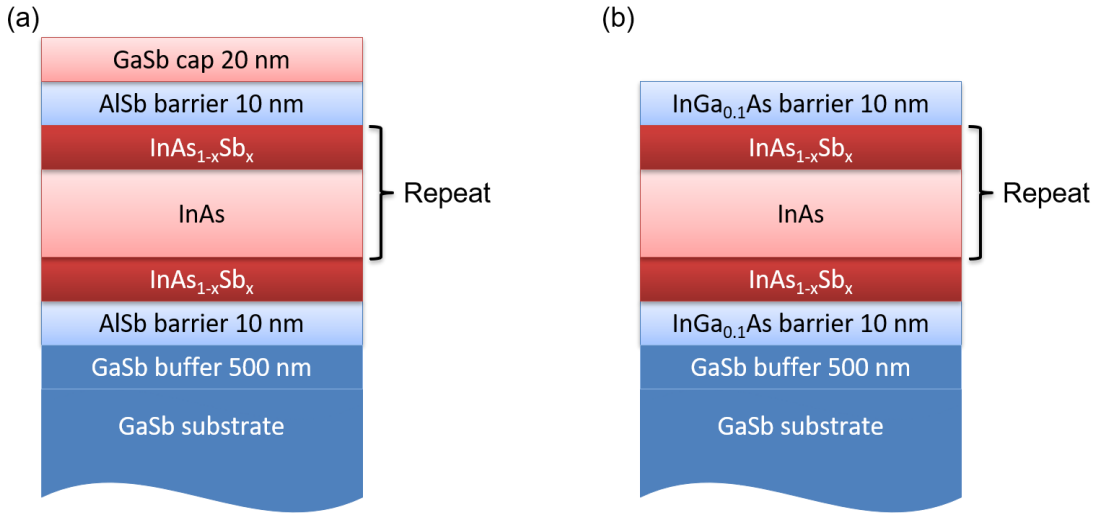

Figure 8. The cross-section of InAs/$InAs_{1-x}Sb_x$ T2SL samples with (a) AlSb or (b) $In_{0.9}Ga_{0.1}As$ barriers. A 20-nm-thick GaSb cap layer was grown on top for the samples with AlSb barrier layers.

AlSb or $In_{0.9}Ga_{0.1}As$ barrier layers which provided better carrier confinement and reduced surface recombination. A 20-nm-thick GaSb cap layer was grown for samples with an AlSb barrier in order to prevent the rapid oxidation of Al in atmosphere. The schematic cross-section of the superlattice sample is shown in Figure 8. One of the advantages of growing InAs/$InAs_{1-x}Sb_x$ T2SLs is the easy-to-achieve alternating of layers by maintaining fixed As flux and modulating one Sb shutter which occur without any intermixing at the interfaces. The growth rate of InAs was kept at 15 nm/min with an As/In flux ratio of 1.2 while the Sb/In flux ratio ranged from 0.251 to 1 for Sb compositions in $InAs_{1-x}Sb_x$ alloy, *x* ranging from 0.206 to 0.426 for various samples. The layer thickness of InAs and $InAs_{1-x}Sb_x$ is calculated based on of thickness-weighted method of strain-balance condition as described in equations (12) and (13). Table 2 lists five T2SL samples with different layer thickness and Sb compositions, resulting in tunable photoluminescence wavelength from MWIR to

Table 2. InAs/$InAs_{1-x}Sb_x$ T2SLs sample list. The T2SLs shows the ability of tunable wavelength by changing period thickness and Sb composition.

Sample #	InAs thickness (nm)	$InAs_{1-x}Sb_x$ thickness (nm)	*x*	Peak λ (μm)
B2525	2.08	1.46	0.206	3.9
B2571	1.63	1.13	0.370	4.4
B2606	9.92	3.97	0.275	6.3
B2657	13.78	4.22	0.383	8.3
B2660	14.15	4.58	0.426	11.0

LWIR. The detailed MBE growth procedure and the comparison study of different growth temperature have been described elsewhere [40], [41].

2.3 X-ray Diffraction of InAs/$InAs_{1-x}Sb_x$ Type-II Superlattices

The structural properties of these T2SL samples were characterized by using PANalytical X'Pert Pro MRD High Resolution X-ray Diffraction (HR XRD). $\omega - 2\theta$ scan along the (004) plane was measured. The HRXRD is a powerful technique to evaluate a crystalline sample which has periodic structure with the atomic spacing close to the X-ray wavelength. This allows the X-ray to diffract into many directions. Several structure information and defects can be determined by XRD, including composition, thickness, superlattice period, mismatch, relaxation, misorientation, dislocation density, curvature, and inhomogeneity. The diffraction occurs when the Bragg's law is satisfied, i.e. the Ewald construction is fulfilled. As described in the following equations, a cubic lattice structure is assumed.

$$2d \sin\theta = n\lambda \tag{16}$$

$$d = \frac{a}{\sqrt{h^2 + k^2 + l^2}}, \tag{17}$$

where d is the spacing between adjacent parallel plane, θ is the diffraction angle, λ is the X-ray wavelength (i.e. 1.5406 Å for Cu K_α), n is the order of diffraction (positive integer), a is the lattice constant, and h, k, l are the miller indices of the plane at which the diffraction occurs. In particular, for a superlattice sample, since the additional periodic structure is made by artificially grown a multi-layer stack with a period Λ, the Fourier transform of the structure creates extra frequencies in the reciprocal space, called satellite peaks. Therefore, the superlattice period Λ can be determined from the separation of the satellite peaks on the symmetric plane $\omega - 2\theta$ scan, and so the Bragg's law becomes:

$$2\Lambda \sin\theta_m = m\lambda\,, \tag{18}$$

where θ_m is the diffraction angle of the satellite peak and m is the order of diffraction. For symmetric reflections,

$$\Lambda = \frac{(m_i - m_j)\lambda}{2(\sin\theta_{m_i} - \sin\theta_{m_j})}. \tag{19}$$

By measuring the diffraction angles θ_m for multiple diffraction order m, an accurate estimate of the average period thickness can be obtained by determining Λ for combinations of Δm.

The average superlattice composition, $\bar{x}$, is determined by the 0^{th} order satellite peak, at which occurs the average Bragg's angle of superlattice not of the alloy layers alone. To determine the alloy composition, x, it is necessary to know the thickness of the alloy, d, and the period, Λ. The alloy composition is given by

$$x = \frac{\Lambda \bar{x}}{d}. \tag{20}$$

Take an InAs/$InAs_{1-x}Sb_x$ T2SL sample for example, Figure 9 shows an $\omega - 2\theta$ XRD of (004)-plane of sample B2606. The results are analyzed with X'Pert Epitaxy software. This sample shows intense satellite peaks with narrow linewidth, indicating high degree of crystalline quality, abrupt interface, and uniform superlattice period. The peak at 30.36° is from the GaSb substrate and all the satellite peaks are labeled with 0^{th}, $\pm1^{st}$, and $\pm2^{nd}$ etc. The average superlattice period thickness is calculated by selecting multiple adjacent satellite peaks and using equation (19). Often time the period thickness, and InAs and $InAs_{1-x}Sb_x$ thickness are not unknown parameters since they are roughly estimated by the InAs and $InAs_{1-x}Sb_x$ growth rates and shutter time during the MBE growth. Therefore, the accurate InAs and $InAs_{1-x}Sb_x$ are obtained after the average period thickness Λ is confirmed with XRD and taking the growth rate and Sb shutter time into account. Therefore, the Sb composition is the only parameter to fit in the XRD scan with the simulation software. The extracted parameters, taken from the best fit of the curve, are that of 9.92-nm-thick InAs and 3.97-nm-thick $InAs_{1-x}Sb_x$ where x=0.275. Here, an abrupt interface and zero unintentional Sb incorporation into the InAs layers are assumed. The simulation curve plotted in Figure 9 matches the measurement curve, even the $In_{0.9}Ga_{0.1}As$ barrier peak is shown and matched, suggesting high degree of accuracy of the fitted thickness and composition.

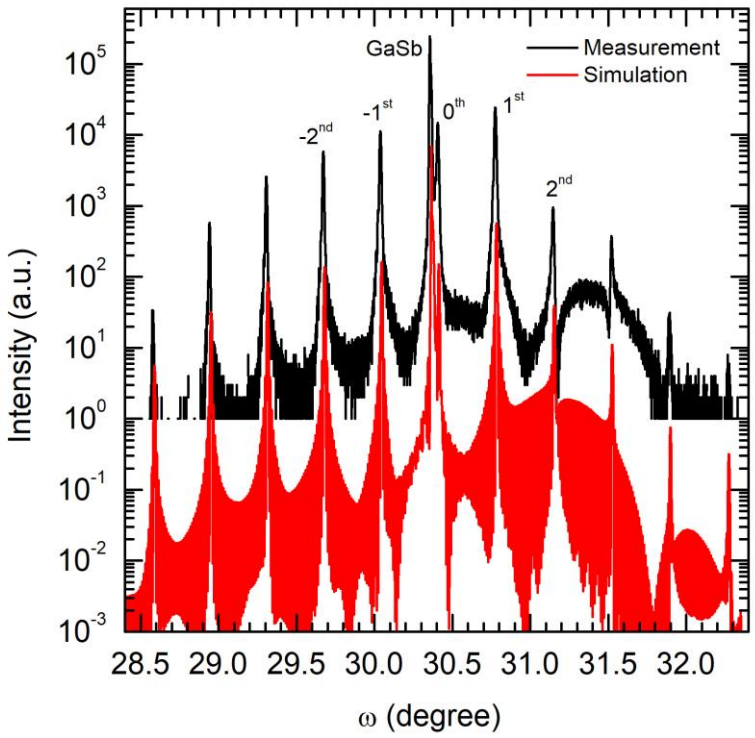

Figure 9. $\omega - 2\theta$ X-ray diffraction (XRD) of (004)-plane of sample B2606. The extracted parameters of the best fit are 9.92-nm-thick InAs and 3.97-nm-thick $InAs_{1-x}Sb_x$ with $x = 0.275$.

2.4 Photoluminescence of InAs/InAs$_{1-x}$Sb$_x$ Type-II Superlattices

Optical properties of these T2SLs were measured by steady-state photoluminescence (SSPL) at 12 K using a pump power of 6 W/cm^2 from a 785 nm laser diode. A double-modulation Nicolet 760 Fourier transform infrared (FTIR), equipped with liquid-nitrogen-cooled InSb and HgCdTe detectors, were used to perform the measurement. The laser was modulated at 50 kHz. The samples were placed in a closed cycle cryogenic system to achieve a temperature of 12 K. Figure 10 illustrates the schematic FTIR system. The effective transition energy at low temperatures can be determined by the PL peak position in unit of meV or micrometers. The normalized PL spectra of the samples listed in Table 2 are shown in Figure 11 as a function of photon energy. Since this measurement was done in atmosphere, the discontinuity in the PL spectra around 290 meV was the result of CO_2 absorption, which can be removed by normalization with the calibration curve of the

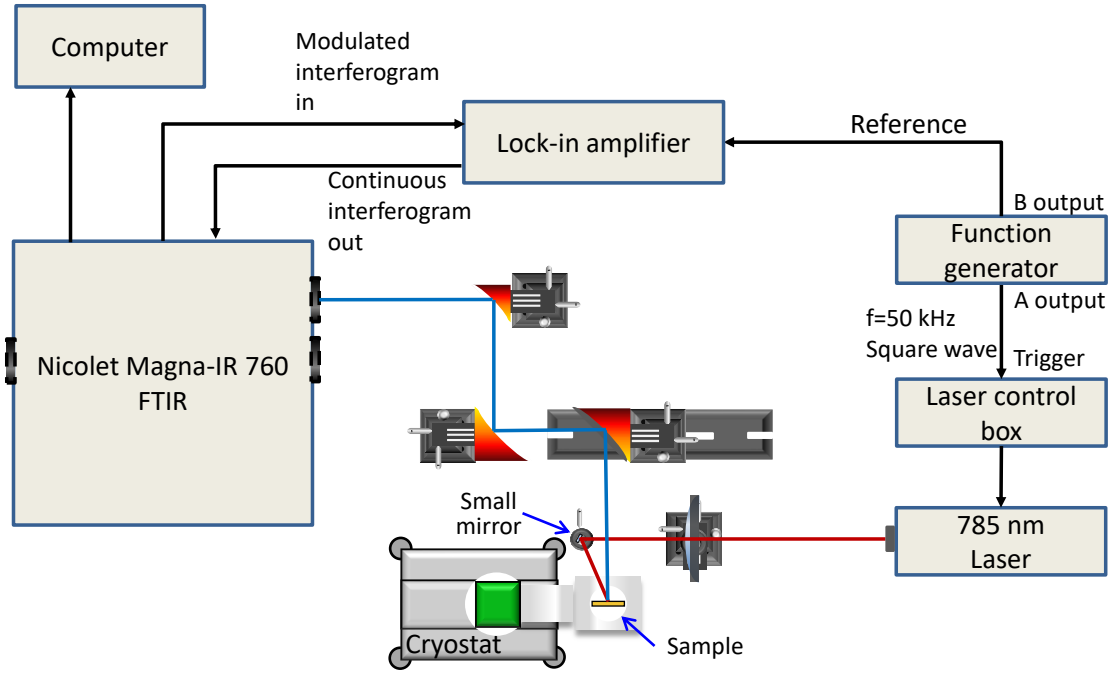

Figure 10. Schematic of double-modulation FTIR system.

detector. These T2SL samples show strong PL intensity and high signal-to-noise ratio, except for sample B2606, whose PL peak is at 6.3 μm. The low PL intensity could result from the strong H_2O absorption in the air as depicted in Figure 2. Figure 11 also showcases that the T2SLs have the flexibility of the bandgap (PL peak energy $-\frac{1}{2}kT$) engineering by manipulating the layer thickness and Sb composition.

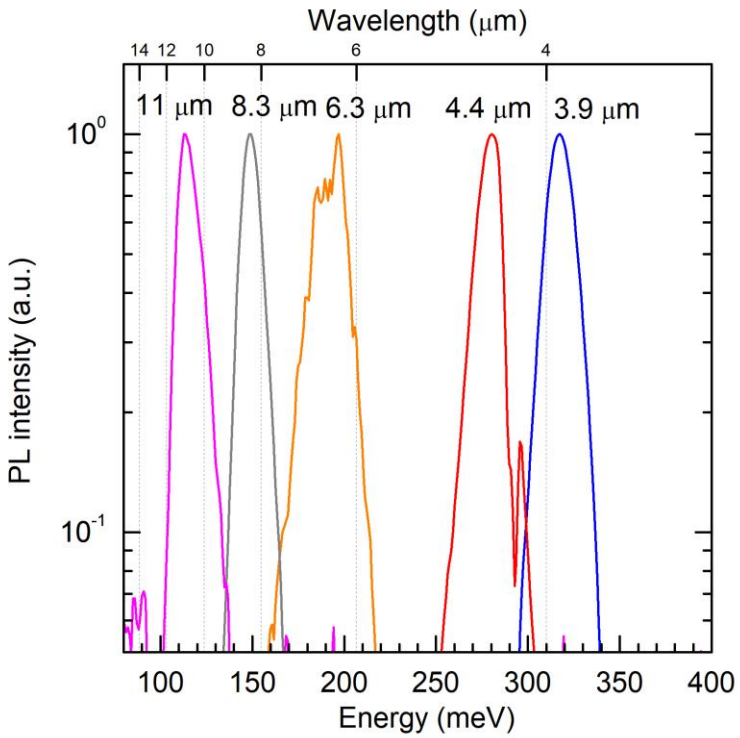

Figure 11. Normalized 12 K photoluminescence spectra from InAs/$InAs_{1-x}Sb_x$ T2SLs samples listed in Table 2. The discontinuity at 290 meV is the result of CO_2 absorption.

3. STUDY OF VERTICAL CARRIER TRANSPORT DYNAMICS IN InAs/$InAs_{1-x}Sb_x$ TYPE-II SUPERLATTICES

Recently, the demonstration of carrier lifetimes in mid-wave IR (MWIR) and long-wave IR (LWIR) InAs/$InAs_{1-x}Sb_x$ T2SLs exceeding 400 ns has inspired tremendous scientific research and technology development in this field [15], [42]–[47]. The long carrier lifetime was principally attributed to the suppression of the Shockley-Read-Hall (SRH) recombination process due to the fact that many defect energy levels in the InAs/$InAs_{1-x}Sb_x$ T2SLs are in the conduction band, and thus have limited adverse impact on the carrier lifetime because they do not act as nonradiative recombination traps [48]. InAs/$InAs_{1-x}Sb_x$ T2SLs devices such as conventional pin and barrier XBn photodetectors both in MWIR and LWIR wavelength ranges have demonstrated remarkable performance, getting much closer to that of the state-of-the-art HgCdTe counterparts devices [22], [49]–[56]. However, further improvement in the detector performance has been hindered by the poor hole transport properties of InAs/$InAs_{1-x}Sb_x$ T2SLs, which results in low quantum efficiency. It is, therefore, important to understand the fundamental physics of vertical hole transport throughout T2SLs and eventually to come up with innovative means to circumvent this challenge. The quantitative study of vertical carrier transport, especially hole transport, by measuring mobility is, however, not a trivial task, due to the relatively small hole mobility caused by the presence of multiple interfaces with large valance band offset, thin layer thickness of T2SLs, and the need for a sophisticated method of measurement. A hole mobility of 60 cm^2/Vs at 6 K has been estimated by using electron beam induced current (EBIC), as seen in a paper published recently [57].

3.1 Previous Works on Vertical Carrier Transport

Vertical carrier transport of periodic structure such as GaAs/AlGaAs multiple-quantum wells (MQWs) and SL has been studied intensively back in 1980s [58]–[65]. The concept of using an enlarged well (EW) served as the indicator of vertical carrier transport throughout the film was introduced. The EW can be placed in the front or back surface or any positions within the studied structure. When carriers move vertically, either by diffusion or drift, they will be captured by the EW and recombine in the well, resulting in PL with relatively longer wavelength than that of studied structure. However, some assumptions in the early works may not be valid in the case of InAs/$InAs_{1-x}Sb_x$ T2SLs. For instance, due to small bandgap of the T2SLs, no discrete excitonic peak is observed even at 10 K. Also, there is possible co-excitation of carriers both in SL and EW due to the fact that the thickness of SL is often thinner or compared to the laser penetration depth, potentially resulting in inaccurate modeling and extracted mobility which assume the excited electron-hole pair density in the EW equals to zero at the beginning of the laser pulse. Therefore, the easiest way to circumvent this concern is to have a thick SL transport region, as described in the following section. Studies of vertical carrier transport in other material systems such as InAs/GaSb T2SLs [66], InGaAs/GaAsP MQW [67], and InAs/InAsSb T2SLs [57] by using pump-probe method, time-of-flight technique, and electron-beam induced current (EBIC) method, respectively, have been carried out recently and summarized in Table 3. The disadvantages of those aforementioned methods in the Table 3 are either sophisticated equipment needed, such as MWIR and LWIR pump-probe systems or scanning electron microscopy (SEM), or potentially large error due to co-

excitation of carriers in SL and EW. Recent further studies regarding InAs/InAsSb T2SLs using better methods and thorough experiment design have deepened the understanding of carrier transport [68]–[73].

In this work, two straightforward methods, i.e. steady-state photoluminescence (SSPL) spectroscopy and time-resolve photoluminescence (TRPL) spectroscopy, are used with an ambipolar diffusion model to extract the temperature-dependent vertical hole mobility in InAs/$InAs_{1-x}Sb_x$ T2SLs. The hole mobility extracted from the SSPL spectroscopy agrees very well with the mobility obtained from the TRPL spectroscopy.

Table 3. Previous works on vertical carrier transport of MQW and SL.

Method	Material system	Model	Limitation	Findings	Ref.
Pump-probe	InAs/GaSb T2SLs	Ambipolar diffusion	1. Femto-second MWIR and LWIR pulse Laser required 2. Co-excitation of carriers in both MWIR and LWIR T2SLs	D_{amb} = 0.25 cm^2/s (excitation density = $5.6 \times 10^{17}\ cm^{-3}$ at 77 K)	[66]
EBIC	InAs/InAsSb T2SLs	Monte Carlo simulation & drift/diffusion	1. Complicated modeling 2. Potentially large error due to a finite electron-T2SL interaction volume 3. SEM required	D_h = 0.03 cm^2/s (at 6 K)	[57]
Carrier TOF	InGaAs/GaAsP MQW	Drift	1. Complicated device fabrication 2. Electric field required, may not work for narrow bandgap material	Drift mobility = 0.28 cm^2/Vs	[67]
Steady-state photoluminescence	GaAs/AlGaAs SL	Rate equation & diffusion	1. Complicated modeling 2. Co-excitation of carriers in both SL and EW	Diffusion length = 0.1 – 0.5 µm	[65]

3.2 Carrier Generation and Recombination

The electrons and holes are created in pairs. Therefore, when the semiconductor is in equilibrium, the thermal-generation rates of electrons (G_{n0}) and holes are equal (G_{p0}), so as the recombination rates of electrons (R_{n0}) and holes (R_{p0}).

$$G_{n0} = G_{p0}\,, R_{n0} = R_{p0}\,. \tag{21}$$

The carrier concentration in equilibrium is independent of time, suggesting the generation and recombination rates are equal as well,

$$G_{n0} = G_{p0} = R_{n0} = R_{p0}\,. \tag{22}$$

When photons with energy higher than the semiconductor bandgap are incident on the material, electrons in the valence band will be excited into the conduction band, leaving additional holes in the valence band, indicating electron-hole pairs are generated by incident photons, and the semiconductor is in non-equilibrium. The additional electrons and holes are called excess electrons (δn) and holes (δp) and their generation rates are also equal. Figure 12 illustrates the process.

$$G_n' = G_p' \tag{23}$$

$$n = n_0 + \delta n \tag{24}$$

$$p = p_0 + \delta p \tag{25}$$

$$np \neq n_0 p_0 = n_i^2\,, \tag{26}$$

where n, p, n_0, p_0 are total electron and hole, and equilibrium electron and hole concentrations, respectively, and n_i is the intrinsic carrier concentration. The recombination rate of excess electrons and holes are equal as both carriers are annihilated at the same time when recombination,

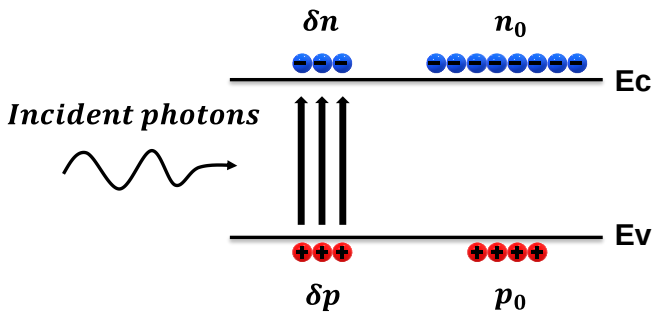

Figure 12. Creation of excess electrons and holes by photons.

$$R_n' = R_p' \,. \tag{27}$$

As a result, under non-equilibrium condition, the carrier concentration is a function of time, given the net rate of change in the electron concentration,

$$\frac{dn(t)}{dt} = \alpha_r[n_i^2 - n(t)p(t)] \,, \tag{28}$$

where α_r is the constant of proportionality for recombination. Since n_0 and p_0 are independent of time, and $\delta n(t) = \delta p(t)$,

$$\begin{aligned} \frac{d\big(\delta n(t)\big)}{dt} &= \alpha_r[n_i^2 - (n_0 + \delta n(t))(p_0 + \delta p(t))] \\ &= -\alpha_r \delta n(t)[(n_0 + p_0) + \delta n(t)] \,. \end{aligned} \tag{29}$$

For a p-type material, $p_0 \gg n_0$, and low-level injection, $\delta n(t) = \delta p(t) \ll p_0$,

$$\frac{d(\delta n(t))}{dt} = -\alpha_r p_0 \delta n(t) \,, \tag{30}$$

given the solution of the equation as

$$\delta n(t) = \delta n(0) e^{-\alpha_r p_0 t} = \delta n(0) e^{-t/\tau_{n0}} \,, \tag{31}$$

where τ_{n0} is the excess minority carrier lifetime for electron and $\tau_{n0} = (\alpha_r p_0)^{-1}$.

With that, the recombination rate

$$R_n' = \frac{-d(\delta n(t))}{dt} = +\alpha_r p_0 \delta n(t) = \frac{\delta n(t)}{\tau_{n0}} = R_p' \,. \tag{32}$$

In the case of an n-type material ($n_0 \gg p_0$) under low-level injection, $\delta n(t) = \delta p(t) \ll n_0$,

$$R_n' = R_p' = \frac{\delta p(t)}{\tau_{p0}}, \tag{33}$$

where τ_{p0} is the excess minority carrier lifetime of holes $\tau_{n0} = (\alpha_r n_0)^{-1}$. According to equations (32) and (33), the excess recombination rate is determined by the excess minority carrier lifetime.

3.3 Continuity Equations and Diffusion Equations

The continuity equation describes the behavior of excess carriers with time and in space in the presence of electric fields and density gradients. Considering a one-dimensional hole flux (F_p^+) is entering the differential element at x and is leaving at $x +$

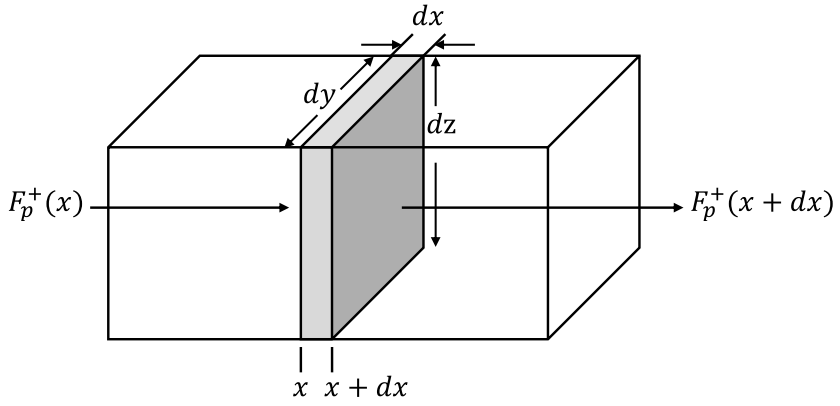

Figure 13. Differential volume showing x component of the x-component hole flux.

dx, as depicted in Figure 13. The net change in the number of holes per unit time in the differential volume element is:

$$\frac{\partial p(t)}{\partial t} dxdydz = -\frac{\partial F_p^+}{\partial x} dxdydz + G_p dxdydz - R_p dxdydz \,. \tag{34}$$

On the right hand side of equation (34), the first term represents the net increase in the number of holes per unit time due to x-component hole flux, the second term represents the increase in the numbers of holes per unit time due to the generation of holes, and the third term represents the decrease in the number of holes per unit time due to the recombination of holes. Given the hole flux

$$F_p^+ = \frac{J_p}{e}, \tag{35}$$

where J_p is the hole current density and $e = 1.6 \times 10^{-19}\ Coulomb$, the net change in the hole concentration per unit time, i.e. the continuity equation for holes, is

$$\frac{\partial p(t)}{\partial t} = -\frac{1}{e}\frac{\partial J_p}{\partial x} + G_p - R_p \,. \tag{36}$$

By the same token, the continuity equation for electrons is

$$\frac{\partial n(t)}{\partial t} = \frac{1}{e}\frac{\partial J_n}{\partial x} + G_n - R_n \,. \tag{37}$$

Recall that the hole and electron current densities are

$$J_p = e\mu_p pE - eD_p \frac{\partial p}{\partial x} \tag{38}$$

$$J_n = e\mu_n nE + eD_e \frac{\partial n}{\partial x}. \tag{39}$$

Substitute equations (38) and (39) in the continuity equations (36) and (37), the time-dependent diffusion equations for hole and electrons are

$$\frac{\partial p(t)}{\partial t} = D_p \frac{\partial p^2}{\partial x^2} - \mu_p \left(E \frac{\partial p}{\partial x} + p \frac{\partial E}{\partial x} \right) + G_p - R_p \tag{40}$$

$$\frac{\partial n(t)}{\partial t} = D_n \frac{\partial n^2}{\partial x^2} + \mu_n \left(E \frac{\partial n}{\partial x} + n \frac{\partial E}{\partial x} \right) + G_n - R_n \,, \tag{41}$$

which describe the space and time behavior of the excess carriers.

Under some particular scenarios, the electrons and holes tend to drift or diffuse with a single effective mobility or diffusion coefficient, which is called ambipolar transport. For example, under applied external electric field E_{app}, the excess electrons and holes created by either electrical injection or light illumination, are prone to drift in the opposite directions. The separation of these charged carriers induces an internal electric field opposite to the applied external electric field, as depicted in Figure 14. The induced internal electric field attract the electrons and holes move toward each other, holding them together; therefore, the electric filed appears in the equations (40) and (41) are composed of the external and internal electric fields. For another example, without external electric field, only light illumination on the semiconductor surface, the excess electrons and holes generated at the surface tend to diffuse toward lower concentration region due to

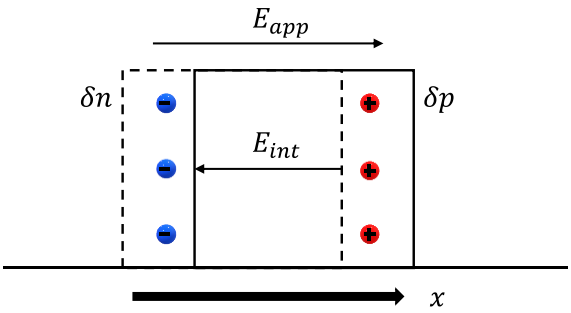

Figure 14. The creation of internal electric field as excess electrons and holes are separated.

concentration gradient. The difference in the mobilities separates them, creating the internal electric field, which also attracts them at the same time. To relate the excess electrons and holes to the internal electric field, Poisson's equation is introduced,

$$\nabla E_{int} = \frac{e(\delta p - \delta n)}{\varepsilon_s} = \frac{\partial E_{int}}{\partial x}, \tag{42}$$

where ε_s is the permittivity of the semiconductor and E_{int} is the internal electric field. Usually the strength of E_{int} is much smaller than that of external electric field, $|E_{app}| \gg |E_{int}|$, and thus is negligible. Since n_0 and p_0 are independent on time and space in equations (24) and (25), equations (40) and (41) can be rewritten as

$$\frac{\partial \delta p(t)}{\partial t} = D_p \frac{\partial \delta p^2}{\partial x^2} - \mu_p \left(E \frac{\partial \delta p}{\partial x} + p \frac{\partial E}{\partial x} \right) + G_p - R_p \tag{43}$$

$$\frac{\partial \delta n(t)}{\partial t} = D_n \frac{\partial \delta n^2}{\partial x^2} + \mu_n \left(E \frac{\partial \delta n}{\partial x} + n \frac{\partial E}{\partial x} \right) + G_n - R_n . \tag{44}$$

Since $\delta n = \delta p$, $G_n = G_p = G$, and $R_n = R_p = R$, combining these two equations and eliminating $\frac{\partial E}{\partial x}$ gives

$$\frac{\partial \delta n(t)}{\partial t} = D_{amb} \frac{\partial \delta n^2}{\partial x^2} + \mu_{amb} E \frac{\partial \delta n}{\partial x} + G - R , \tag{45}$$

where D_{amb} is the ambipolar diffusion coefficient and μ_{amb} is the ambipolar mobility, which expressions are as followed

$$D_{amb} = \frac{\mu_n n D_p + \mu_p p D_n}{\mu_n n + \mu_p p} \tag{46}$$

$$\mu_{amb} = \frac{\mu_n \mu_p (p - n)}{\mu_n n + \mu_p p} . \tag{47}$$

The Einstein relation relates the mobility and diffusion coefficient as shown below

$$\frac{\mu}{D} = \frac{e}{kT}. \tag{48}$$

The ambipolar diffusion coefficient can be expressed in the form

$$D_{amb} = \frac{D_n D_p (p+n)}{D_n n + D_p p}. \tag{49}$$

3.4 Physical Model of Vertical Carrier Transport

The working principle of the study of vertical hole transport by PL spectroscopy is illustrated in Figure 15. In this experiment, a long-wave probe region, consisting of LWIR T2SLs (LWSLs), is sandwiched between a bottom barrier and a MWIR T2SLs (MWSLs) transport region. When the MWSLs are excited by a continuous-wave or pulsed laser,

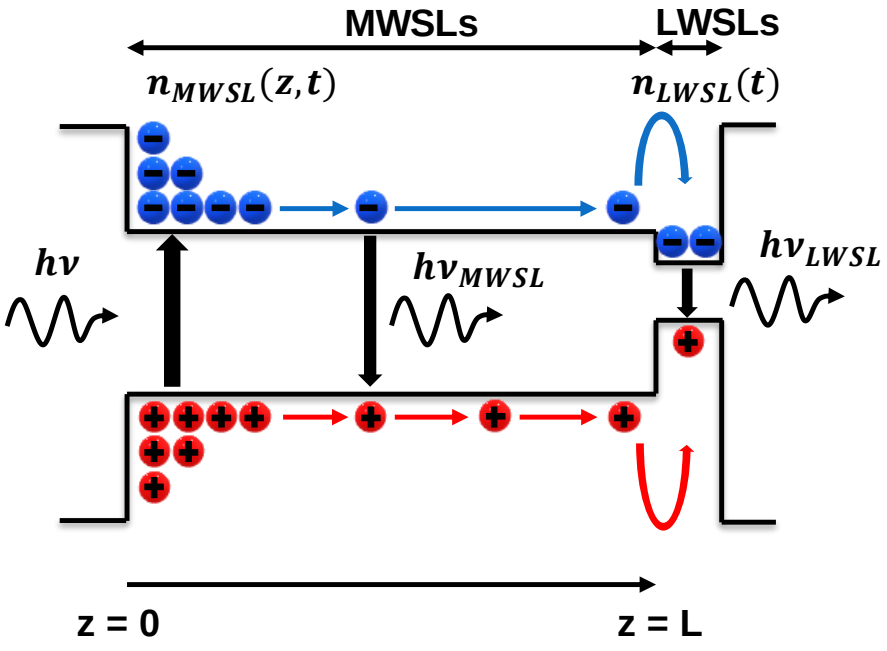

Figure 15. Schematic diagram illustrating the study of vertical carrier transport in MWSLs by PL spectroscopy. The vertical photocarrier transport in $InAs/InAs_{1-x}Sb_x$ MWSLs is limited by the slower hole transport.

photogenerated carriers will recombine to give PL in the MWSL region while diffusing vertically toward the probe region. If the carrier lifetime in the MWSLs is longer than the transport time across this region, a substantial amount of surviving carriers will be captured by the probe region and recombine there, giving rise to luminescence at a wavelength ($h\nu_{\mathrm{LWSL}}$) longer than that of the PL ($h\nu_{\mathrm{MWSL}}$) from the MWSLs. Information about the vertical carrier transport in the MWSL region can then be retrieved from either the intensity ratio of the luminescence from two different regions or the decay profile of the photoluminescence from the LWSL probe region. The carrier transport dynamics in both MWSLs and LWSLs can be described by an ambipolar diffusion equation, which is derived in equation (45), assuming no external electric field,

$$\frac{\partial n(z,t)}{\partial t} = D_{amb}\frac{\partial^2 n(z,t)}{\partial z^2} + \frac{\partial n(z,t)}{\partial t}\Big|_{gen} + \frac{\partial n(z,t)}{\partial t}\Big|_{rec}, \tag{50}$$

where $n(z,t)$ in equation (50) is the excess electron-hole pair density, D_{amb} is the ambipolar diffusion coefficient, $\frac{\partial n(z,t)}{\partial t}\Big|_{gen}$ is the generation term, and $\frac{\partial n(z,t)}{\partial t}\Big|_{rec}$ is the recombination term. The equation (50) can also be written in different forms for MWSLs and LWSLs, respectively. In MWSLs, the general equation is [61]

$$\frac{\partial n_{MWSL}(z,t)}{\partial t} = J(z) - \frac{n_{MWSL}(z,t)}{\tau_{MWSL}} + D_{amb}\frac{\partial^2 n_{MWSL}(z,t)}{\partial z^2}, \tag{51}$$

where $J(z)$ is the carrier generation rate from the laser and τ_{MWSL} is carrier lifetimes in MWSLs. Since the structure is sandwiched by $In_{0.9}Ga_{0.1}As$ or AlSb barriers, carriers reaching the top surface will be reflected without any carrier loss due to surface recombination. On the other hand, for LWSLs, the carrier diffusion is ignored due to

relatively thin thickness (100 nm), compared with that of MWSLs (at least 3.5 μm), and high internal quantum efficiency. Also, no direct excitation from laser is assumed,

$$\frac{\partial n_{LWSL}(t)}{\partial t} = -\frac{n_{LWSL}(t)}{\tau_{LWSL}} + D_{amb}\left|\frac{\partial n_{MWSL}(z,t)}{\partial z}\right|_{z=L}\Bigg|, \tag{52}$$

where $D_{amb}\left|\frac{\partial n_{MWSL}(z,t)}{\partial z}\right|_{z=L}\Bigg|$ is the carrier injection from MWSLs into LWSLs due to ambipolar diffusion, L is the thickness of MWSLs, and τ_{LWSL} is the carrier lifetimes in LWSLs. Here, the capture time of carriers by LWSLs is neglected because it has been reported that the capture time for electrons and holes is less than 1 ps [59], [65], significantly faster than transport time, meaning when carriers diffusing into the interface of MWSLs and LWSLs will be captured by LWSLs immediately without carrier accumulation.

In the following sections, steady-state and transient behaviors are measured by SSPL with continuous wave (CW) laser excitation, and TRPL with a pulse laser excitation, respectively. Under steady-state condition, equations (51) and (52) become

$$0 = J(z) - \frac{n_{MWSL}(z)}{\tau_{MWSL}} + D_{amb}\frac{\partial^2 n_{MWSL}(z)}{\partial z^2} \tag{53}$$

$$0 = -\frac{n_{LWSL}}{\tau_{LWSL}} + D_{amb}\left|\frac{\partial n_{MWSL}(z,t)}{\partial z}\right|_{z=L}\Bigg|, \tag{54}$$

where $J(z) = J_0 e^{-\alpha z}$ with $J_0 = \alpha\Phi$, where Φ is the photon flux and α is the absorption coefficient. While under pulse excitation condition, i.e. transient-state, equation (51) becomes

$$\frac{\partial n_{MWSL}(z,t)}{\partial t} = -\frac{n_{MWSL}(z,t)}{\tau_{MWSL}} + D_{amb}\frac{\partial^2 n_{MWSL}(z,t)}{\partial z^2}, \tag{55}$$

where the carrier generation rate J is zero and an initial condition of $n_{MWSL}(z,0) = n_0 e^{-\alpha z}$ (where $n_0 = 10^{18}$ cm^{-3} as an initial excess electron-hole pair density from a laser energy of 2.3 μJ/pulse), indicating the carrier dynamics in MWSLs we measured is after the short-pulse laser excitation. On the other hand, the transient behavior of carriers in LWSLs is still governed by equation (52).

3.5 Sample Structure for Transport Study

Two samples with different MWSL thickness were grown on GaSb (100) substrates by using MBE for this study. The sample structure consists of a 100-nm-thick LWSL and a MWSL regions sandwiched between two 10-nm-thick AlSb or $In_{0.9}Ga_{0.1}As$ barrier layers grown atop a 500-nm-thick GaSb buffer layer. The cross-section of the layer structure and schematic band diagram are shown in Figure 16. The MWSLs region is either 3.5 μm (sample A, B2622) or 4.5 μm (sample B, B2623) thick and comprises unintentionally doped n-type 2.14 nm/1.5 nm InAs/$InAs_{0.782}Sb_{0.218}$ T2SLs. The LWSL probe region is composed of 100-nm-thick undoped 9.78 nm/4.22 nm InAs/$InAs_{0.7}Sb_{0.3}$ T2SLs. The As/In flux ratio was kept constant at 1.2 during the growth while the Sb/In ratios were 1.08 and 0.41 for the growth of LWSLs and MWSLs, respectively, and the growth rate of InAs was fixed at 15 nm/min at a growth temperature of 450 ℃. The PL peak wavelength for MWSLs was designed to be at 4.1 μm, whereas the wavelength for the LWSL probe region was chosen to be at 8 μm to avoid strong water absorption, as discuss in chapter 1 and illustrated in Figure 2, and to be easily resolved spectrally from the PL of the MWSL region. Assuming the absorption coefficient of InAs/$InAs_{1-x}Sb_x$ T2SLs is $1.0 \times 10^4\ cm^{-1}$ at 785

nm and 1064 nm wavelength [74], the thinnest MWSLs in this study, i.e. 3.5 μm thick, is sufficiently thick that satisfy the assumption in which carriers will be generated only in MWSLs when laser illuminates on the top surface. Figure 17 illustrates the HRXRD (004) $\omega - 2\theta$ profile and simulation for sample A, in which the satellite peaks for MWSLs and LWSLs are sharp and well-defined. The Pendellösung fringes shown in the XRD profile indicate excellent crystalline quality and abrupt interfaces. Furthermore, the zeroth order peaks of MWSLs and LWSLs are aligned well with the substrate peak, indicating that the T2SLs were strain-balanced, a necessity for growing thick layer without generating misfit dislocations. The extracted parameters, taken from the best fit by X'pert Epitaxy, are

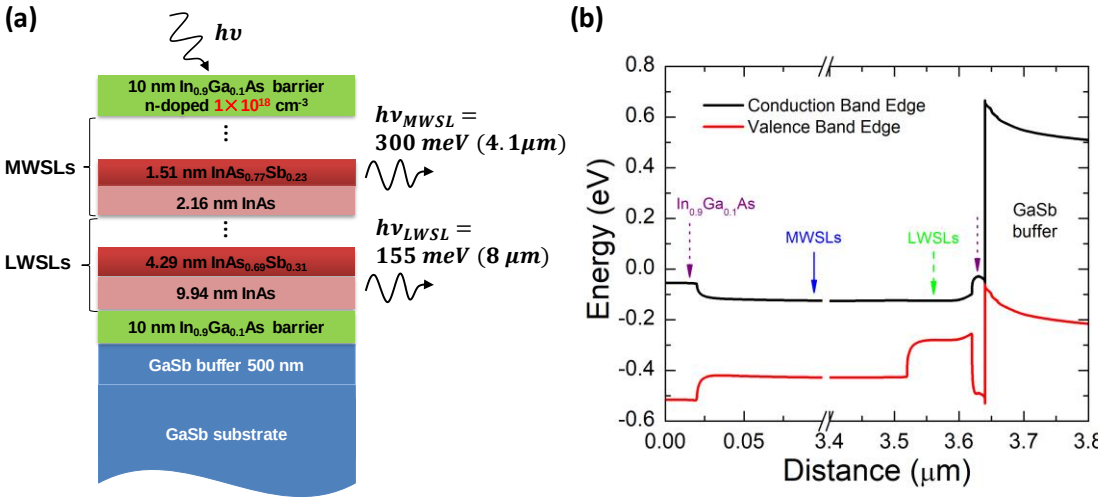

Figure 16. (a) Schematic layer structure of the MBE-grown sample. The top $In_{0.9}Ga_{0.1}As$ barrier layer was doped to 1×10^{18} cm^{-3} to achieve a flat band in MWSLs. and (b) band edge alignment of sample A calculated using one-dimensional drift-diffusion model, demonstrating the conduction and valence band alignment of $In_{0.9}Ga_{0.1}As$ barriers, MWSLs, LWSLs, and GaSb buffer. The top surface of the sample is at 0 µm. This simulation reveals flat energy bands for the MWSL region, which justifies the use of a pure diffusion model in the main text.

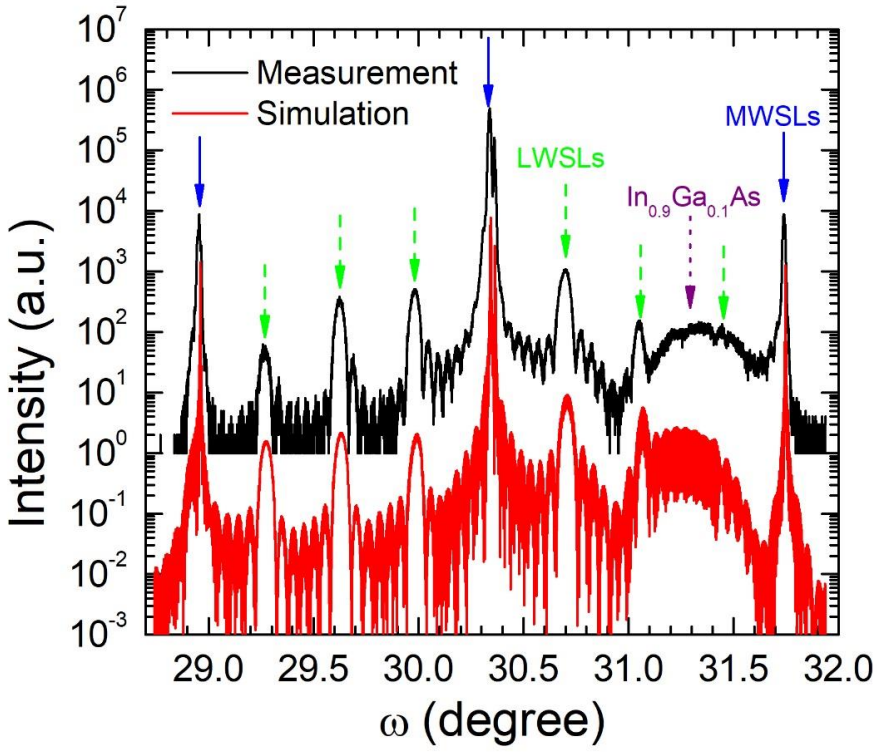

Figure 17. $\omega - 2\theta$ XRD of sample A for vertical carrier transport study. Black and red lines illustrate the measured and simulated curves, respectively. The peaks for LWSLs, MWSLs and $In_{0.9}Ga_{0.1}As$ barrier are as indicated by different arrows.

summarized in Table 4, which reveals the consistency between the design and measurement.

Table 4. The extracted parameters from the best fit of (004) XRD, indicating the consistency between the design and measurement.

Layer	Measurement (XRD)			Design		
	InAs (nm)	$InAs_{1-x}Sb_x$ (nm)	x	InAs (nm)	$InAs_{1-x}Sb_x$ (nm)	x
LWSLs	9.94	4.29	0.31	9.78	4.22	0.3
MWSLs	2.16	1.51	0.23	2.14	1.5	0.218

3.6 Steady-state Photoluminescence Analysis of Carrier Transport

The temperature-dependent SSPL spectra of sample A and B were measured by using a Nicolet 760 Fourier transform infrared (FTIR) spectrometer, equipped with a liquid-nitrogen cooled HgCdTe detector, and a continuous-wave laser diode with excitation wavelength of 785 nm and pump power of 6 W/cm^2. The excited carrier density in MWSLs was ~5×10^{15} cm^{-3}. Figure 18 shows the SSPL of sample A recorded from 12 K to 210 K. The SSPL spectra for sample B are similar to those of sample A and can be found in Figure 19. In general, all spectra feature both 4.1 μm ($h\nu_{MWSL}$) and 8 μm ($h\nu_{LWSL}$) PL peaks. The

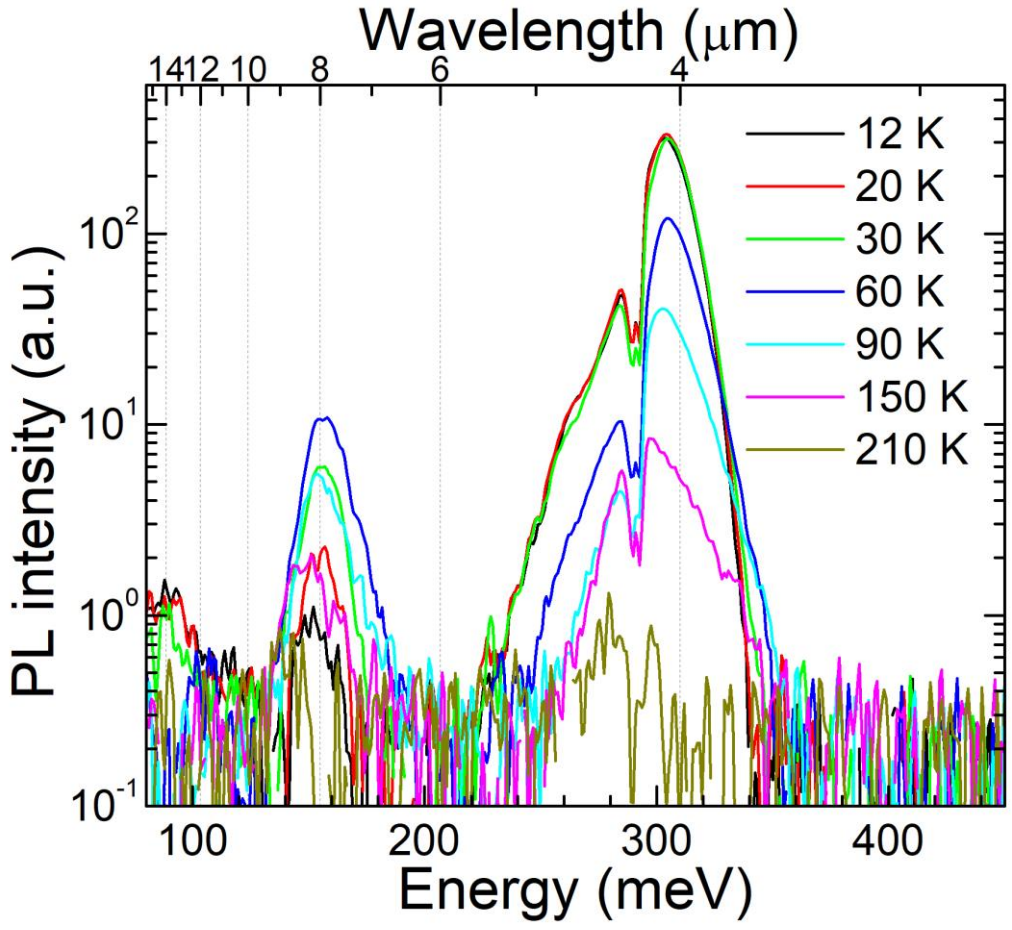

Figure 18. SSPL of sample A taken at various temperatures. Both MWIR and LWIR are observed, indicating carrier diffusion of photogenerated carriers in MWSL into LWSL region.

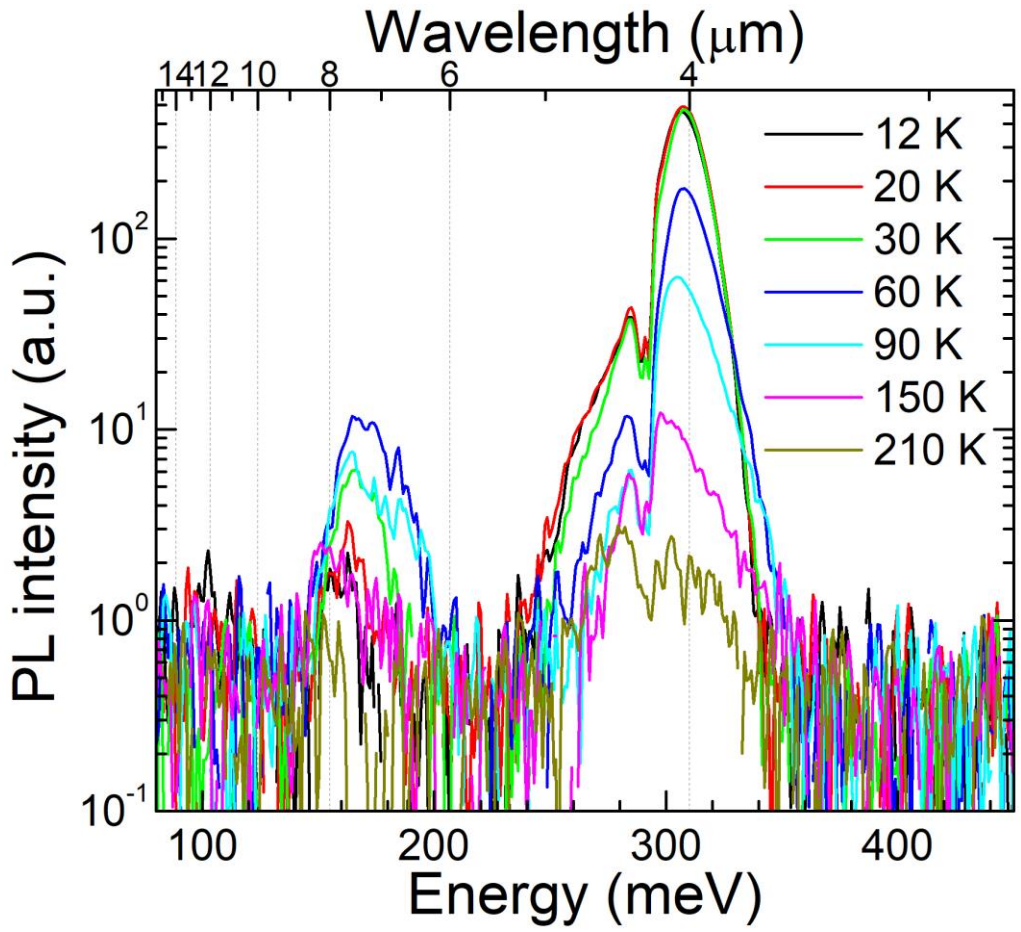

Figure 19. Temperature-dependent SSPL spectra of sample B (4.5 μm thick). The peaks at 4.1 μm and 7.5 μm are the emission peaks of MWSL and LWSL, respectively. The slight shift of LWSL peak wavelength of sample B from that of sample A is due to the variation of Sb composition in InAsSb layer. However, this difference will not affect the assumptions and calculations described in the main text.

dips at ~4.2 μm near the MWSL peaks are due to the atmospheric CO_2 absorption. The MWSL peak consistently shows a higher intensity than the LWSL peak at the same temperature. This discrepancy in intensity suggests that a substantial number of excited carriers recombine in the MWSL region. The LWSL peak intensity is vanishingly small at 12 K, indicating that there is essentially no direct excitation of the probe region by the 785 nm laser light, and thus almost all photogenerated holes recombines in the MWSL region.

This characteristic is expected since the estimated laser penetration depth, ~1 μm by assuming an absorption coefficient α of 10^4 cm^{-1}, is at least three times smaller than the MWSL region thickness in sample A and B. To further verify the assumption, the PL from a sample with a 2-μm thick MWSL region was recorded in Figure 20 where the LWSL peak at 7.5 μm shows different temperature trend with respect to sample A and B. At temperature of 12 K, the intensity of LWSL peak is as pronounced as that of MWSL peak,

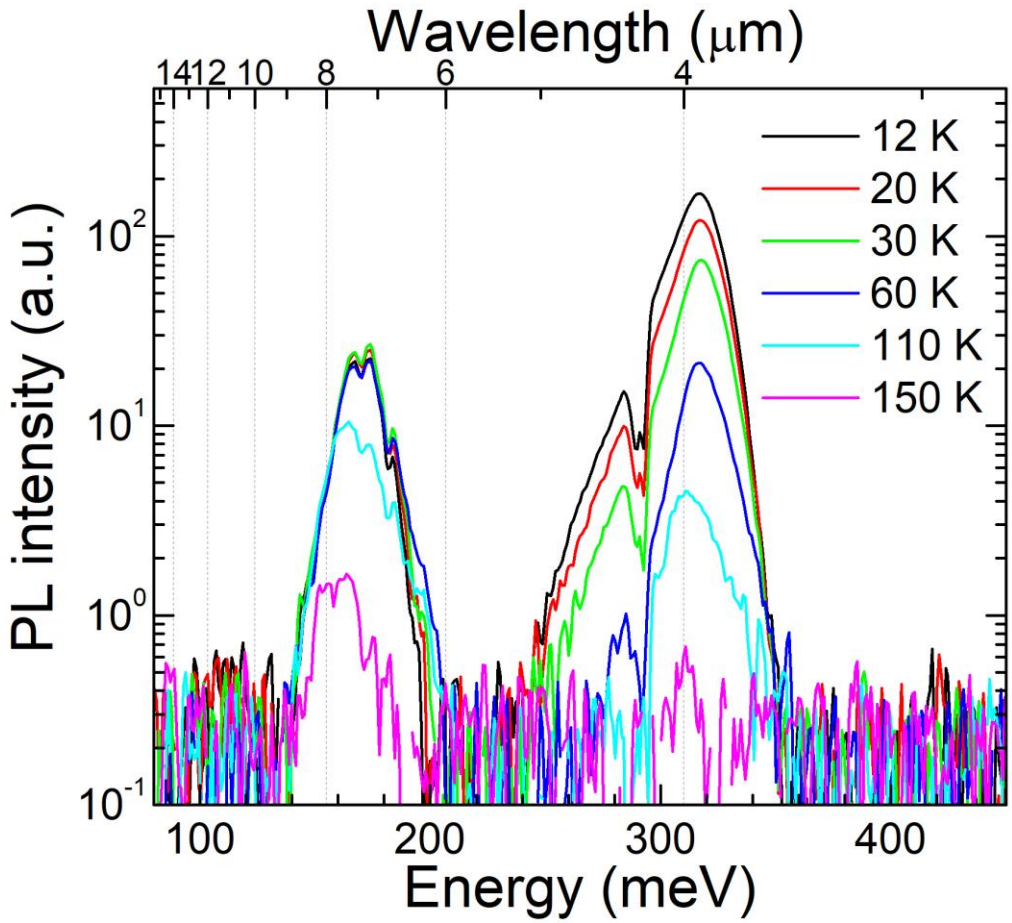

Figure 20. Temperature-dependent SSPL spectra of a sample with 2 μm thick MWSL region. The LWSL peak at 7.5 μm shows different temperature trend with respect to sample A and B. At temperature of 12 K, the intensity of LWSL peak is as pronounced as that of MWSL peak, strongly evidencing the co-excitation of two regions in the sample with 2 μm thick MWSL region.

strongly evidencing the direct excitation of probe regions in the sample with 2 μm thick MWSL region.

To gain more insight into the temperature dependence of the transport property, the integrated intensities of MWSL and LWSL PL peaks, I_{MWSL} and I_{LWSL}, are plotted as a function of temperature in Figure 21 and 22 for samples A and B, respectively. The temperature-dependent behavior for both samples shows pretty much identical trend, also suggesting decent MBE run-to-run growth uniformity. I_{MWSL} remains constant for

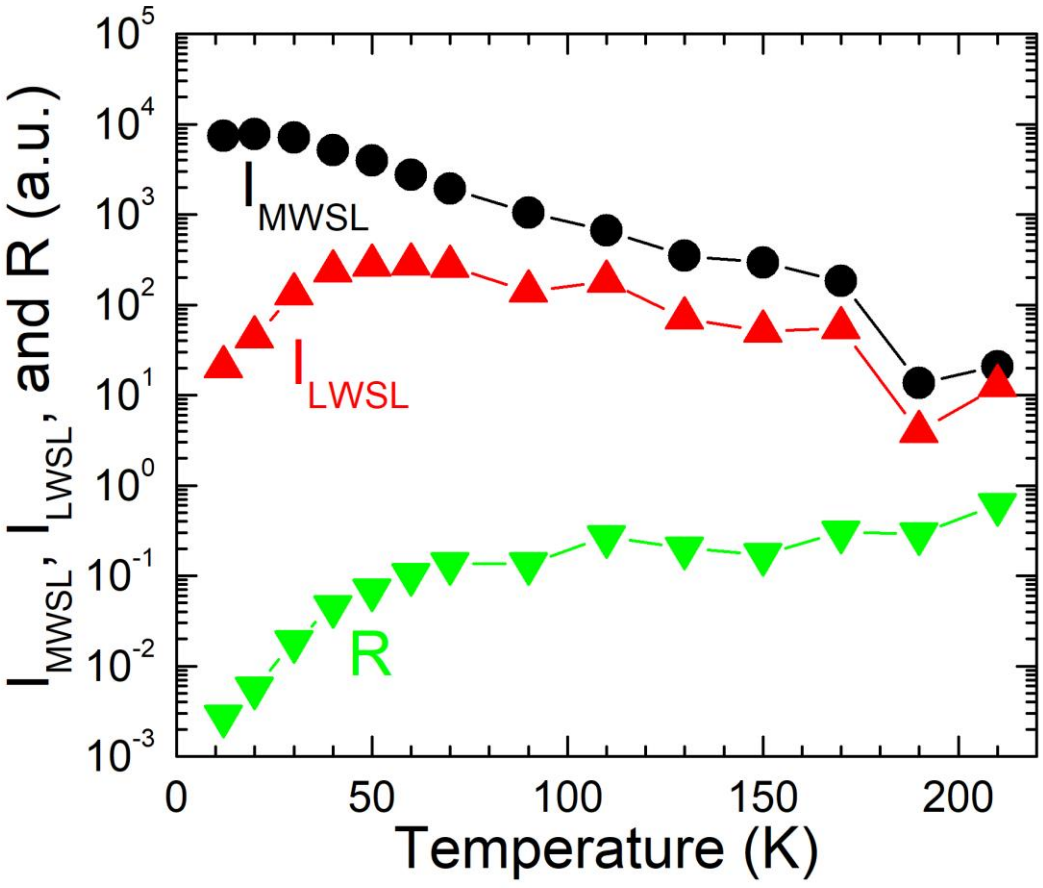

Figure 21. The integrated luminescence intensities of MWSLs (I_{MWSL}) and LWSLs (I_{LWSL}), and the ratio $R = I_{LWSL}/I_{MWSL}$ of sample A at various temperatures extracted from the temperature-dependent luminescence spectra (figure 18).

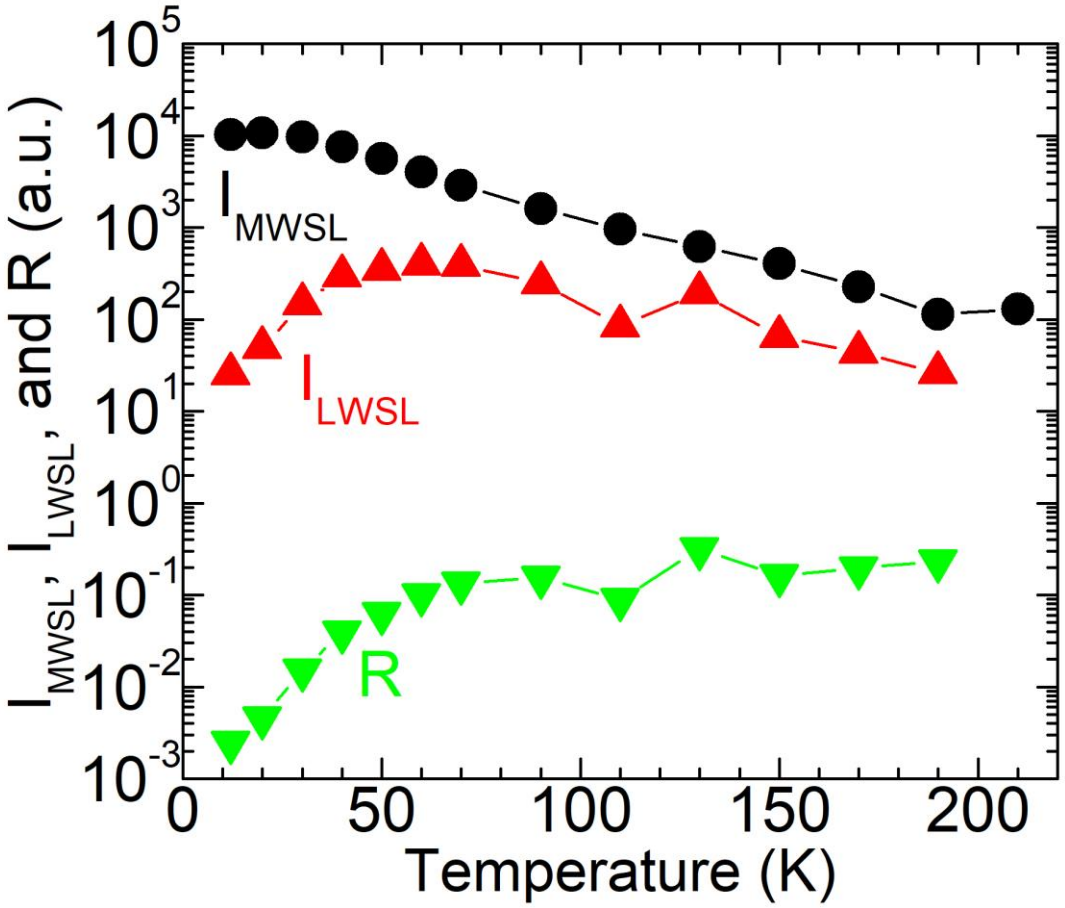

Figure 22. The integrated luminescence intensities of MWSLs (I_{MWSL}) and LWSLs (I_{LWSL}), and the ratio $R = I_{LWSL}/I_{MWSL}$ of sample B at various temperatures extracted from the temperature-dependent luminescence spectra (figure 19).

temperatures from 12 K to 30 K, indicating the luminescence efficiency is almost unity and non-radiative recombination is suppressed. As the temperature further increases, I_{MWSL} shows a monotonic decrease whereas the temperature dependence of I_{LWSL} clearly exhibits two distinct regimes. Below ~60 K, I_{LWSL} increases steeply with temperature, indicating that more photogenerated holes are transported to the LWSL probe region as hole mobility in the MWSL region is increased with temperature; above ~60 K, I_{LWSL} resembles the trend

of I_{MWSL}, indicating that the emission from the probe region switches from hole density limited to hole lifetime limited emission. To uncover the correlation between the MWSL and LWSL peaks, the ratio $R = I_{LWSL}/I_{MWSL}$ is also plotted in Figure 21 and 22 for samples A and B, respectively. The ratio increases by two orders of magnitude from 12 K to 60 K and levels off with further increase in temperature, clearly illustrating thermally enhanced hole transport in the MWSL region at low temperature.

Previously, it has been reported that InAs/$InAs_{1-x}Sb_x$ T2SLs suffer from carrier localization at low temperatures due to the fluctuations of layer thickness and Sb

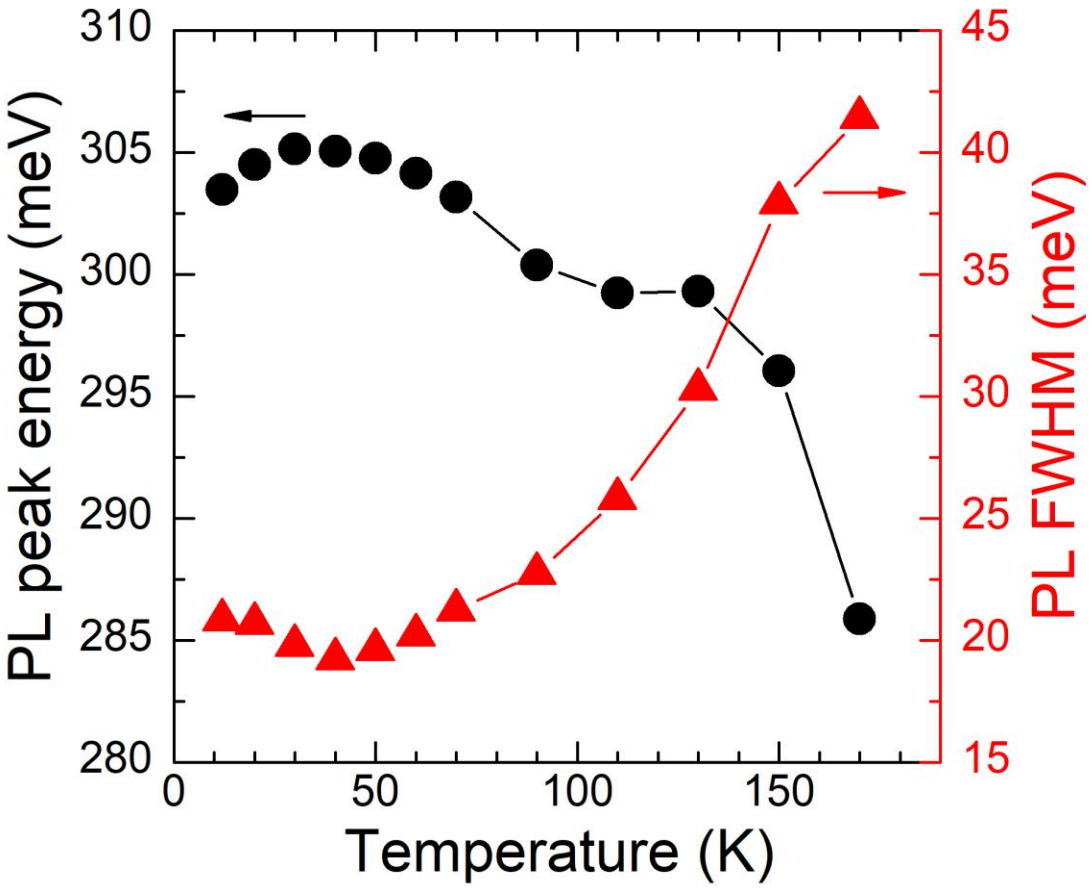

Figure 23. MWSL PL peak energy and FWHM of sample A as a function of temperature.

composition [42], [75]. The effect of carrier localization is more prominent in MWSLs as the thickness of each period is usually much thinner than that in LWSLs [42], [75]. In this study, starting from 12 K the MWSLs PL peak energy initially increased and then decreased monotonically with temperature, which is accompanied by the initial decrease and then increase of the full width at half maximum (FWHM) of the PL peaks (Figure 23 and 24). Both are clear signatures of carrier localization. It is speculated that this carrier localization likely leads to a significant reduction in the carrier (especially hole) mobility. As a result, the majority of photogenerated electron-hole pairs recombine in the MWSL

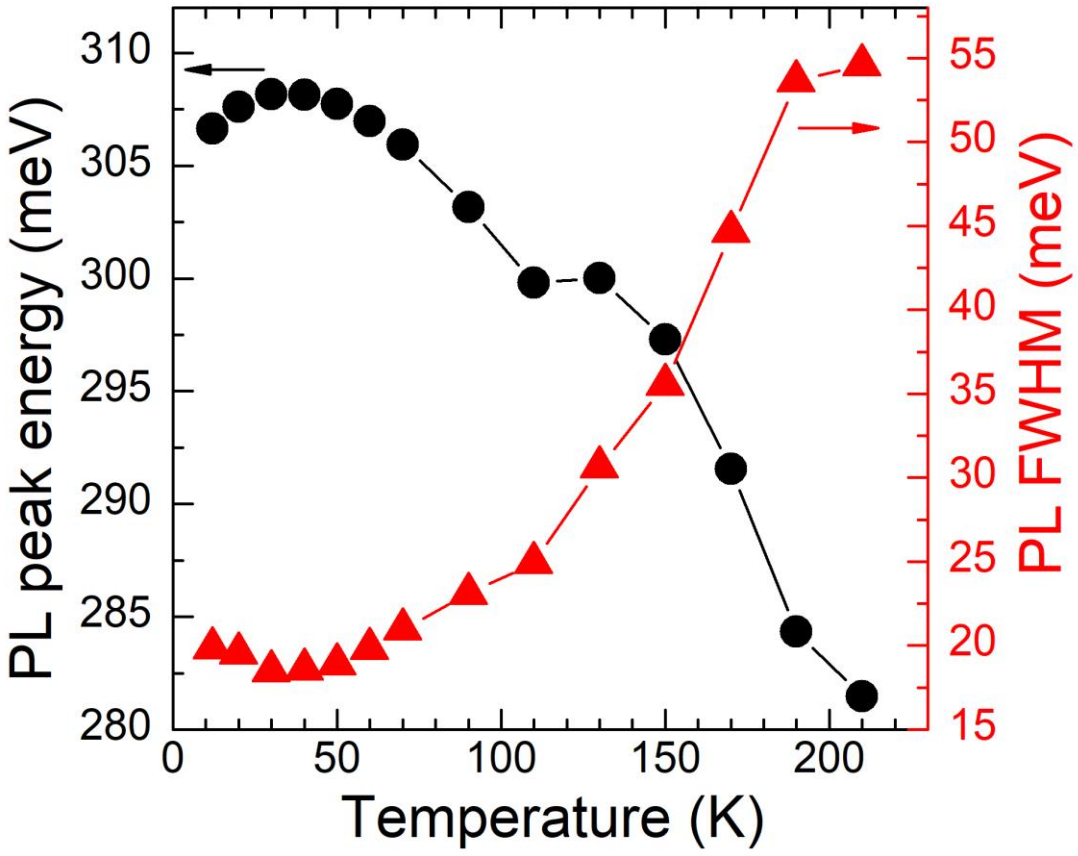

Figure 24. MWSL PL peak energy and FWHM of sample B as a function of temperature.

region at 12 K. As the temperature increases, more and more carriers are freed from localized states due to thermalization and diffuse into the probe region to recombine with electrons there, giving rise to a steep increase in luminescence intensity. Above 60 K, the ratio saturates with temperature, indicating that the carrier transport in MWSLs is no longer limited by carrier localization.

The PL peak and FWHM are exacted from Figure 23 and 24 by using bi-gaussian peak expression:

$$I = I_0 + He^{-\frac{1}{2}(\frac{x-x_c}{w_1})^2} \quad (x < x_c) \tag{56}$$

$$I = I_0 + He^{-\frac{1}{2}(\frac{x-x_c}{w_2})^2} \quad (x \geq x_c)\,, \tag{57}$$

where I is the PL intensity per unit photon energy, I_0 is the background intensity, H is the peak intensity, x_c is the peak center in unit of photon energy, and w_1 and w_2 are the two widths for the two sides of the PL profile which has different slopes on low- and high-energy sides. The high-energy side represents the carrier distribution, which is obtained by multiplying Fermi-Dirac distribution with the density of state; therefore, the width and slope of the high-energy side of PL are a function of temperature and the PL width broadens with decreasing temperature. For the low-energy side, it represents the band tails in the joint density of states, which are due to impurity states at the band edge or compositional inhomogeneity. Since they are less temperature sensitive, usually the slope and width of the low-energy side are constant over a wide temperature range.

Since both electrons and holes diffuse toward the probe region after photogeneration, and the difference in the electron and hole mobilities is large, it is an ambipolar diffusion

process and the carrier dynamics can be described by equation (52) and (55) with the following boundary conditions:

$$n_{MWSL}(z)|_{z=L} = 0 \tag{58}$$

$$\left.\frac{dn_{MWSL}(z)}{dz}\right|_{z=0} = 0\,, \tag{59}$$

where z is the distance into MWSLs and $z = 0$ is the surface of the sample as shown in Figure 16(a).

By solving equation (52) and equation (55) in steady-state with boundary conditions given in (58) and (59), one can obtain the excess electron-hole pair densities in MWSL and LWSL regions. The detailed derivation is shown as follow. From the equation (55),

$$\frac{\partial^2 n_{MWSL}(z)}{\partial z^2} - \frac{n_{MWSL}(z)}{D_{amb}\tau_{MWSL}} = -\frac{J_0 e^{-\alpha z}}{D_{amb}}\,. \tag{60}$$

Equation (60) is a non-homogeneous differential equation with a solution of $n_{MWSL}(z) = n_h(z) + n_p(z)$, where $n_h(z)$ is the homogeneous solution and $n_p(z)$ is the particular solution for the non-homogenous part. For the homogeneous part,

$$\frac{\partial^2 n_h(z)}{\partial z^2} - \frac{n_h(z)}{D_{amb}\tau_{MWSL}} = 0\,. \tag{61}$$

$n_h(z)$ can be solved from equation (61), which yields

$$n_h(z) = C_1 e^{z/L_D} + C_2 e^{-z/L_D}\,, \tag{62}$$

where L_D is the carrier diffusion length with $L_D = \sqrt{D_{amb}\tau_{MWSL}}$; C_1 and C_2 are constants which will be determined later. For the non-homogeneous part, $n_p(z) = K \cdot \frac{J_0 e^{-\alpha z}}{D_{amb}}$ is assumed. The secondary derivative of $n_p(z)$ yields

$$n_p''(z) = K \cdot \frac{J_0 e^{-\alpha z}}{D_{amb}} \cdot \alpha^2 \,. \tag{63}$$

Plug equation (63) back to equation (60) yields

$$K \cdot \frac{J_0 e^{-\alpha z}}{D_{amb}} \cdot \alpha^2 - K \cdot \frac{J_0 e^{-\alpha z}}{D_{amb}} \cdot \frac{1}{D_{amb}\tau_{MWSL}} = -\frac{J_0 e^{-\alpha z}}{D_{amb}} \,. \tag{64}$$

One can obtain

$$K = \frac{L_D^2}{1 - L_D^2 \alpha^2} \,, \tag{65}$$

and

$$n_p(z) = K \cdot \frac{J_0 e^{-\alpha z}}{D_{amb}} = \frac{L_D^2}{1 - L_D^2 \alpha^2} \cdot \frac{J_0 e^{-\alpha z}}{D_{amb}} = \frac{J_0 \tau_{MWSL}}{1 - L_D^2 \alpha^2} e^{-\alpha z} \,, \tag{66}$$

Therefore, the general solution becomes

$$n_{MWSL}(z) = n_h(z) + n_p(z) = C_1 e^{z/L_D} + C_2 e^{-z/L_D} + \frac{J_0 \tau_{MWSL}}{1 - L_D^2 \alpha^2} e^{-\alpha z} \,. \tag{67}$$

However, when $\alpha = 1/L_D$, the generation solution takes a different form because the assumption of particular solution $n_p(z) = K \cdot \frac{J_0 e^{-\alpha z}}{D_{amb}}$ becomes part of the homogeneous solution and a divergent point occurs in equation (67). Hence, if $\alpha = 1/L_D$, the particular solution $n_p(z) = K \cdot z \cdot \frac{J_0 e^{-\alpha z}}{D_{amb}}$ is assumed. By doing similar procedure from equation (63) to equation (66), one can obtain $K = 1/2\alpha$ and $n_p(z) = \frac{J_0}{2\alpha D_{amb}} \cdot z \cdot e^{-\alpha z}$. In this study, as the 785 nm laser penetration depth (~1 μm) is smaller than the carrier diffusion length, the $L_D^2 \alpha^2$ term in equation (66) is always larger than 1 and $n_{MWSL}(z)$ is continuous across the

MWSL region. In the following paragraph, only equation (66) will be discussed. The equation (67) can be normalized as

$$n_{MWSL}(z) = \frac{J_0 \tau_{MWSL}}{1 - L_D^2 \alpha^2} \left(A e^{z/L_D} + B e^{-z/L_D} + e^{-\alpha z} \right), \tag{68}$$

where A and B are constants which can be determined by plugging equation (68) into two boundary conditions [equation (58) and (59)], from where one can obtain

$$A = B + \alpha L_D \; and \; A e^{L/L_D} + B e^{-L/L_D} = -e^{-\alpha L}. \tag{69}$$

Solving A and B from equation (69) yields

$$A = \frac{\alpha L_D e^{-L/L_D} - e^{-\alpha L}}{e^{L/L_D} + e^{-L/L_D}} \tag{70}$$

$$B = \frac{-(\alpha L_D e^{L/L_D} + e^{-\alpha L})}{e^{L/L_D} + e^{-L/L_D}}. \tag{71}$$

Also, from equation (54), the excess electron-hole pair density n_{LWSL} can be obtained

$$n_{LWSL} = \tau_{LWSL} D_{amb} \left| \frac{\partial n_{MWSL}(z)}{\partial z} \right|_{z=L} \Big|. \tag{72}$$

The integrated photoluminescence intensities in MWSL region, I_{MWSL}, can be defined as [65]

$$I_{MWSL} = \int_0^L \frac{n_{MWSL}(z)}{\tau_{MWSL}^R} dz = \int_0^L \eta_{MWSL} \frac{n_{MWSL}(z)}{\tau_{MWSL}} dz, \tag{73}$$

where τ_{MWSL}^R is radiative recombination carrier lifetimes in MWSLs and η_{MWSL} is the quantum efficiency of the radiative recombination process in MWSLs, which can be deduced as follow

$$\frac{1}{\tau_{MWSL}} = \frac{1}{\tau_{MWSL}^R} + \frac{1}{\tau_{MWSL}^{NR}} \tag{74}$$

$$\eta_{MWSL} = \frac{\tau_{MWSL}}{\tau^{R}_{MWSL}} = (1 + \frac{\tau^{R}_{MWSL}}{\tau^{NR}_{MWSL}})^{-1}\,, \tag{75}$$

where τ^{NR}_{MWSL} is the non-radiative recombination carrier lifetimes in MWSLs. Similarly, the integrated PL intensity in LWSLs, I_{LWSL}, is also determined by following equations

$$I_{LWSL} = \frac{n_{LWSL}}{\tau^{R}_{LWSL}} = \eta_{LWSL}\frac{n_{LWSL}}{\tau_{LWSL}} = \eta_{LWSL} D_{amb} \left|\frac{\partial n_{MWSL}(z)}{\partial z}\right|_{z=L}\Bigg| \tag{76}$$

$$\eta_{LWSL} = \frac{\tau_{LWSL}}{\tau^{R}_{LWSL}} = (1 + \frac{\tau^{R}_{LWSL}}{\tau^{NR}_{LWSL}})^{-1}\,. \tag{77}$$

Hence, the intensity ratio between I_{LWSL} and I_{MWSL} can be expressed as

$$R = \frac{I_{LWSL}}{I_{MWSL}} \tag{78}$$

$$= \frac{\eta_{LWSL} D_{amb} \left|\frac{\partial n_{MWSL}(z)}{\partial z}\right|_{z=L}\Bigg|}{\frac{J_0 \eta_{MWSL}}{1 - L_D^2 \alpha^2}\left(AL_D(e^{L/L_D} - 1) - BL_D(e^{-L/L_D} - 1) - \alpha^{-1}(e^{-\alpha L} - 1)\right)}\,.$$

Equation (78) shows that R is an explicit function of ambipolar diffusion coefficient D_{amb}, which is an effective coefficient describing the concurrent diffusion of electrons and holes (ambipolar diffusion) in MWSLs. D_{amb} is derived in equation (46) and reiterated here

$$D_{amb} = \frac{n\mu_e D_h + p\mu_h D_e}{n\mu_e + p\mu_h}\,, \tag{79}$$

where D_h and D_e are diffusion coefficients for hole and electron, respectively, and μ_h and μ_e are corresponding mobilities. Using 1 μm penetration depth and also taking into account a reflection of 33.5% at the sample interface, a photogenerated carrier density of 1×10^{16} cm^{-3} is obtained, which is one third of the background electron concentration (3×10^{16} cm^{-3} at 10 K [15]). The equation (79) can be rewritten as

$$D_{amb} = \frac{D_h + \frac{p\mu_h D_e}{n\mu_e}}{1 + \frac{p\mu_h}{n\mu_e}}. \quad (80)$$

For InAs/$InAs_{1-x}Sb_x$ T2SLs, the following assumptions generally hold, especially for the temperature range (>77 K) of strong interests for detector applications: $D_h \ll D_e$ and $\mu_h \ll \mu_e$. Using Einstein relation as described in equation (48) and considering that $\frac{p}{n} = \frac{1\times10^{16}}{1\times10^{16}+3\times10^{16}} = 0.25$, one can obtain $D_{amb} \cong 1.25\, D_h$, which is very close to $D_{amb} = D_h$. In general, the $D_{amb} = C \cdot D_h$, where $1 \leq C \leq 2; C = 1$ for very low level injection and $C = 2$ for very high level injection (e.g., pulse laser in TRPL measurements). This simple relationship between the ambipolar and hole diffusion coefficients suggests that although the diffusion process is ambipolar in nature, it is in effect regulated by the slow hole diffusion process. In principle, given other parameters remain the same, C is determined by the carrier lifetime, and thus is dependent on temperature. For simplicity and considering that the background electron concentration at temperatures higher than 10 K is likely larger than 3×10^{16} cm^{-3}, we use $C = 1$ for the extraction of mobilities for all the temperatures. This simplification used the assumption that the carrier transport in InAs/$InAs_{1-x}Sb_x$ T2SLs is limited by hole transport. This assumption is generally valid, considering that the electron diffuses across MWSLs via Bloch transport as the conduction band offset between InAs and $InAs_{0.782}Sb_{0.218}$ is 67 meV compared to 238 meV for valance band offset at 12 K [76]. In addition, it is assumed that η_{MWSL} and η_{LWSL} have similar temperature dependence and values such that they are canceled in equation (78). With these

assumptions, a numerical solution of D_h can be sought after from equation (78), and the vertical hole mobility can then be calculated by using Einstein relation, $D_h = \mu_h k_B T/e$.

In order to extract the vertical hole mobility by using equation (78), the carrier lifetimes of MWSLs have to be determined beforehand by using TRPL, which system setup will be discussed in detail in next section. Then the carrier lifetimes τ_{MWSL} can be plugged into $L_D = \sqrt{D_{amb}\tau_{MWSL}}$ which is used in equation (78). The temperature-dependent TRPL spectra and extracted carrier lifetimes of sample A and B are shown in Figure 25 and 26, respectively. These lifetimes were extracted from the TRPL data and much shorter than a previously measured carrier lifetime of 12.8 μs in a MWSL at 15 K reported in Ref. [15]. This discrepancy in the lifetime is mainly due to the measurement temperature difference and shorter periods in the MWSL region with a LWSL region acting as a photogenerated carrier collector at the bottom in samples A and B, which all shortened the carrier lifetime.

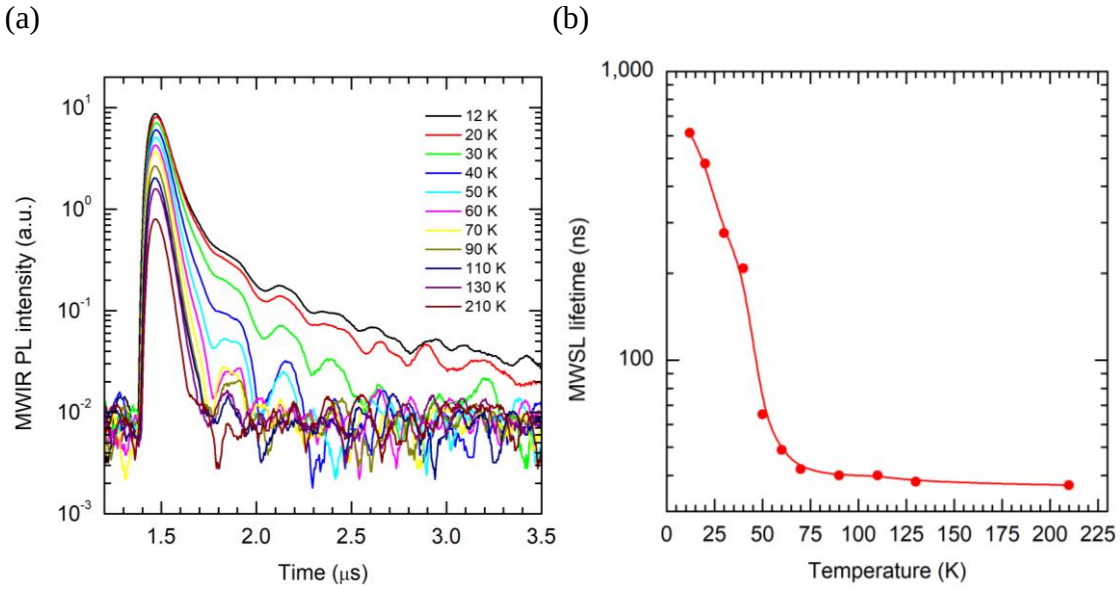

Figure 25. (a) Temperature-dependent TRPL spectra of sample A from 12 to 210 K. (b) The extracted τ_{MWSL} at various temperatures by fitting the curve in (a) with exponential decay function.

The extracted vertical hole mobilities in sample A and B are presented in Figure 27. In general, hole mobility in these two samples exhibits very similar temperature dependence, indicating decent run-to-run uniformity of strain-balanced MWSL growth of different thicknesses. The hole mobility takes on a value of ~0.2 cm^2/Vs at 12 K and rapidly reaches a saturation value of ~50 cm^2/Vs at 60 K, closely resembling the temperature dependence trend of *R* in Figure 21and 22. From previous discussion, it is found that the rapid increase in mobility below 60 K has been attributed to the thermally assisted hole delocalization from localized states. It is speculated that the mobility saturation above 60 K might be ascribed to interface scattering, originating from alternate InAs and $InAs_{1-x}Sb_x$ interfaces. This interface scattering has been considered as one of the dominant carrier scattering mechanisms in T2SLs along with impurity scattering [77].

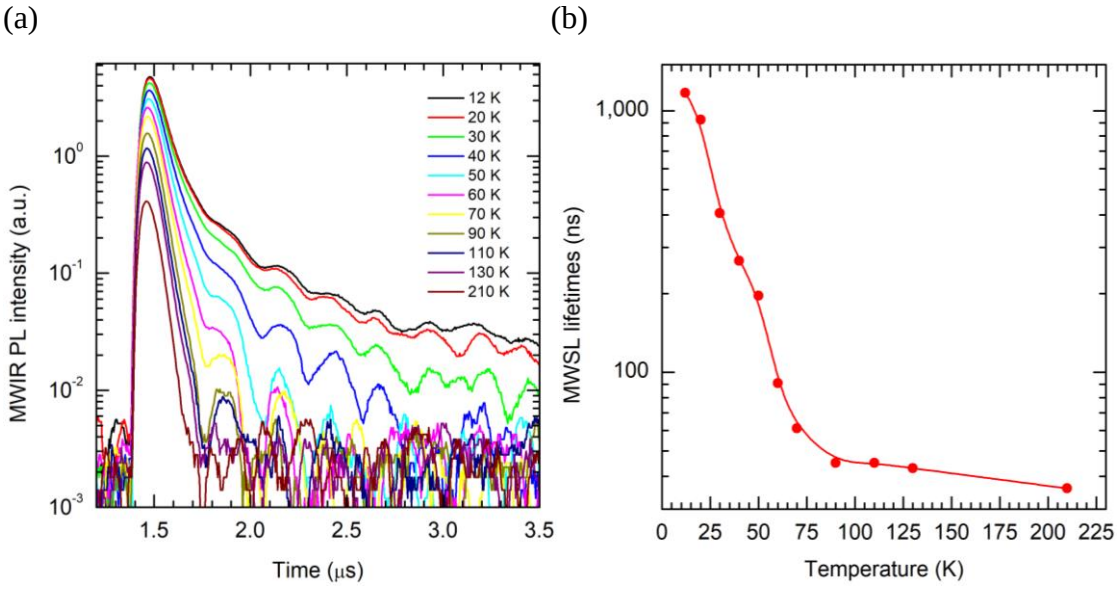

Figure 26. (a) Temperature-dependent TRPL spectra of sample B from 12 to 210 K. (b) The extracted τ_{MWSL} at various temperatures by fitting the curve in (a) with exponential decay function.

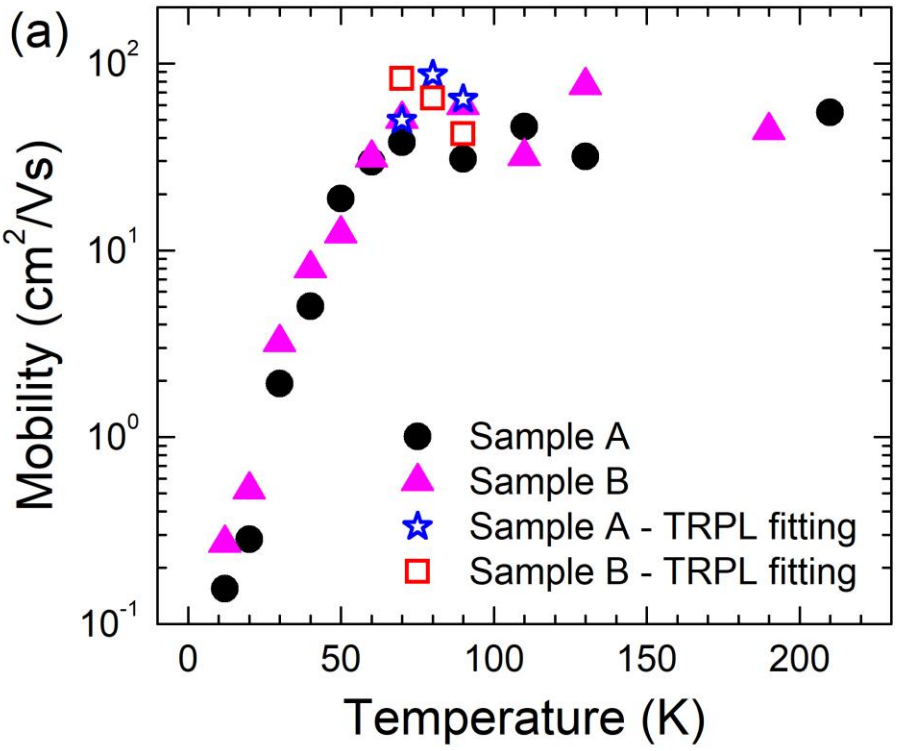

Figure 27. Extracted vertical hole mobilities of sample A (dot) and B (triangle) at temperatures ranging from 12 K to 210 K. The "star" and "square" denote the hole mobility resulting from a fitting to the TRPL data of sample A and B from 70 to 90 K (see text for details).

3.7 Transient Analysis of Carrier Transport

To verify the mobility data in Figure 27, the hole mobility is also evaluated by using TRPL spectroscopy. A block diagram of the experimental setup can be found in Figure 28. In this experiment, the sample is excited by a 1064 nm pulse laser with a repetition rate of 10 kHz and a pulse width of ~700 ps. The laser beam is further mechanically chopped at a frequency of 1 kHz for an enhanced signal-to-noise ratio [78]. The photoluminescence decay signal is detected by a high-speed (50 MHz) HgCdTe detector and then recovered by a boxcar averager. To get individual LWIR signal, a long-pass filter with a cut-on wavelength at 6.5 μm is inserted to wipe out the MWIR and other unwanted signals. The vertical hole mobility can be extracted by fitting the photoluminescence time decay profile

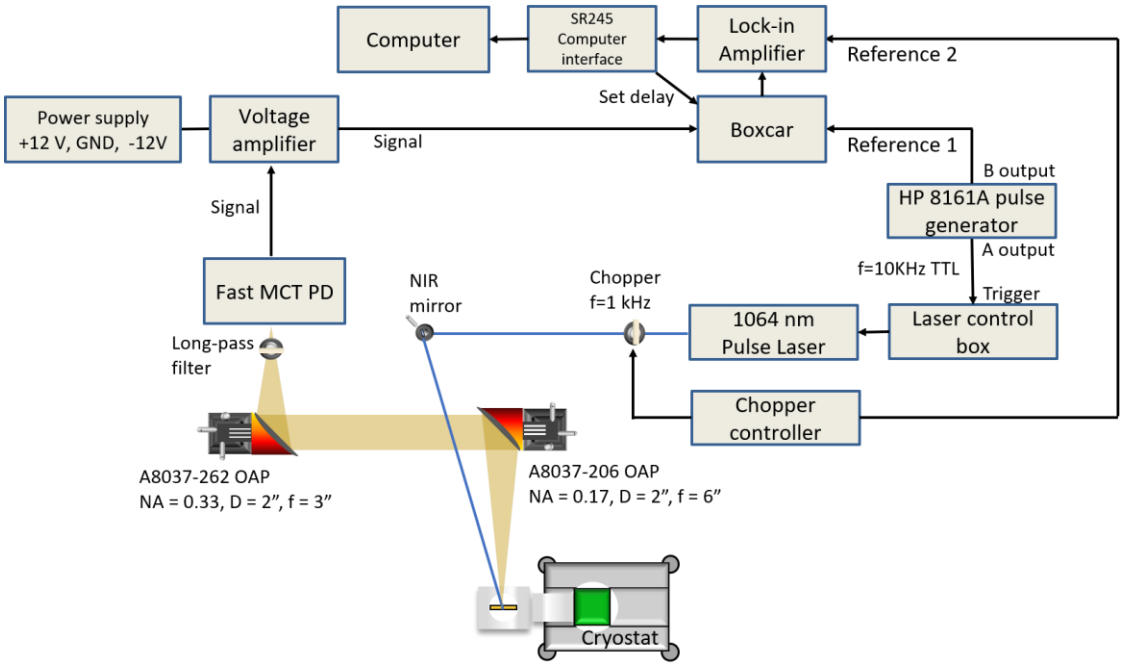

Figure 28. Schematic diagram of the real-time baseline correction time-resolved photoluminescence measurement setup. The use of an additional relatively low frequency (1 kHz) optical chopper and a lock-in amplifier significantly increases the signal-to-noise ratio. A 6.5 μm long-pass filter is inserted in front of the fast HgCdTe detector to filter out unwanted wavelengths and consequently to monitor only LWSL luminescence signals.

of LWSLs using equations (52), (55), (58), and (59) in transient-state with $J = 0$ and an initial condition of $n_{MWSL}(z, 0) = n_0 e^{-\alpha z}$ (where $n_0 = 10^{18}$ cm^{-3} as an initial excited carrier density from a laser energy of 2.3 μJ/pulse). Since equation (55) is a non-homogeneous partial differential equation which does not have a general solution, leading to the used of MATLAB software to obtain a numerical solution. Finite-difference time-domain (FDTD) method is a powerful algorithm to convert the complex derivative operation into simple arithmetic operations, such as addition, subtraction, multiplication, and division. The finite-difference approximation of the first derivative can be expressed as

$$f'(x_i) = \frac{f(x_{i+1}) - f(x_i)}{h}, \tag{81}$$

where $h = x_{i+1} - x_i$ and $\lim_{h \to 0} h = 0$. Similarly, the approximation of the second derivative is

$$f''(x_i) = \frac{f(x_{i+2}) - 2f(x_{i+1}) + f(x_i)}{h^2}. \tag{82}$$

The 3-dimensional image of the numerical solution of $n_{MWSL}(z, t)$ for sample A at 70 K is illustrated in Figure 29, clearly showing the a rapid decay of $n_{MWSL}(z, t)$ on space from sample surface and on time after the laser pulse. To unveil more details regarding the $n_{MWSL}(z, t)$, the cross-sections of the function with respect to time and space are depicted in Figure 30(a) and 30(b), respectively. Recall the equation (52), the carrier injection from MWSLs to LWSLs is dependent on the gradient of carrier concentration $n_{MWSL}(z, t)$ at the

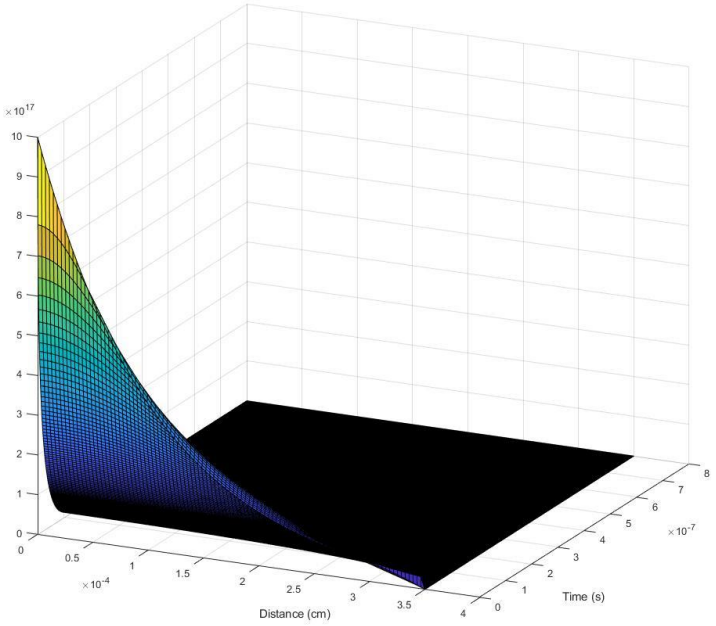

Figure 29. $n_{MWSL}(z,t)$ numerical solution of equation (55) for sample A at 70 K as a function of space and time.

interface. As shown in Figure 30(b), the strength of the slope starts with a higher value and gradually decreases to a small and close to zero value. After obtaining $n_{MWSL}(z,t)$ and its gradient, the numerical solution of $n_{LWSL}(t)$ can then be obtained from equation (52).

(a) (b)

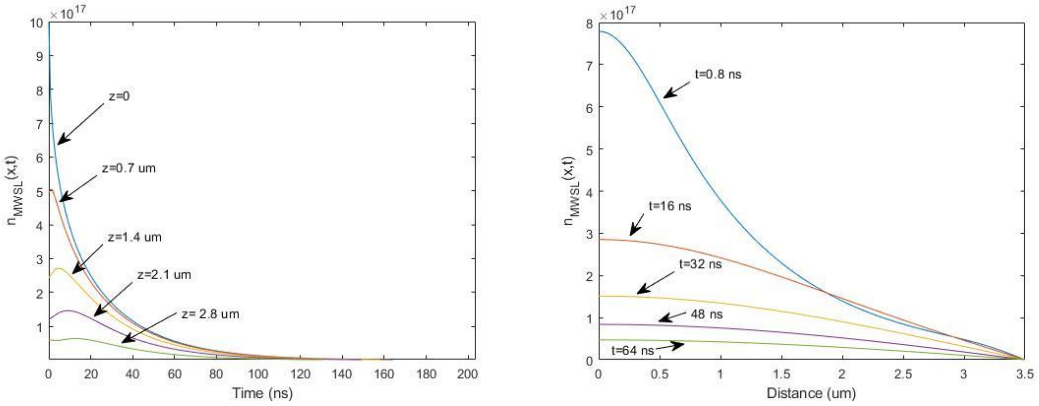

Figure 30. Cross-section view of $n_{MWSL}(z,t)$ in Figure 29 with respect to (a) time and (b) space.

Figure 31 presents the TRPL spectra of LWSLs of sample A and B recorded at 70, 80, and 90 K together with their fitting curves, respectively. The fitting was done by using an absorption coefficient α of 1.0×10^4 cm^{-1} for both samples and lifetimes τ_{MWSL} are the extracted values from Figure 25 and 26, and τ_{LWSL} of 49 ns, 44 ns, and 33 ns for sample A, and τ_{LWSL} of 69 ns, 64 ns, and 56 ns for sample B at 70, 80, and 90 K, respectively. The relatively low intensity of LWSLs PL and the electrical ringing effect (oscillatory tail) increase the difficulty for curve fitting. The electrical ringing effect, which is commonly observed, originates from the impedance mismatch between the coaxial cable and the HgCdTe detector. Under high injection conditions, D_{amb} can be simplified to $D_{amb} = 2D_h$ as described in previous section. From the fitting, vertical hole mobilities of 49.6, 86.9, and 64.4 cm^2/Vs, and 82.7, 65.2, and 41.8 cm^2/Vs were obtained at 70, 80, and 90 K for samples A and B, respectively. These mobility values are comparable to those reported in Refs. [57], [68], [69], [72] (see Table 5). For comparison, these mobility values at 70, 80, and 90 K are marked by "star" and "square" in Figure 27 together with the mobilities extracted by SSPL measurements. For both samples, there is a good agreement between the mobilities extracted from TRPL and SSPL methods. This finding suggests that both methods are able to quantitatively assess the vertical hole mobility in T2SLs.

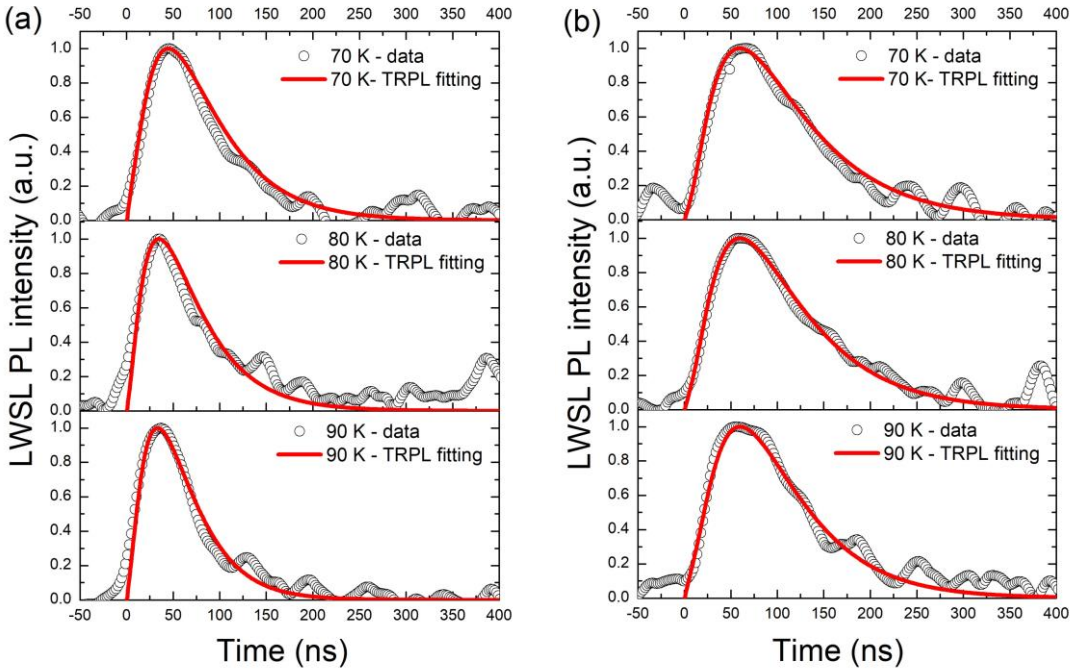

Figure 31. Normalized TRPL spectra and corresponding fitting curves for sample A (a) and B (b) from 70 to 90 K. The vertical hole mobilities extracted from the fitting are 49.6, 86.9, and 64.4 cm^2/Vs for sample A and 82.7, 65.2, and 41.8 cm^2/Vs for sample B at 70, 80, and 90 K, respectively. These data are also indicated in the Figure 27.

Table 5. Comparison of mobilities in $InAs/InAs_{1-x}Sb_x$ T2SLs extracted using different methods. HBT stands for heterojunction bipolar transistors, and Magneto stands for magnetoresistance measurement.

Method	Wavelength (μm)	Vertical hole mobility (cm^2/Vs)	References
SSPL/TRPL	4	40-60 @ 90 K	This work
EBIC	5.5	60 @ 6 K	57
EBIC	5.5	1-30 @ 90 K	68
HBT	12	200 @ 90 K	69
Magneto	5.7	1.6 @ 77K	72

4. InAs/InAsSb TYPE-II SUPERLATTICES nBn, pBn, AND pBp PHOTODETECTOR APPLICATIONS

4.1 Chapter 4 Introduction

As discussed in the chapter 1, the XBn photodetector significantly reduces the dark current by introducing a unipolar barrier layer sandwiched between the absorber and contact layers to block majority carriers, thermally generated or excited by incident photons. It is favorable to operate the IR photodetector in background limited infrared photodetection (BLIP) condition at which the minimum detection is limited by background noise. BLIP temperature is defined as a critical temperature at which the photodetector dark current is equal to the photocurrent induced by background blackbody radiation, given a 2π field of view (FOV), and a background temperature. Typically, the photodetector dark current decreases with temperature since two major components for dark current, G-R and diffusion, are functions of temperature as shown in the following

$$J_{SRH} \approx e\frac{n_i}{\tau_{SRH}}W_{dep} \propto n_i \propto e^{(-E_g/2kT)} \tag{83}$$

$$J_{diff} \approx e\frac{n_i^2}{N_d}\frac{1}{\tau_{diff}}L \propto n_i^2 \propto e^{(-E_g/kT)}, \tag{84}$$

where W_{dep} is the depletion width, τ_{SRH} is the SRH lifetime of minority carriers in the doped region, τ_{diff} is the carrier lifetime, L is the length of neutral region of the device or the diffusion length of minority carrier, whichever is smaller, and N_d is the doping density. At certain threshold temperature, the photodetector noise is equal to the noise generated by 300 K background blackbody radiation, suggesting that with even cooler temperature of

the device, the dark current does not reduce anymore. Here, the threshold temperature is defined as BLIP temperature; therefore, a higher BLIP temperature for an IR photodetector is highly desired because it needs only less and easy cooling systems with lower cost.

To achieve higher BLIP temperature, i.e. high operating temperature (HOT), minimizing the dark current of the photodetector becomes so important that the XBn outstands among all structures. T2SLs not only provide the flexibility of bandgap engineering but also suppress the Auger recombination and tunneling dark current. Combining the benefits from XBn structure and T2SLs, the T2SL XBn IR photodetector is the most prominent device that can possibly beat and replace conventional HgCdTe photodetector [79].

In this chapter, MBE growth and design, and device process of the InAs/InAsSb nBn, pBn, and pBp will be firstly discussed; then the comparison of nBn, pBn, and pBp will be discussed in the last section along with the preliminary test results of these devices.

4.2 MBE Growth and Device Process

All devices have the same InAs/InAsSb T2SL structure for absorber and both top and bottom contacts, consisting of 13.9 nm InAs/4.5 nm $InAs_{0.62}Sb_{0.38}$ totaling a thickness of 2.2 μm, 150 nm, and 280 nm for absorber, top, and bottom contacts, respectively, on (001) GaSb substrates. The growth temperature was 500 ºC for GaSb buffer growth and fixed at 410 ºC for T2SLs growth. The As/In and Sb/In flux ratio were fixed at 1.2 and 0.9, respectively, during the T2SLs growth. The 3.2 nm InAs/2.8 nm $Al_{0.8}Ga_{0.2}As_{0.01}Sb_{0.99}$

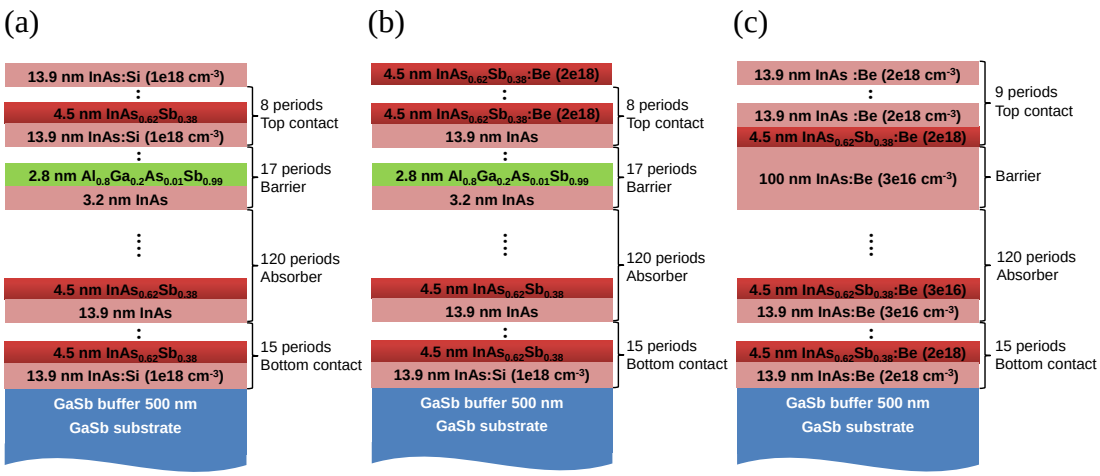

Figure 32. Detailed layer structure of (a) nBn, (b) pBn, and (c) pBp photodetectors.

superlattices unipolar electron barrier layer totaling 100 nm was used for nBn and pBn while 100 nm InAs unipolar hole barrier layer was used for pBp structure. The Sb/III flux ratio was 2 for $Al_{0.8}Ga_{0.2}As_{0.01}Sb_{0.99}$ growth. The As shutter was shut during the $Al_{0.8}Ga_{0.2}As_{0.01}Sb_{0.99}$ growth; therefore, the As in this layer was from the chamber background incorporation. The doping concentration and detailed layer structure are summarized in Figure 32. Since the unintentionally doped InAs/InAsSb T2SLs is n-type, there was no additional doping added into the absorber for nBn and pBn. Si and Be were used as n- and p-type dopant, respectively. The effective bandgap for the absorber was designed at 11 μm and confirmed by measuring PL at low temperature by FTIR. Figure 33 shows the PL spectra of the designed nBn structure (B2666) at 12 K and 77 K, indicating the effective bandgap energy of 119.1 and 113.4 meV at 12 K and 77 K of the absorber, respectively. The effective bandgap energy was obtained by subtracting the PL peak energy with $\frac{1}{2}kT$. The cut-off wavelength of the device is expected to be beyond 11 μm due to the sub-bandgap absorption caused by impurity states.

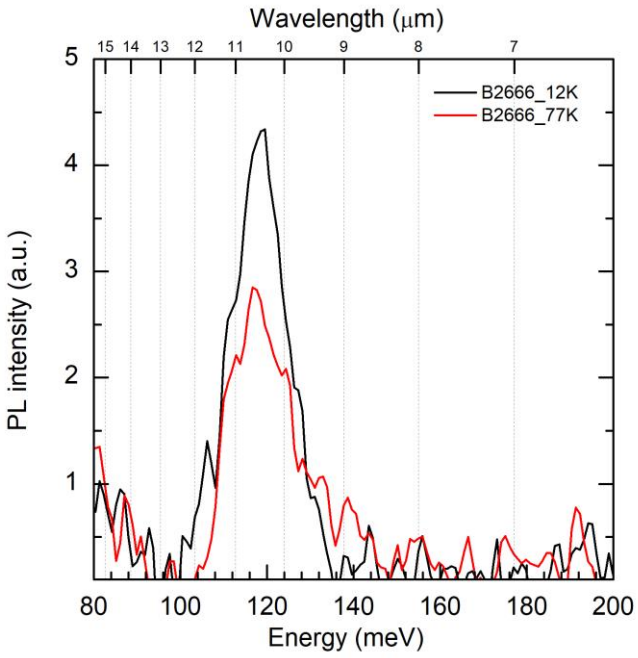

Figure 33. Photoluminescence of InAs/$InAs_{0.62}Sb_{0.38}$ nBn T2SLs at 12 K and 77 K.

After the MBE growth, samples were sent to ASU NanoFab for device process. The photodetector process started with top contact deposition, mesa etch, and bottom contact deposition. Both top and bottom Ohmic contacts were unannealed 50 nm Ti/50 nm Pt/300 nm Au. The top contact possessed different sizes of circular window with the aperture diameter ranging from 100, 150, to 200 μm. The mesa had a size of 410 μm×410 μm square. Wet etching was done with H_3PO_4:H_2O_2:H_2O with a volume ratio of 1:1:10 to etch the InAs/InAsSb T2SL top contact layer and the InAs/AlGaAsSb barrier layer into InAs/InAsSb T2SL absorber; then, citric acid solution (1 g citric acid:1 ml H_2O):H_2O_2:H_2O with a volume ratio of 1:1:10 was used to etch the remaining absorber and stop at middle of the T2SL bottom contact layer. The phosphoric acid etchant is non-selective solution which can etch through InAs/InAsSb T2SLs and Al containing barrier layers with

relatively higher etch rate of 200 nm/min. On the other hand, the citric acid etchant has slower etch rate of 50 nm/min and is selective which cannot etch through the InAs/$Al_{0.8}Ga_{0.2}As_{0.01}Sb_{0.99}$ barrier, but the slower etch rate benefits the side wall smoothness. The masks for these processes are illustrated in Figure 34. Positive photoresist lift-off and etch process were used for these three photomasks; therefore, the blue area in Figure 34(c) is clear; red area in Figure 34(b) is chrome; purple area in Figure 34(c) is clear. Thicker lift-off resist (LOR) was used for bottom contact deposition due to the 2.5 μm mesa topography. No surface passivation and anti-reflection coating were applied. The

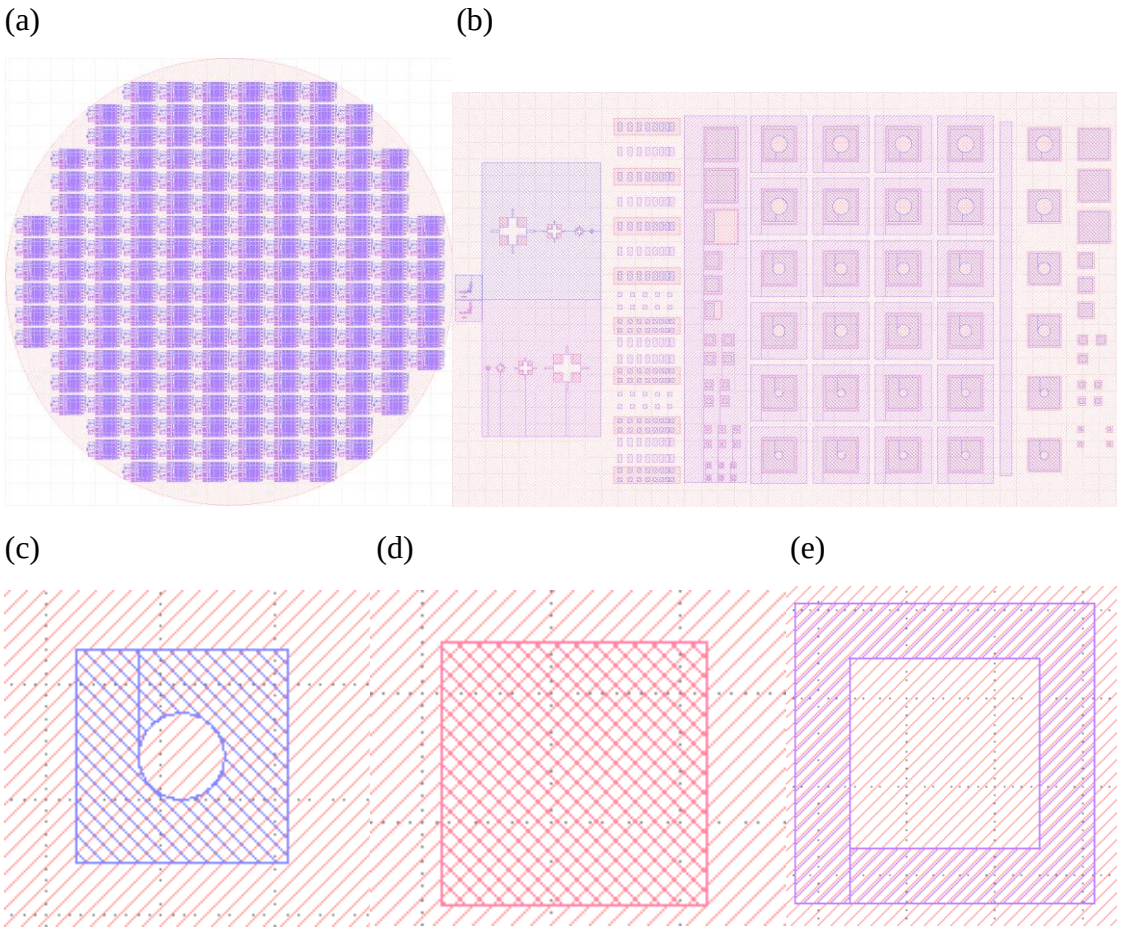

Figure 34. Photomask for photodetector device process. (a) 4" mask; (b) individual die; (c) top contact; (d) mesa; (e) bottom contact.

external bias was applied on the top contact of each mesa while the bottom contact was always grounded.

The scanning electron microscope (SEM) image of the cross-section view of the mesa is shown in Figure 35. The protruding barrier layer is the result from the use of different etchant. Since citric acid is selective etchant while phosphoric acid is not, the top contact and absorber layers were pulled back when the sample was in citric acid solution, leaving Al containing barrier layer sticking out from the sidewall edge.

The complete single element photodetector is shown in Figure 36, including the schematic cross-section view of the device and the photos for different aperture sizes. Then the wafers were diced and each die was wire bonded in a ceramic package.

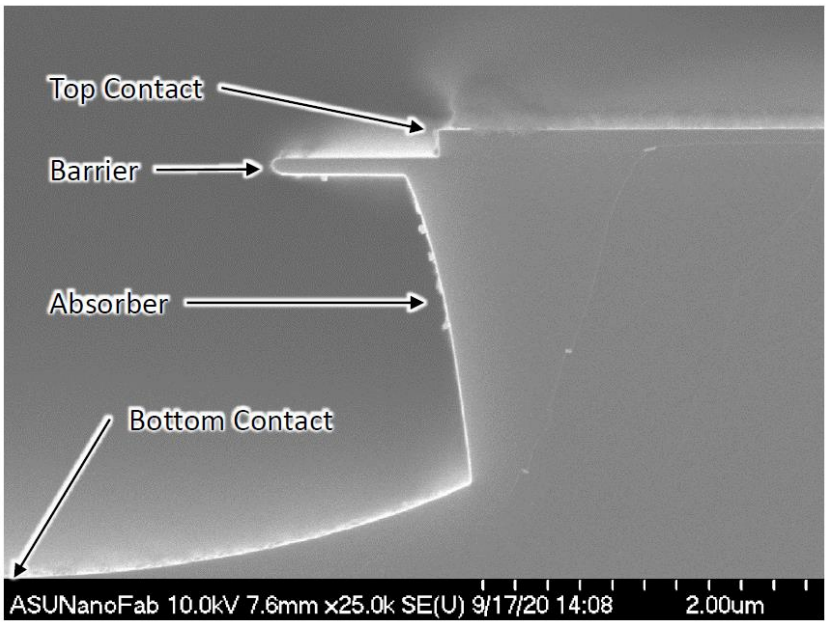

Figure 35. SEM image of cross-section view of the photodetector mesa.

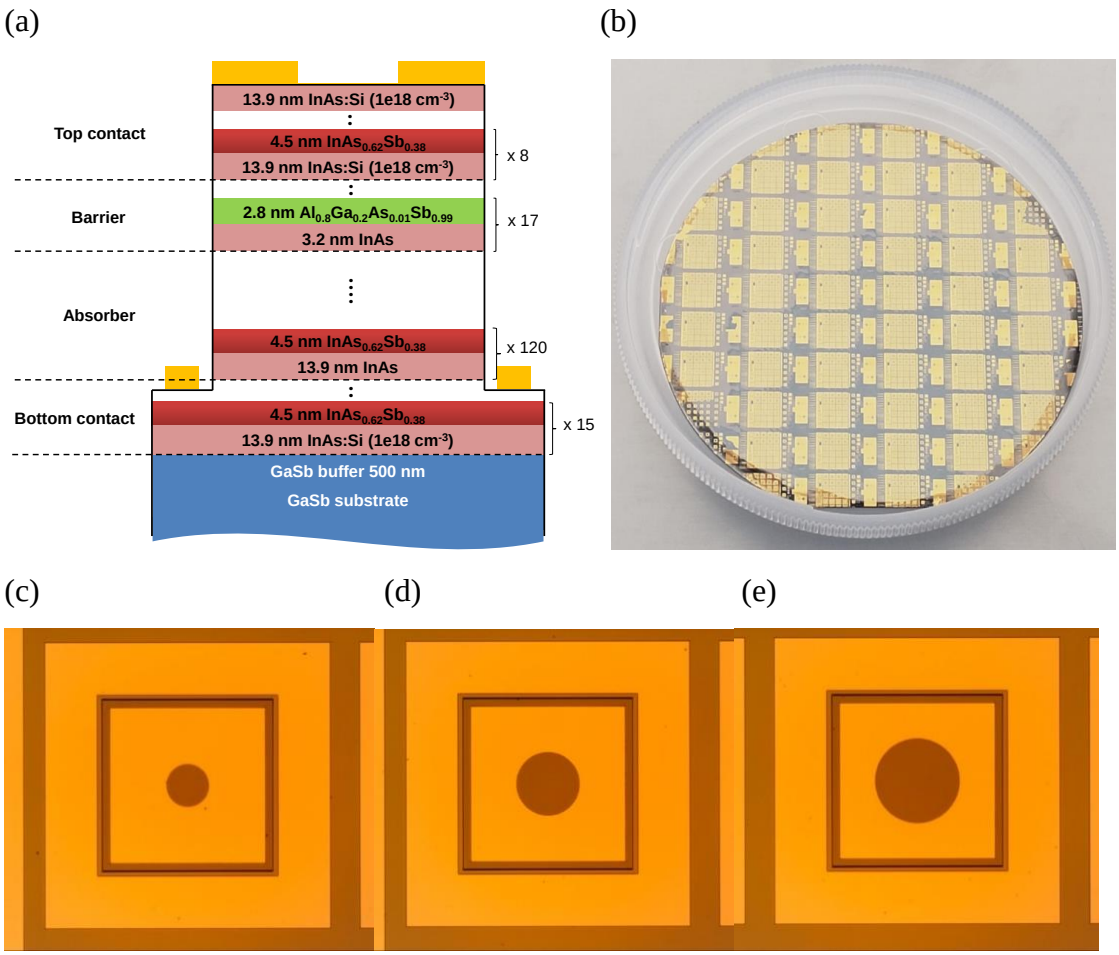

Figure 36. (a) Schematic cross-section of the nBn photodetector mesa. (b) 2” wafer after photodetector process. Microscopic image of single element photodetector with (a) 100 µm, (b) 150 µm, and (c) 200 µm apertures.

(a)

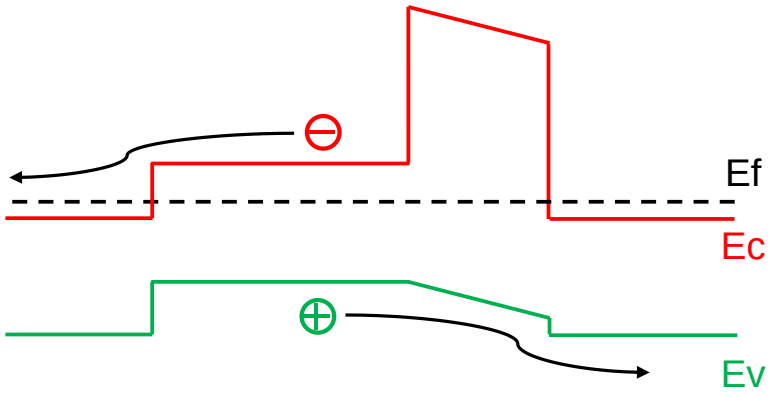

(b)

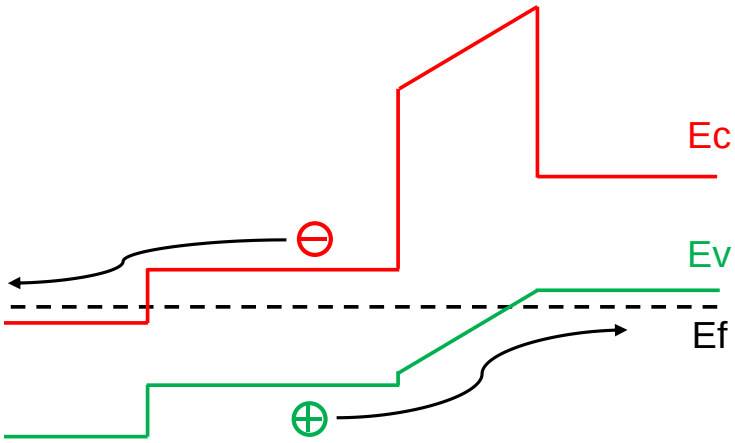

(c)

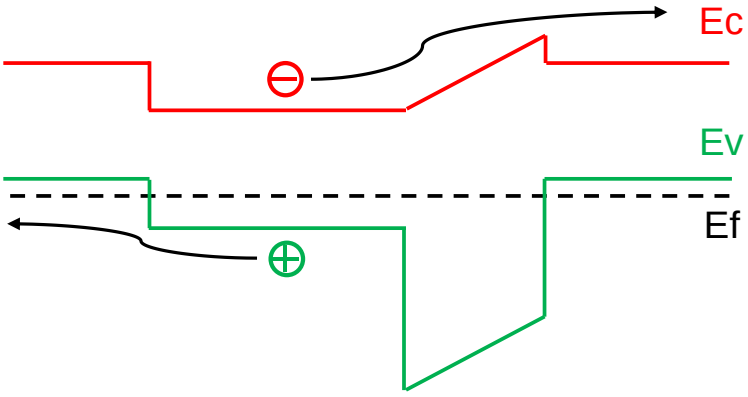

Figure 37. Schematic band diagram of the (a) nBn, (b) pBn, and (c) pBp photodetecros.

4.3 Comparison Between nBn, pBn, and pBp Photodetectors and Measurement Results of nBn Device

Figure 37 depicts the schematic band diagrams of nBn, pBn, and pBp photodetectors under equilibrium without external voltage bias. In these three structures, most of the depletion region and voltage drop occur across the wide bandgap barrier layer; therefore, the G-R dark current originated from SRH recombination centers is greatly reduced. As shown in the Figure 37, a negative voltage bias needs to be applied on the top contact of the nBn device to facilitate the hole transport across the barrier layer, while a positive voltage bias is needed for pBp device to facilitate electron transport. However, for pBn structure, due to the internal electric field, there is no barrier for hole transport. It becomes possible to operate the device at zero bias, further reducing the band-to-band tunneling current and G-R dark current. An important factor that affects the zero bias operation is the zero valence band offset between barrier and absorber layers. Based on previous work [49], the simulation based on Kronig-Penney model shows that the valence minibands of InAs/$InAs_{0.62}Sb_{0.38}$ T2SLs and InAs/$Al_{0.8}Ga_{0.2}As_{0.01}Sb_{0.99}$ T2SLs are aligned while the conduction band barrier height is around 400 meV. The effective bandgap of the barrier is 500 meV which is around 5 times larger than that of the absorber, effectively minimizing G-R dark current and the trap-assisted and band-to-band tunneling current.

The transfer length method (TLM) was adopted to characterize the contact resistivity for both Si-doped n-type and Be-doped p-type InAs/InAsSb T2SL contacts. The TLM pattern consists of rectangular contact pads with 100 μm in width and 50 μm in length with spacings of 10, 20, 30, 40, 50, 60, and 70 μm. Figure 38 shows the current-voltage (I-V)

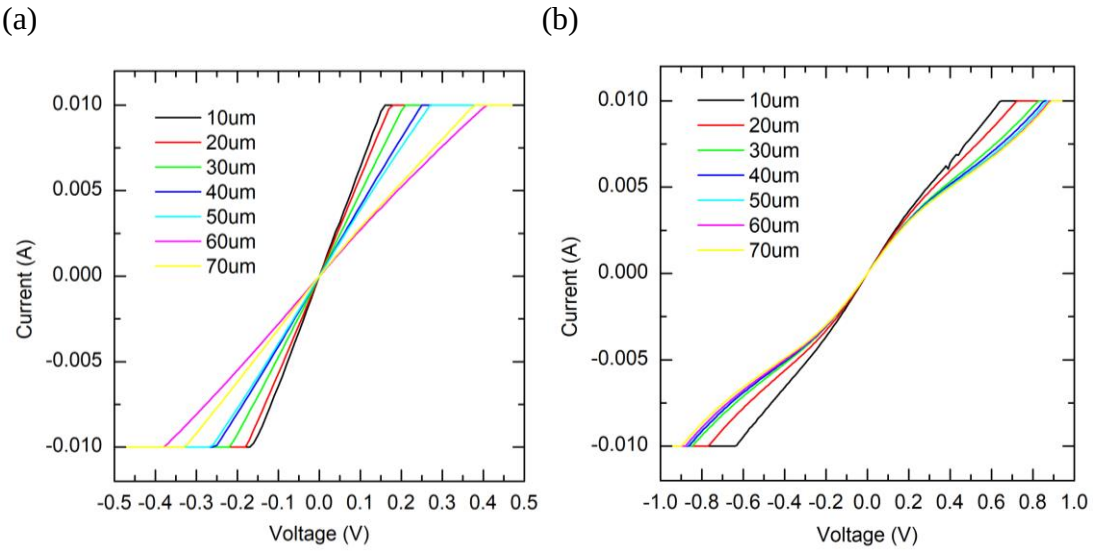

Figure 38. I-V characteristic of the TLM pattern from (a) n- and (b) p-type contacts.

characteristic measured from the top n- and p-type contact TLM pattern of nBn and pBn devices, respectively. Both contacts exhibit Ohmic contact behavior despite there is a small skew in the p-type contact. The total resistance can be calculated from the Figure 38 by fit the linear region with Ohm's law in the voltage range from -0.1 to 0.1 V and -0.2 to 0.2 V for n- and p-type contacts, respectively. Figure 39 shows the measured total resistance dependence on the length in spacing. According to the TLM model, the specific contact resistivity of both n- and p-type contacts can be extracted from the intercept and slope of the curve shown in Figure 39, in which the specific contact resistivities are $8.7 \times 10^{-5}\ \Omega\, cm^2$ and $4.7 \times 10^{-3}\ \Omega\, cm^2$ for n- and p-type InAs/InAsSb T2SLs, respectively.

Figure 40 shows the temperature-dependent dark current density-voltage (J_{dark}-V) characteristic of the nBn devices with a diameter of 200 μm from 77 to 300 K. At the temperature of 77 K and a bias voltage of -0.5 V, the dark current density is

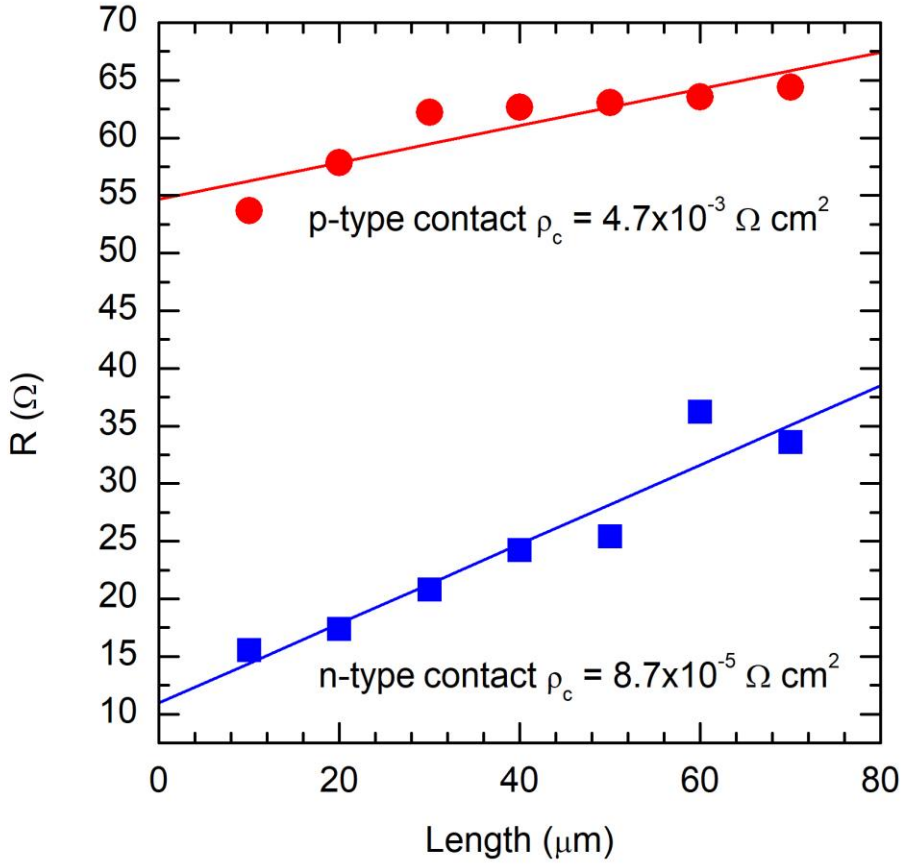

Figure 39. The measured total resistance with respect to the TLM pattern spacing on n- and p-type InAs/InAsSb T2SLs. The linear fit is used to obtain the specific contact resistivity.

$9.5 \times 10^{-4}\ A/cm^2$. This dark current density is, depending on the bias voltage, very close to and possibly superior than that of state-of-the-art LWIR InAs/InAsSb T2SL nBn photodetectors [49], [80], [81]. The temperature-dependent differential resistance-product (R_dA) was obtained from J_{dark}-V curve in Figure 40. R_dA is an important performance parameter for infrared photodetectors, which determines system noise and limits the specific detectivity. Figure 41 shows the temperature-dependent R_dA and reveals a maximum R_dA of 563 Ω-cm^2 under -0.5 V, indicating the optimum operating bias voltage

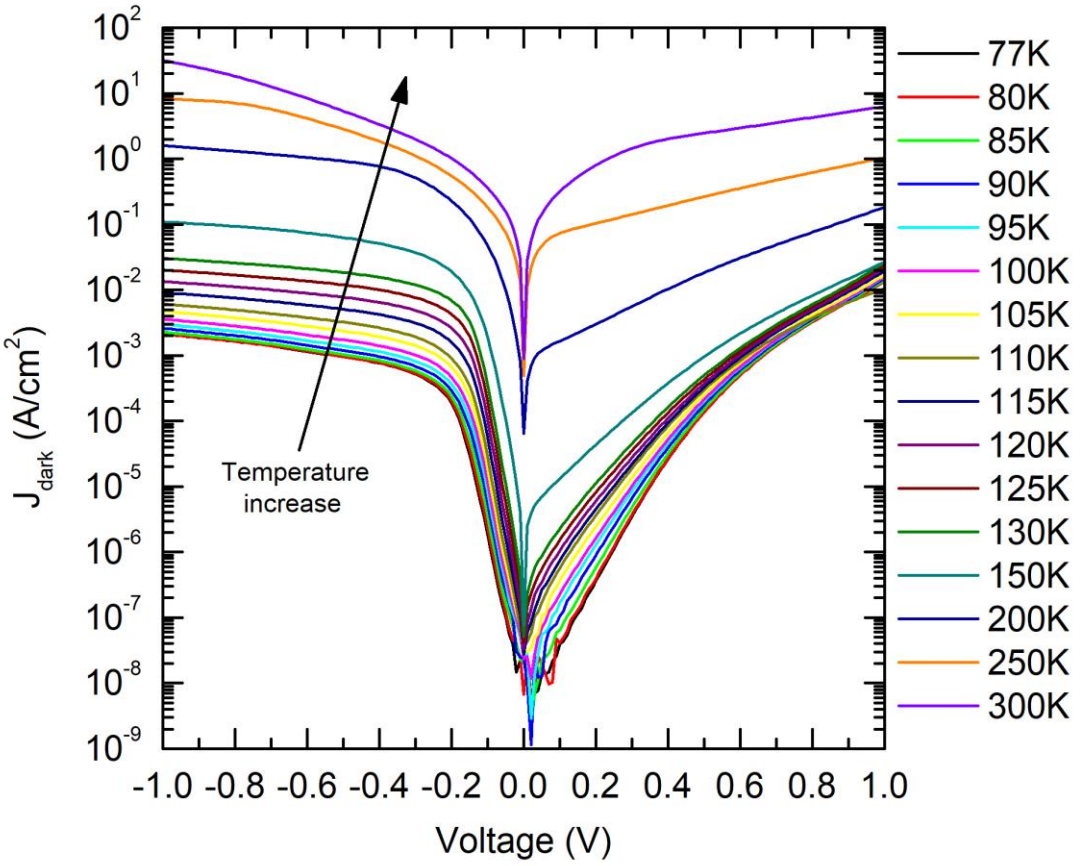

Figure 40. Temperature-dependent dark current density-voltage (J_{dark}-V) of the LWIR InAs/InAsSb nBn photodetector from 77 to 300K.

of -0.5 V. An Arrhenius plot of the dark current density at -0.5 V is shown in Figure 42. From the graph, the slope of the curve represents the activation energy, which can be used to explain which mechanism limits the dark current. Below 90 K, the dark current density stays constant, meaning that it is possibly limited by the background radiation or temperature-insensitive defect-related leakage, for example, surface leakage. From 90 K to 110 K, the dark current density shows an activation energy of 54 meV, suggesting the G-R dark current dominates since as described in equation (83), it is close to half of the

bandgap, which is 113 meV ($\lambda \approx 11$ μm). Above 110 K, the device is diffusion process limited with an activation energy of 106 meV, literally equal to the T2SL bandgap (see equation (84)). The cross point as shown in the Figure 42 indicates that the device can possibly operates between 90 K to 110 K, much improved from temperatures reported previously in the literature [49], [80], [82]–[84].

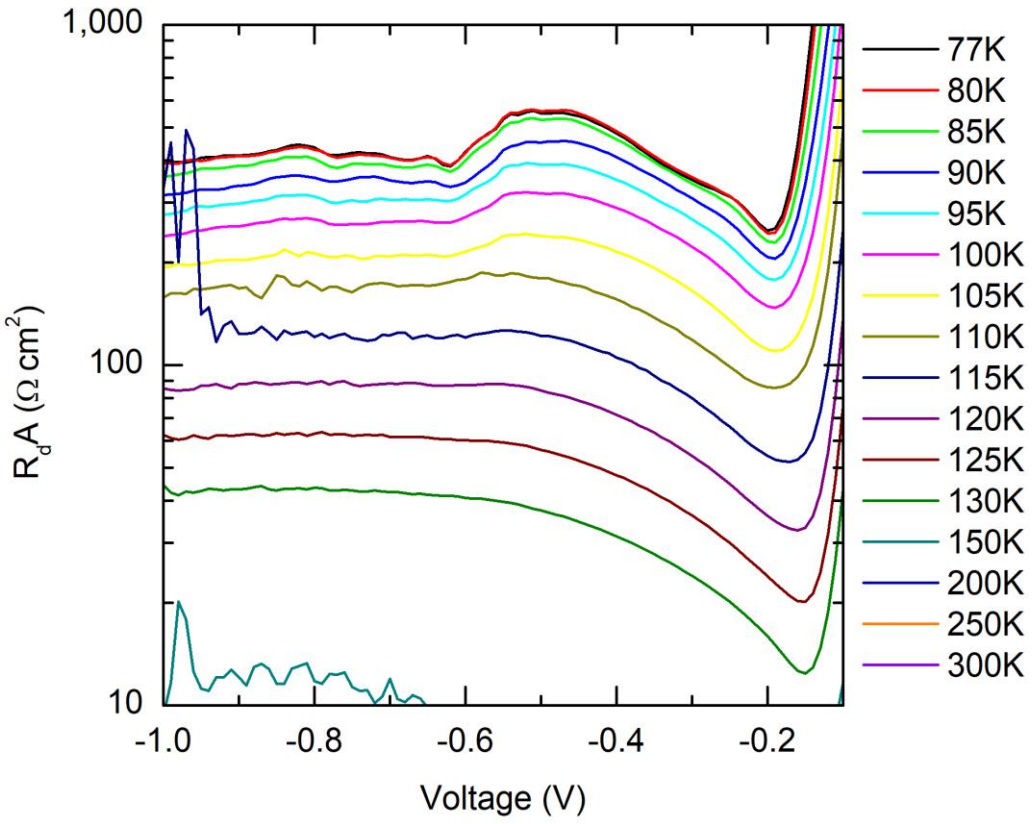

Figure 41. Temperature-dependent differential resistance-area product (R_dA) of InAs/InAsSb T2SL nBn photodetector.

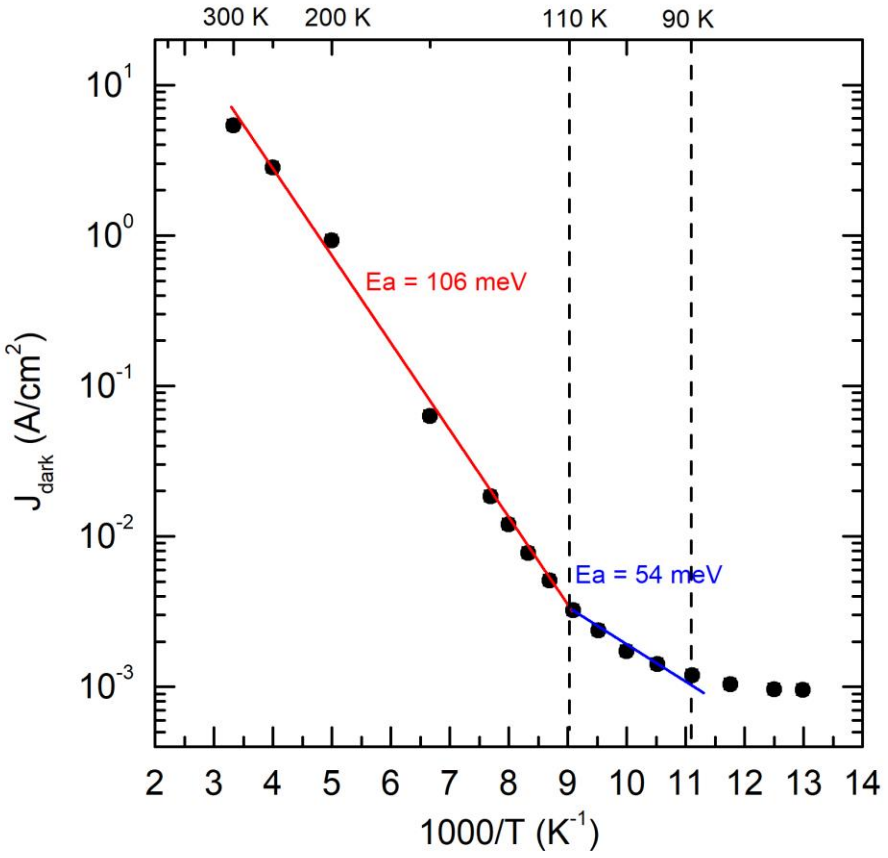

Figure 42. Arrhenius plot of the dark current density of nBn device at -0.5 V. The extracted activation energy for different section is shown.

5. EPITAXIAL LIFT OFF OF II-VI THIN FILMS USING WATER SOLUBLE MgTe

The most preliminary type of epitaxial lift-off (ELO) necessitates the chemical reactions of aggressive acidic etchants which not only harm the surface of a sample but can also harm the environment due to production of hazardous waste. A material which requires a relatively gentle ELO process is Magnesium Telluride (MgTe). MgTe is a material which is extremely hygroscopic and easily hydrolyzed, making simple de-ionized (DI) water the favorable etchant with which to react with the MgTe to lift off the films above. MgTe will decompose into Magnesium hydroxide ($Mg(OH)_2$) and hydrogen telluride (H_2Te) when MgTe reacts with water. H_2Te is a colorless gas and very unstable in atmosphere at room temperature, decomposing immediately into hydrogen and tellurium and producing black particles [85], [86]. The pictures in Figure 43 show observations, which agree with the previously-mentioned reaction, notably that of a test of the pH level of the DI water after MgTe submersion and reaction. The solution becomes alkaline, which is likely a contribution from the hydroxide product. The chemical reaction can be represented by

$$MgTe + 2H_2O \rightarrow Mg(OH)_2 + H_2Te \tag{85}$$

$$H_2Te \rightarrow H_2 + Te\,. \tag{86}$$

A quarter of a 2” CdTe/MgCdTe double-heterostructure (DH) grown atop MgTe which itself was grown on an InSb (001) substrate is submerged into water. Figure 43(a) shows the black particles floating in the water are possibly Te particulates. Figure 43(b) shows the observation of some bubbles, likely hydrogen gas, coming from the sample edges. Evidence of the hydroxide product is seen by a distinct change in pH of the water from a 6

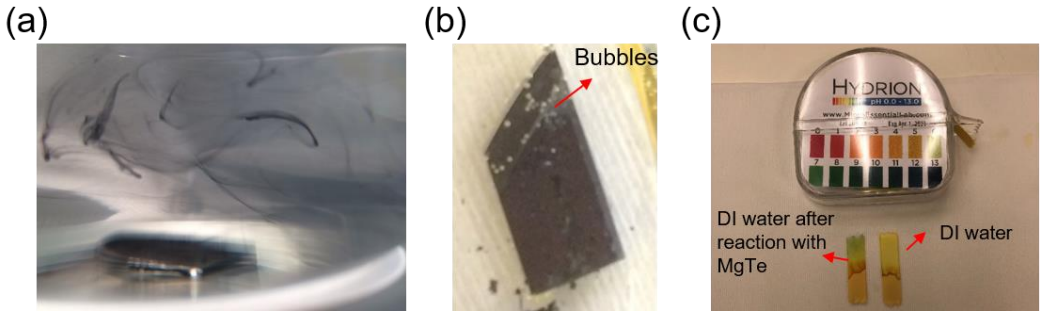

Figure 43. (a) Black particles (tellurium) releasing from the sample when MgTe reacting with water. (b) Hydrogen gas bubbles coming out from sample edges. (c) The water becoming alkaline after reacting with MgTe. The pH level is tested by universal pH indicator.

into a more basic 7 during ELO [Figure 43(c)]. Further work will be needed to confirm the presence of the H_2Te, which likely dissociates into hydrogen gas and tellurium particulates. Because of the hydrolysis property, MgTe can be a sacrificial layer to release the film above it, similar to its III-V counterpart AlAs in hydrofluoric acid (HF). The biggest difference and the most interesting part is only water is used to perform epitaxial lift-off without using any strong acid or base. Water is the least harmful etchant to most of the semiconductor materials, of course except for MgTe and Al containing material.

The schematic diagram of MgTe-based ELO process conducted in this study is shown in Figure 44 [87]. The sample consists of a CdTe/MgCdTe DH on MgTe sacrificial layer grown atop InSb (001) substrate by MBE. Upon removal from ultra-high vacuum after MBE growth, a superstrate, polymer, photoresist or scotch tape, is bonded to the sample surface; then the wafer is submerged in DI water for the hydrolyzing of MgTe which causes the sacrificial layer to be etched away and releases the film on top. Finally, the lifted-off free-standing film can be transferred to a foreign substrate such as reflective back contact,

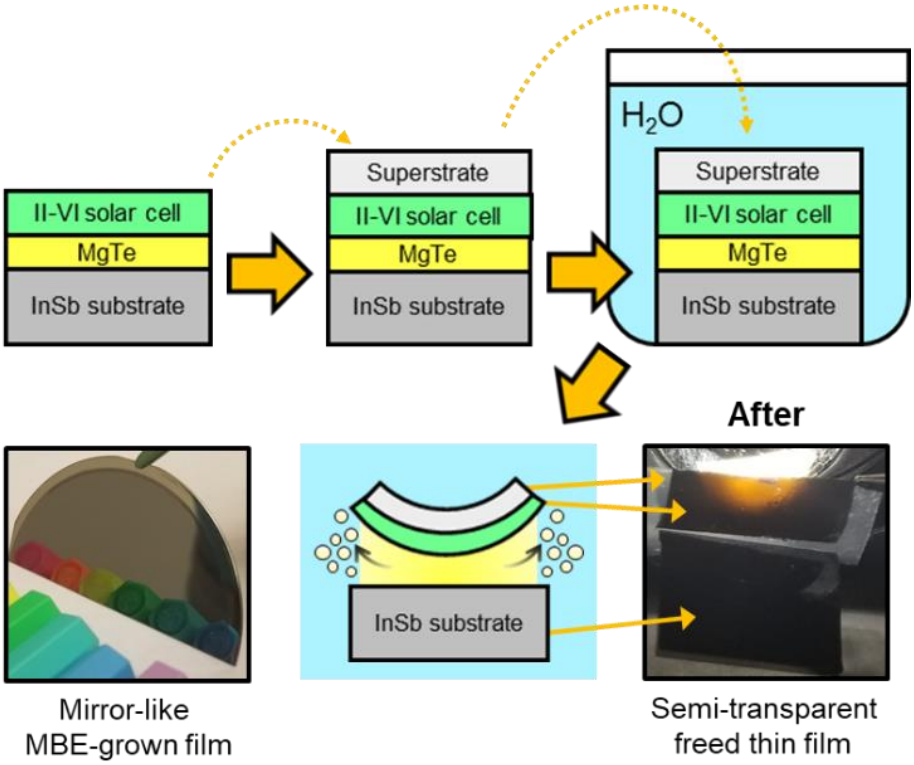

Figure 44. Schematic of II-VI MgTe-based epitaxial lift off process, as well as photographs of the mirror-like MBE-grown sample and a resulting thin film in practice.

Si bottom solar cells, or flexible substrates to make high efficiency solar cells or tandem cell applications. Also, as depicted in Figure 44, the mirror-like surface morphology of as-grown sample and crack-free lifted-off film reveal the potentially low-cost light weight devise for space and terrestrial applications.

5.1 Lift-off Technology Applications and Comparison

The motivation of this work is the integration of different material platforms into a single monolithic system. Several applications can be realized by combining III-V, II-VI, and group-IV materials either *in situ* growth by MBE [88], [89] or *ex situ* integration by

lift-off technique. For example, 20% efficient thin-film CdTe solar cells with a record V_{oc} of 1.1 V are grown on InSb substrates [30], [31]. This substrate will absorb any light escaping from the CdTe absorber. The performance of the solar cell can be improved if the InSb substrate can be removed after MBE growth and replaced by a mirror or reflective back contact. Also, for 1.7-eV MgCdTe solar cells developed for Si-based tandem applications [90], the InSb substrate can be removed and the free-standing MgCdTe thin film can be put on top of Si to make a tandem cell with approaching 30% efficiency. Furthermore, because the substrates have been removed, both CdTe and MgCdTe solar cells are extremely light weight. As such, they can be used for space or drone applications. Additionally, III-V/II-VI integration can make high reflectance DBRs with thinner thicknesses enabled by the large difference in refractive index of III-V and II-V materials [37], [91]. This DBR design can also be lifted-off and used for many IR applications such as resonant-cavity IR LEDs or MWIR vertical-cavity surface-emitting lasers (VCSELs). To make all the aforementioned applications possible, MgTe-based epitaxial lift-off (ELO) is a feasible way to realize a free-standing thin film.

The ELO process for GaAs has been studied since Konagai *et al.* [92] first demonstrated it in 1978 by using hydrofluoric acid (HF) to selectively etch $Al_{0.7}Ga_{0.3}As$ sacrificial layer to release the device from a GaAs substrate. This technique seems promising and the reusable substrate will reduce production costs tremendously. However, the drawbacks of the process include low lateral etching rate and a rough resulting surface. Yablonovitch *et al.* [35] discovered that the critical issue is the reaction product, hydrogen gas, which prevents the etchant from diffusing into the etching zone and forms bubbles

which crack the film. Therefore, this method relies upon the creation of a gap between the lifted-off film and the sacrificial layer in order to allow for the outdiffusion of hydrogen gas from the etching zone. This method is done by applying black wax on top of the sample surface to provide surface tension. This conventional method has been improved by the weight-induced ELO (WI-ELO) process [93], [94] which can obtain a 2" freestanding thin film with a relatively high lateral etching rate. This procedure utilizes a support and a HF-resistant plastic foil with black wax on top of the sample surface. A weight is attached on one side of the foil, which provides external force to lift the film and create a gap to allow for outdiffusion of hydrogen gas when one droplet of 10% HF is applied on the side of the weight. Although the lateral etching rate is higher than that of conventional method, the disadvantages of WI-ELO are the difficulty to control the process and low throughput. The weight needs to be carefully designed for different samples; otherwise too much weight will peel off the thin film instead of lift-off the film and will then result in cracks. Recently, Cheng *et al.* [95] demonstrated surface tension-assisted ELO (STA-ELO) to modify and improve on the conventional method and WI-ELO. The surface tension is provided by photoresist or wax coated on top of the sample which is placed obliquely with an angle of 1° - 20° from the solution surface, and the etchant is added to the level of the etching front. When lift-off is in progress, the etchant can diffuse into the etching zone by capillary force and the film is lifted off and floats on the surface of the solution because of the surface tension provided by photoresist or wax. Therefore, the hydrogen gas can easily diffuse out from the etching front to assure the whole process is chemical reaction limited. Performing ELO in chemical reaction limited conditions is preferred because it can maximize the

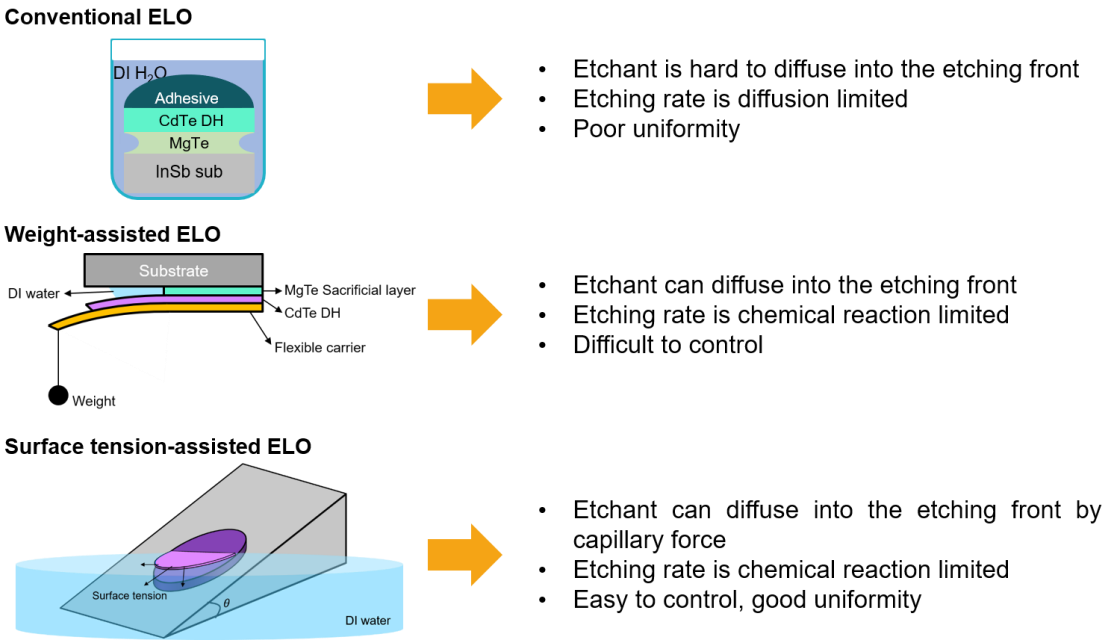

Figure 45. Conventional, weight-assisted, and surface tension-assisted epitaxial lift-off (ELO) technique comparison.

etching rate and throughput [96]. The comparison of these three different ELO methods is illustrated in Figure 45. The ELO process for GaAs/AlGaAs DH has been used for decades in fabrication of thin film devices including solar cells [95], [97]–[99]. This work reports a detailed study of the II-VI ELO process using MgTe with aim to demonstrate its feasibility for enhancing single-junction as well as multijunction thin-film II-VI solar cells along with other thin-film devices.

5.2 Molecular Beam Epitaxy of MgTe Growth

The crystal structure of MgTe has been under debate since Kuhn *et al.* [85]. In his study, MgTe was synthesized in stoichiometric quantities of Mg and Te using a graphite crucible in vacuum wherein a wurtzite structure of MgTe was claimed to be observed.

Table 6. 6.5 Å family material properties. Due to lack of report on MgTe, thermal expansion coefficient of MgTe is missing.

Material	CdTe	MgTe	InSb	HgTe
Crystalline structure	ZB	WZ/ZB	ZB	ZB
Lattice constant at 300 K (Å)	6.482	6.42	6.479	6.453
Thermal expansion coefficient (K^{-1})	4.7×10^{-6}	--	5.0×10^{-6}	4.7×10^{-6}

However, some literature predicts that a zincblende structure is favorable and more stable according to first-principles local-density formalism (LDF) [100] and density-functional theory (DFT) [101]. The wurtzite MgTe has a lattice constant *a* of 4.548 Å and *c* of 7.390 Å [102] while zincblende MgTe has a lattice constant of 6.42 Å closely lattice-matched to InSb (6.479 Å) substrate with less than a 1% mismatch. Table 6 summarizes some material properties of the 6.5 Å family including those of CdTe, MgTe, HgTe, and InSb. They have similar lattice constants and thermal expansion coefficients to each other which makes them suitable for monolithic integration. Furthermore, according to Matthews-Blakeslee's critical thickness model [38] and assuming the crystal structure is zincblende for MgTe and

MgCdTe alloys, the relationship between critical thickness and Mg composition in MgCdTe can be determined, as shown in Figure 46.

To grow the sample, a dual-chamber MBE system is used which contains a III-V and a II-VI chamber connected by an ultra-high vacuum preparation chamber. To begin with, the InSb substrate's oxide is removed in the III-V chamber and after the InSb buffer layer is also grown; the sample is then transferred through the preparation chamber to the II-VI chamber to grow the CdTe buffer, MgTe sacrificial layer, a 500-nm-thick CdTe absorber layer sandwiched by two 30-nm-thick MgCdTe barriers, and a 30-nm-thick CdTe cap layer. Figure 47 illustrates the MBE-grown structure design. The growth temperature for all II-

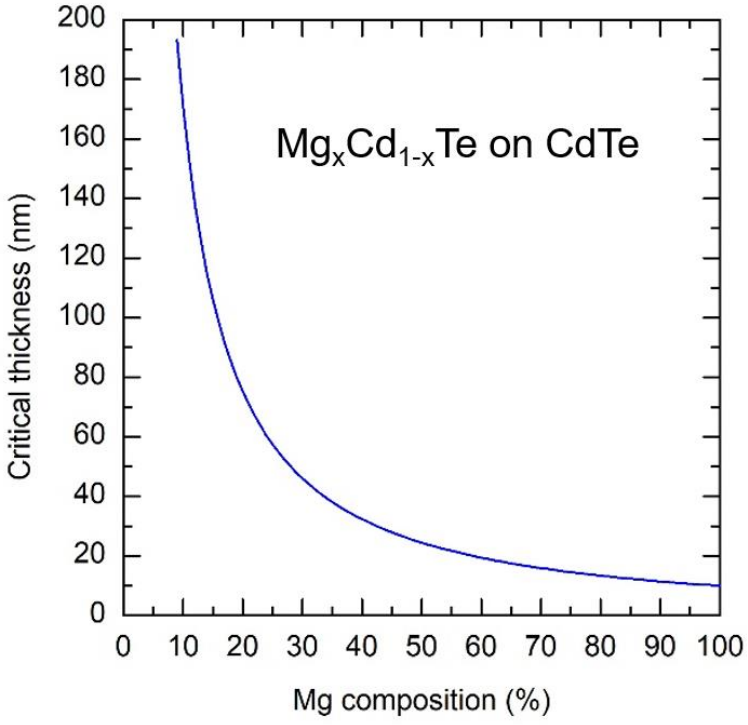

Figure 46. Critical thickness for $Mg_xCd_{1-x}Te$ alloys grown on CdTe. The calculation is based on Matthews-Blakeslee's model [38].

VI material is at 280 ℃ and the growth is under Cd over-pressure with a Cd/Te flux ratio of 1.5 and growth rate of 1.6 Å/s for CdTe. The reflective high energy electron diffraction (RHEED) patterns shown in Figure 48 were taken during the growth of MgTe, which show (2x1) RHEED patterns, the same as those of the CdTe buffer, indicating the MgTe is pseudomorphic and thus has a zincblende structure instead of wurtzite [103]. The bright and streaky patterns also reveal the smooth, 2-dimensional growing MgTe surface and its similarity to that of CdTe. This is the first step in confirming the excellent crystal quality of the resulting thin film sample. A (115) reciprocal space map (RSM) of the sample with

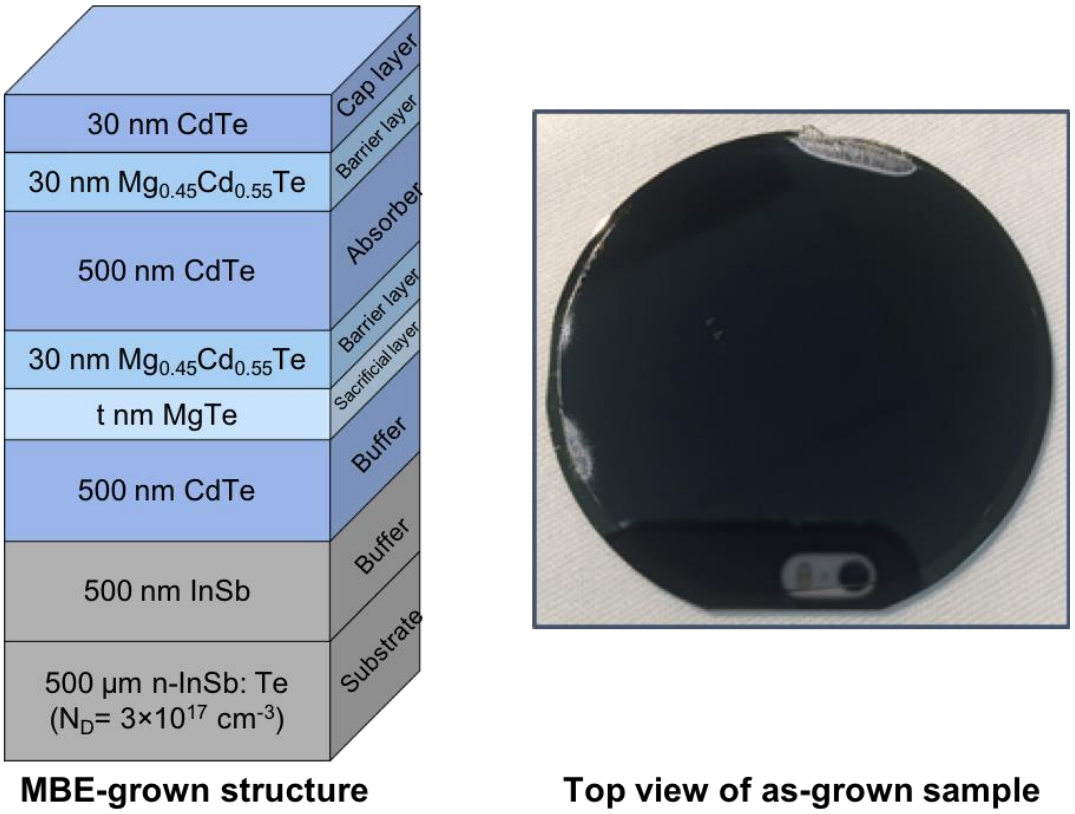

Figure 47. (Left) Layer structure of MBE-grown sample. Several samples with different MgTe thickness (t) are grown as listed in Table III. (Right) Top view of as-grown sample. The grey area at the sample edge is that of slightly melted InSb during InSb substrate oxide removal.

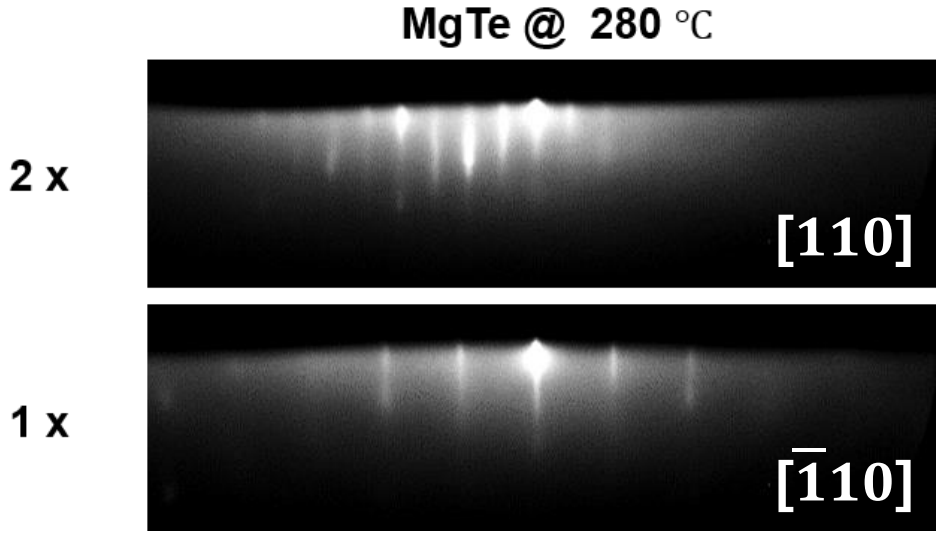

Figure 48. RHEED patterns during the MBE growth of MgTe. The (2x1) patterns are the same as those of CdTe, suggesting MgTe has the zincblende crystal structure.

130-nm-thick MgTe is shown in Figure 49 where it can be observed that even though a thick 130-nm-thick MgTe was grown, the reciprocal lattice points of InSb, CdTe, MgTe, and MgCdTe are aligned on the same Q_{xy}, revealing that all layers have the same in-plane lattice constant and the entire structure is still fully-strained, and maintains good crystallinity and also the zincblende structure for MgTe is further confirmed.

MgTe is extremely hygroscopic, which means that it's very easy for it to absorb moisture from the air and get oxidized immediately. The edge of the sample is the only place that has direct contact with air because of the stack-up of the CdTe DH on top of the MgTe surface. Edge oxidation and its MgTe thickness dependence are crucial factors in the ELO process. Once the edge is oxidized, it will prevent the etchant from diffusing into the etching front and therefore the ELO process stops. Several samples with different MgTe thickness were grown ranging from 20 to 130 nm as listed in Table 7. The samples display

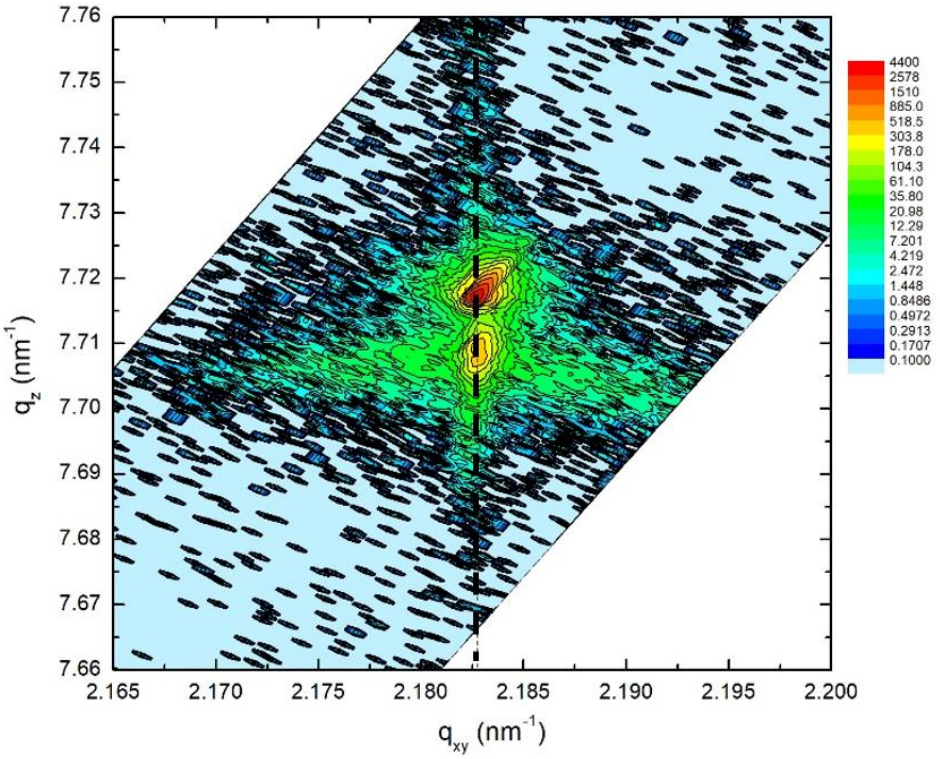

Figure 49. (115) RSM of CdTe DH with 130-nm-thick MgTe MBE-grown sample. The black dash line indicates in-plane reciprocal lattice constant of InSb substrate.

different stabilities in atmosphere. Figure 50 shows a side-by-side, top-down 5× magnified microscopic image of sample B (20 nm MgTe) and C (130 nm MgTe) 30 minutes after removal from ultra-high vacuum. Sample B has a smooth as-grown surface even under 50 × magnification, shown in the bottom right image of Figure 50. In contrast, the edges of

Table 7. A table of the four samples grown in this study which feature different thicknesses as well as compositions of the sacrificial layer.

Sample	MgTe layer thickness	Cd alloyed into MgTe
	t nm	%
A	10	Trace
B	20	Trace
C	130	Trace
D	130	22

sample C roughen as a result of the oxidation of the MgTe layer to a lateral depth of ~1 mm from the edges. On a heating stage in atmosphere set to 250 ºC, a 1-inch wide piece of sample C fully oxidizes from its edges to center within minutes. Sample B shows no signs of oxidation under the same high-temperature conditions. These results suggest that oxidization processes at MgTe film edges are greatly dependent on MgTe thickness and can be exacerbated by higher sample temperatures. Sample D does not exhibit any oxidation but as discussed below, turns out to be ineffective as a water-soluble sacrificial layer.

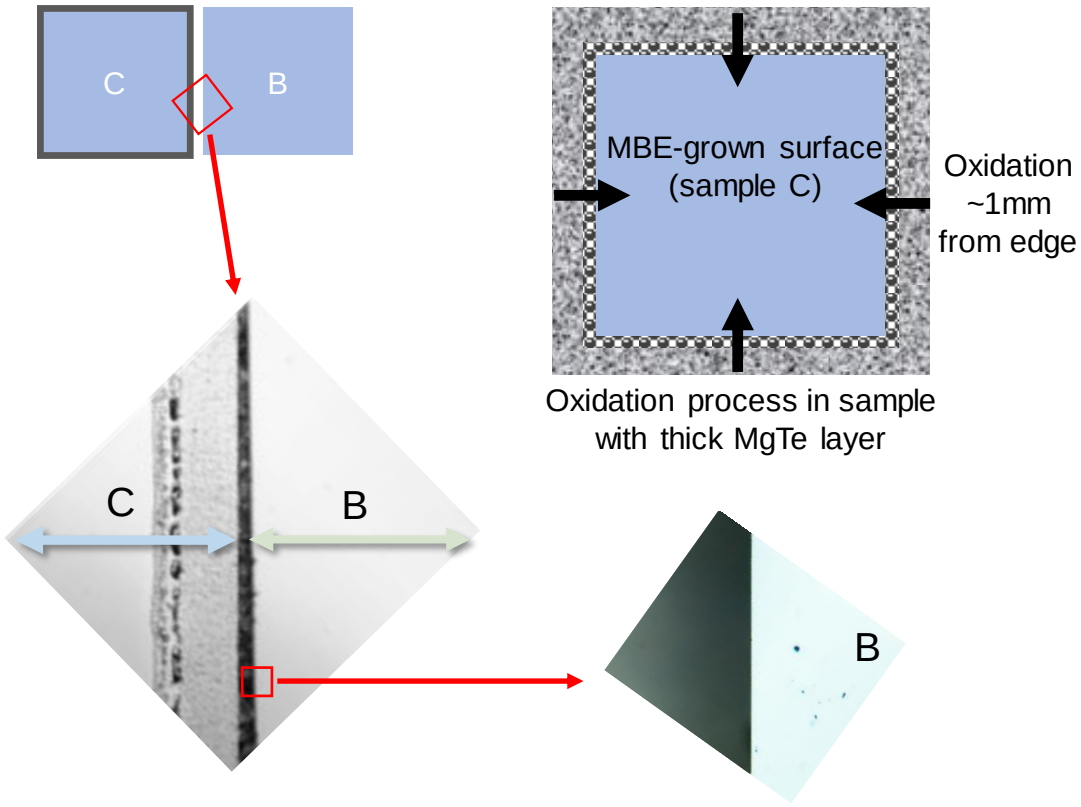

Figure 50. Edge oxidation of CdTe/MgCdTe DH samples with 130 and 20-nm-thick MgTe. Sample C (130 nm MgTe) has been oxidized 1 mm from the edge while sample B (20 nm MgTe) still has abrupt edges.

5.3 Structural and Optical Properties of Pre- and Post-lifted-off Film

The very first ELO process we have tried is using Scotch tape. The as-grown sample C is covered by Scotch tape before submerging into DI water. After a couple minutes to hours, depending on the thickness of the MgTe, the CdTe/MgCdTe DH film is released while attached to the tape. The pictures shown in Figure 44 illustrate the process and a potential application to flexible or wearable devices since the CdTe film is bendable. The structural quality of the free-standing film is characterized by a HR XRD $\omega - 2\theta$ scan along the (004) plane. Figure 51 shows the XRD of the sample before the ELO process and the free-standing film on tape post-ELO. The diffraction peaks of the sample before the ELO process are well defined and they fit properly with the simulation. The peak of the InSb buffer is off the substrate peak a little bit due to a small amount of unintentional As

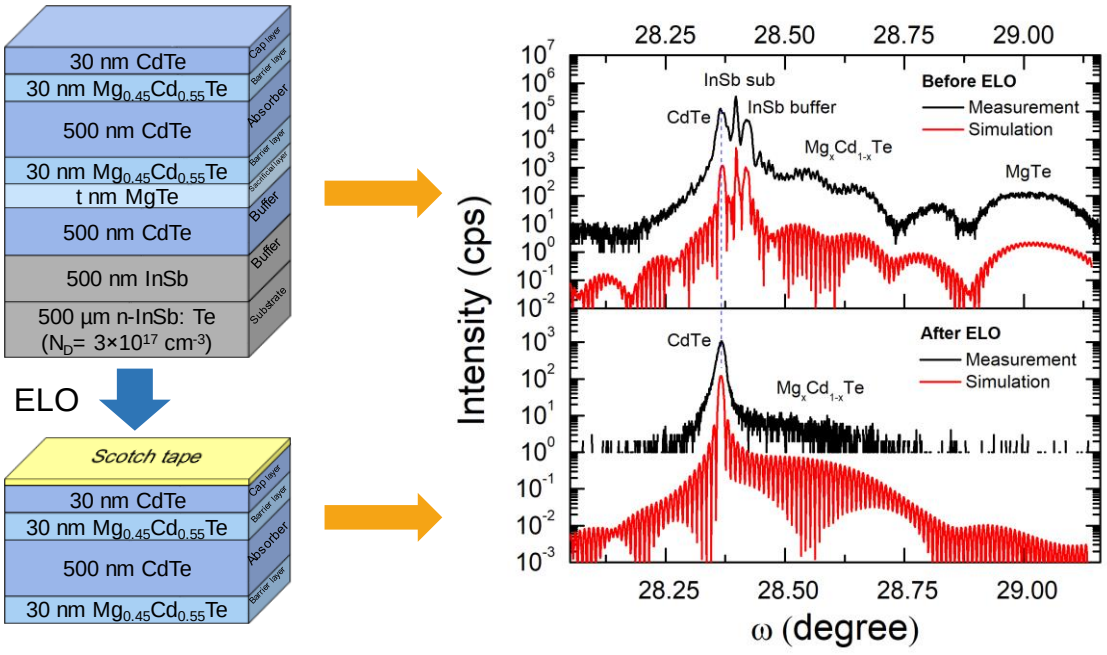

Figure 51. $\omega - 2\theta$ XRD of sample C before (top) and after (bottom) ELO process. The disappearance of InSb and MgTe peaks indicates successful removal of substrate and sacrificial layer.

incorporation from the background during the MBE growth. After the ELO process, the free-standing film with tape on top is mounted on a Si carrier wafer to perform the measurement. The XRD results show the absence of InSb and MgTe peaks; only CdTe and $Mg_{0.45}Cd_{0.55}Te$ peaks are left, which is the evidence of successful ELO. It should be noted that the FWHM of the CdTe absorber peak broadens between pre- to post-ELO, which is likely due to a slight bending of the flexible tape superstrate.

After ELO, the bottom $Mg_{0.45}Cd_{0.55}Te$ surface is exposed to the air. The surface morphology of this layer is characterized by atomic-force microscopy (AFM), as shown in Figure 52, revealing the smooth lifted-off surface with root-mean-square (RMS) roughness of 6.69 Å, indicating the surface is intact and its reaction rate with DI water is extremely low.

The optical performance of the pre-ELO films is measured by room-temperature photoluminescence (PL) spectroscopy. Figure 53 shows the PL spectra of samples B and C excited with a 532-nm continuous wave laser light. The peak in the spectra corresponds

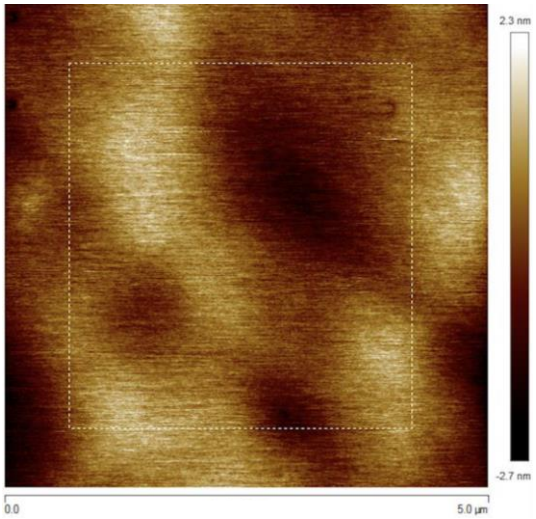

Figure 52. AFM image of $Mg_{0.45}Cd_{0.55}Te$ surface morphology after ELO in 5 µm × 5 µm range with RMS roughness of 6.69 Å.

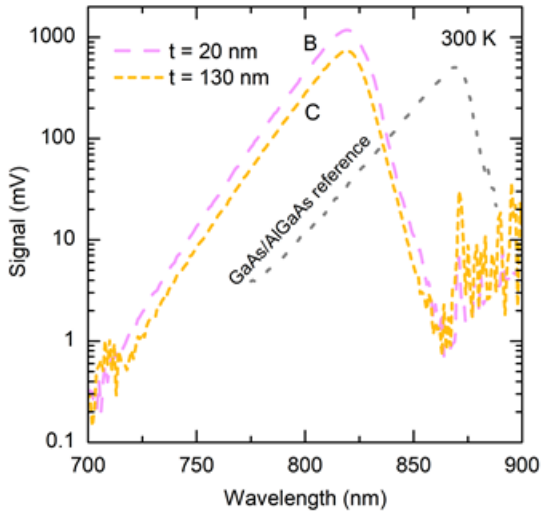

Figure 53. Room-temperature photoluminescence (PL) showing a trend of higher PL intensity with a thinner MgTe layer.

to the bandgap of the CdTe absorber. Both samples in this study have peak intensities higher than the GaAs/AlGaAs DH reference sample, indicating their high optical quality. The PL peak intensity of sample B is approximately twice as high as that of sample C. This weaker PL intensity from sample C likely stems from the thick 130 nm MgTe layer. Since the conservative Matthews-Blakeslee critical thickness of the MgTe/CdTe material system is 10 nm, it is understandable that sample C, whose MgTe thickness is an order of magnitude higher than theoretical critical thickness, would possess a higher density of misfit dislocations and subsequently a higher nonradiative recombination rate.

Figure 54 depicts the PL spectra of a 2.5 mm × 5 mm piece of sample B both as-grown and as a CdTe/MgCdTe DH thin film after ELO from its InSb substrate. Strong PL peak intensity is seen in the free-standing film. This shows that the optical quality of the DH absorber survives after ELO. Shown in Figure 54, the lack of an absorptive substrate

enables the film to act as an efficient waveguide and causes the edges of the thin film to luminesce at an intensity up to $3\times$ higher than that of the as-grown sample. This phenomenon would not be possible without the survival of excellent optical quality in the free-standing DH absorber and the lack of an absorptive substrate enabling enhanced photon-recycling in the film.

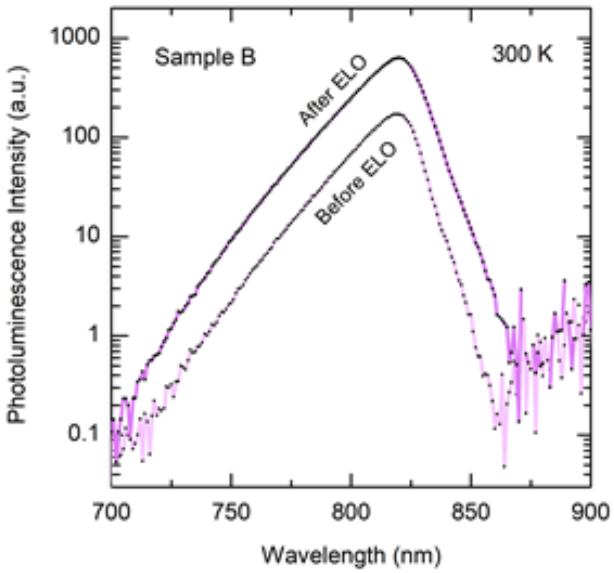

Figure 54. As-grown and after lift-off sample B room-temperature photoluminescence (PL). Higher PL intensity is observed after ELO.

6. CONCLUSION AND OUTLOOK

In summary, the vertical hole transport in InAs/$InAs_{1-x}Sb_x$ mid-infrared T2SLs has been investigated by using SSPL and TRPL spectroscopies. The mobilities extracted from both samples A and B show comparable values, which clearly showcase the decent run-to-run reproducibility in the T2SL growth by MBE. The strong carrier localization observed at low temperatures impedes hole transport in the MWSL region, resulting in a hole mobility of ~0.2 cm^2/Vs at 12 K. The rapid increase of hole mobility with temperature reveals the thermally activated nature of the hole transport in the MWSL region. Above 60 K, the mobility saturates at ~50 cm^2/Vs. This saturation is attributed to the interface scattering from alternate InAs and $InAs_{1-x}Sb_x$ layers. The results show that both SSPL and TRPL methods are straightforward in terms of the experimental setup and data interpretation. The comparison of the mobilities extracted from SSPL and TRPL methods provides a useful means to verify the accuracy of the obtained mobility.

The method to extract MWIR InAs/$InAs_{1-x}Sb_x$ T2SLs vertical hole mobility can also extend to LWIR range. Several samples have been grown with the design as shown in Figure 55(a). The structure for the study of LWIR T2SLs vertical mobility is comprised of a 2.82 nm InAs/9.12 nm $InAs_{0.61}Sb_{0.39}$ T2SL transport region with PL wavelength of 8 μm grown atop a probe region consisting of a 5.78 nm InAs/18.72 nm $InAs_{0.64}Sb_{0.36}$ T2SLs with PL wavelength of 12 μm. Figure 55(b) shows the corresponding XRD pattern which also indicates the well-aligned zeroth-order satellite peaks for both T2SLs with the substrate peak. The temperature-dependent SSPL spectra of the sample as illustrated in Figure 56, however, only show the 8 μm PL peak without any observation of 12 μm PL

peak. Due to the weak electron-hole wave-function overlap of the T2SLs with 12 µm wavelength, the PL intensity from the layer is expected to be low. Also, the PL peak energy of the transport region decreases monotonically as temperature increases, evidencing the carrier localization is not significant at low temperature in this sample because of the thicker period thickness.

The future work for extending the method to be applied on LWIR range is to design a new structure with much higher Sb % in the probe region. For the current design the probe region has similar Sb % to that of transport region, leading to poor hole confinement and potentially inhibiting the carrier recombination in the probe region with 12 µm wavelength. Increasing the Sb % will essentially lift up the hole miniband and provide better hole confinement as a results of large valence band bowing in the $InAs_{1-x}Sb_x$ alloy. Further simulations and experiments can be carried out to complete the work of the study.

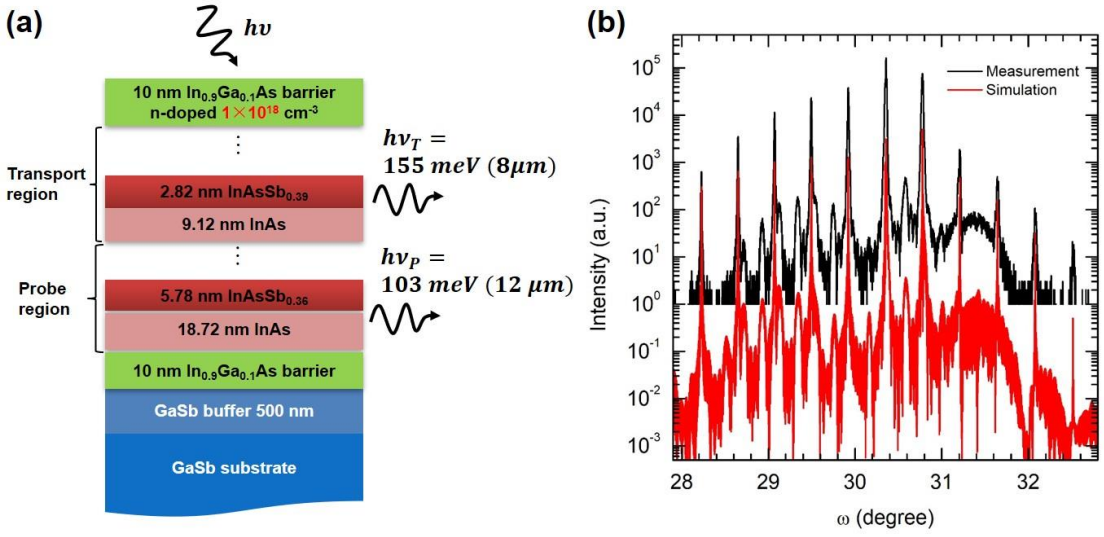

Figure 55. (a) Sample structure of LWIR T2SLs vertical carrier transport study. (b) (004) $\omega - 2\theta$ XRD pattern of the sample described in (a).

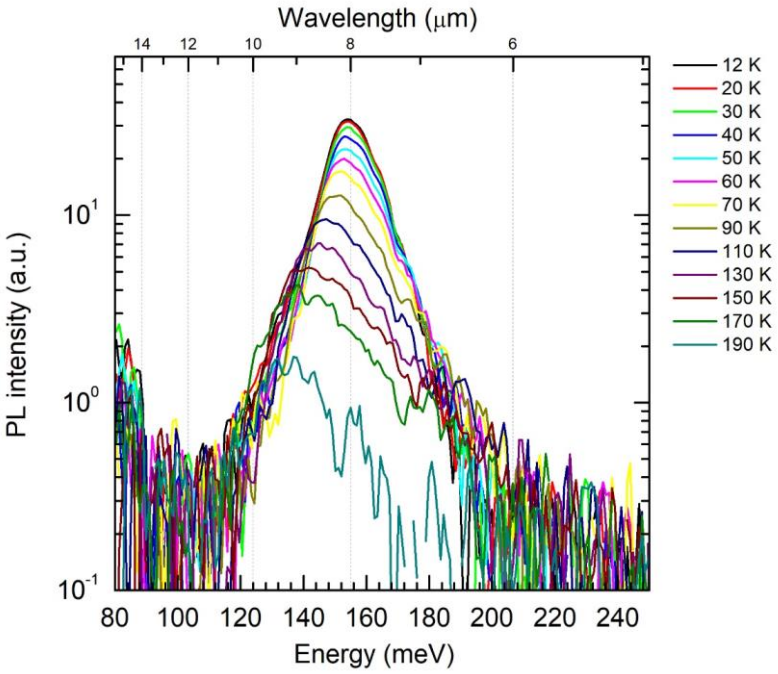

Figure 56. Temperature-dependent SSPL spectra of the sample illustrated in Figure 55(a). The peak around 15 μm is an artifact from the measurement system.

Besides, the design, growth, and device process of nBn, pBn, and pBp photodetectors are well discussed with some preliminary results. The future work of the photodetector project is to measure and analyze temperature-dependent and bias-dependent spectral responsivity and detectivity, D*, which are the two important figure-of-merits determining the cut-off wavelength and the performance over a wide spectral range. High-operating-temperature (HOT) LWIR InAs/InAsSb T2SL barrier detector is anticipated. The future work of this project can also be focusing on: (1) optimized the doping in the barrier layer, and (2) study the valence band offset between barrier and T2SL absorber. The need for the first work is because the G-R dark current still shows in the Arrhenius plot of the dark current density with an activation energy of 54 meV, which is half of the T2SL bandgap, indicating the depletion region has reached the T2SL absorber from the barrier layer.

Ideally, the G-R dark current from the absorber layer can be totally suppressed since almost all the voltage drop and depletion region should occur only in the wide-bandgap barrier layer. For the second work, since the optimum operating bias of the nBn device presented in this report is -0.5 V, which is comparatively higher than those of published work, -0.08 V [81]. The accurate simulation is needed in order to assure the valence band offset between T2SL absorber and barrier is perfectly flat, which can greatly reduce the operating bias voltage. The benefits of smaller operating bias are lower G-R dark current, lower tunneling current and lower power consumption.

This dissertation also demonstrates an ELO method to obtain free-standing single-crystal CdTe/MgCdTe double heterostructures from sample grown on lattice-matched InSb substrates. This method uses water-soluble MgTe, and results from this study show that MgTe film thickness can optimize the ELO process, allowing for the development of flexible, free-standing II-VI films with high structural and optical quality that exhibit stability in atmosphere and smooth, fast ELO. This ELO process can be utilized in the fabrication of II-VI solar cells in order to enhance photon-recycling and opportunities for integration in tandem devices. Subsequent studies will focus on improving widescale film uniformity and will aim to demonstrate a solar cell featuring a thin-film II-VI absorber. The schematic process flow for fabricating CdTe thin film on metal back contact is shown in Figure 57. Theoretically, since the photon recycling effect increases due to metal back contact and therefore the absorber thickness can be reduced which leads to less SRH non-

radiative recombination, the power conversion efficiency and open circuit voltage can beat the record published in 2016 [30].

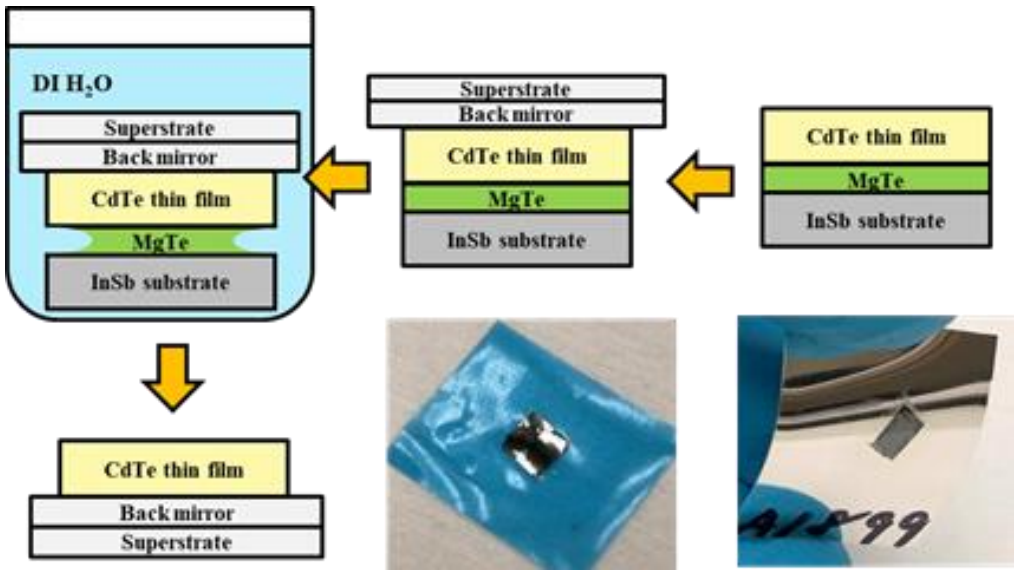

Figure 57. Process flow for fabricating free-standing CdTe thin-film solar cell with metal back contact.

REFERENCES

[1] Z. I. Alferov, “Nobel lecture: The double heterostructure concept and its applications in physics, electronics, and technology,” *Rev. Mod. Phys.*, vol. 73, no. 3, pp. 767–782, 2001.

[2] L. Esaki and R. Tsu, “Superlattice and Negative Differential Conductivity in Semiconductors,” *IBM J. Res. Dev.*, vol. 14, no. 1, pp. 61–65, 1970.

[3] H. Schneider and H. C. Liu, *Quantum Well Infrared Photodetectors*. 2007.

[4] A. Y. Cho and J. R. Arthur, “Molecular beam epitaxy,” *Prog. Solid-State Chem.*, vol. 10, no. 3, pp. 157–191, 1975.

[5] Q. Liu, X. Zhang, L. B. Abdalla, and A. Zunger, “Transforming Common III-V and II-VI Semiconductor Compounds into Topological Heterostructures: The Case of CdTe/InSb Superlattices,” *Adv. Funct. Mater.*, vol. 26, no. 19, pp. 3259–3267, 2016.

[6] A. Rogalski and K. Chrzanowski, “Infrared devices and techniques (revision),” *Metrol. Meas. Syst.*, vol. XXI, no. 4, pp. 565–618, 2014.

[7] A. Rogalski, “Next decade in infrared detectors,” in *Proc. SPIE 10433, Electro-Optical and Infrared Systems: Technology and Applications XIV*, 2017, no. 104330L.

[8] W. D. Lawson, S. Nielsen, E. H. Putley, and A. S. Young, “Preparation and properties of HgTe and mixed crystals of HgTe-CdTe,” *J. Phys. Chem. Solids*, vol. 9, no. 3–4, pp. 325–329, 1959.

[9] D. Bagot, S. Rolland, R. Granger, and R. Triboulet, “Linear thermal expansion coefficient in $Hg_{1-x}Cd_xTe$ and $Hg_{1-x}Zn_xTe$,” *J. Cryst. Growth*, vol. 117, pp. 189–192, 1992.

[10] P. Norton, “HgCdTe infrared detectors,” *Opto-electronics Rev.*, vol. 10, no. 3, pp. 159–174, 2002.

[11] D. R. Rhiger, “Performance comparison of long-wavelength infrared type II superlattice devices with HgCdTe,” *J. Electron. Mater.*, vol. 40, no. 8, pp. 1815–1822, 2011.

[12] G. A. Sai-Halasz, R. Tsu, and L. Esaki, “A new semiconductor superlattice,” *Appl. Phys. Lett.*, vol. 30, no. 12, pp. 651–653, 1977.

[13] H. Sakaki, L. L. Chang, G. A. Sai-Halasz, C. A. Chang, and L. Esaki, “Two-dimensional electronic structure in InAs-GaSb superlattices,” *Solid State Commun.*, vol. 26, pp. 589–592, 1978.

[14] D. L. Smith and C. Mailhiot, “Proposal for strained type II superlattice infrared detectors,” *J. Appl. Phys.*, vol. 62, no. 6, pp. 2545–2548, 1987.

[15] E. H. Steenbergen *et al.*, “Significantly improved minority carrier lifetime observed in a long-wavelength infrared III-V type-II superlattice comprised of InAs/InAsSb,” *Appl. Phys. Lett.*, vol. 99, p. 251110, 2011.

[16] D. Donetsky, S. P. Svensson, L. E. Vorobjev, and G. Belenky, “Carrier lifetime measurements in short-period InAs/GaSb strained-layer superlattice structures,” *Appl. Phys. Lett.*, vol. 95, no. 21, pp. 14–17, 2009.

[17] J. B. Rodriguez, P. Christol, L. Cerutti, F. Chevrier, and A. Joullié, “MBE growth and characterization of type-II InAs/GaSb superlattices for mid-infrared detection,” *J. Cryst. Growth*, vol. 274, no. 1–2, pp. 6–13, 2005.

[18] P. J. Carrington, Q. Zhuang, M. Yin, and A. Krier, “Temperature dependence of mid-infrared electroluminescence in type II InAsSb/InAs multi-quantum well light-emitting diodes,” *Semicond. Sci. Technol.*, vol. 24, no. 7, 2009.

[19] Y. Zhang, “Continuous wave operation of $InAs/InAs_xSb_{1-x}$ midinfrared lasers,” *Appl. Phys. Lett.*, vol. 66, no. 2, pp. 118–120, 1995.

[20] Y. H. Zhang, R. H. Miles, and D. H. Chow, “$InAs–InAs_xSb_{1-x}$ Type-II Superlattice Midwave Infrared Lasers Grown on InAs Substrates,” *IEEE J. Sel. Top. Quantum Electron.*, vol. 1, no. 2, pp. 749–756, 1995.

[21] C. H. Grein, M. E. Flatte, and H. Ehrenreich, “Comparison of Ideal InAs/InAsSb and InAs/InGaSb Superlattice IR Detectors,” in *Proceedings of the Third International Symposium on Long-Wavelength Infrared Detectors and Arrays: Physics and Applications*, 1995, pp. 211–218.

[22] D. Z. Ting *et al.*, “Mid-wavelength high operating temperature barrier infrared detector and focal plane array,” *Appl. Phys. Lett.*, vol. 113, p. 021101, 2018.

[23] Y. H. Zhang, A. Lew, E. Yu, and Y. Chen, “Microstructural properties of $InAs/InAs_xSb_{1-x}$ superlattices and $InAs_xSb_{1-x}$ ordered alloys grown by modulated molecular beam epitaxy,” *J. Cryst. Growth*, vol. 175–176, no. PART 2, pp. 833–837, 1997.

[24] D. H. Chow, R. H. Miles, J. N. Schulman, D. A. Collins, and T. C. McGill, “Type II superlattices for infrared detectors and devices,” *Semicond. Sci. Technol.*, vol. 6, pp. C47–C51, 1991.

[25] S. Maimon and G. W. Wicks, “nBn detector, an infrared detector with reduced dark current and higher operating temperature,” *Appl. Phys. Lett.*, vol. 89, no. 15, 2006.

[26] P. Klipstein and Z. Yaacov, “Depletion-less photodiode with suppressed dark current and method for producing the same,” US 7,798,640 B2, 2010.

[27] H. Kroemer, “Nobel Lecture: Quasi-Electric Fields and Band Offsets: Teaching Electrons New Tricks,” *Rev. Mod. Phys.*, vol. 73, pp. 783–793, 2001.

[28] P. Klipstein, “‘XBn’ Barrier Photodetectors for High Sensitivity and High Operating Temperature Infrared Sensors,” in *Proc. of SPIE Infrared Technology and Applications XXXIV*, 2008, p. 69402U.

[29] W. Shockley and H. J. Queisser, “Detailed balance limit of efficiency of p-n junction solar cells,” *J. Appl. Phys.*, vol. 32, no. 3, pp. 510–519, 1961.

[30] Y. Zhao *et al.*, “Monocrystalline CdTe solar cells with open-circuit voltage over 1 V and efficiency of 17%,” *Nat. Energy*, vol. 1, no. 6, pp. 1–7, 2016.

[31] J. J. Becker *et al.*, “Loss Analysis of Monocrystalline CdTe Solar Cells with 20% Active-Area Efficiency,” *IEEE J. Photovoltaics*, vol. 7, no. 3, pp. 900–905, 2017.

[32] S. Ouendadji, S. Ghemid, N. Bouarissa, H. Meradji, and F. El Haj Hassan, “Ab initio study of structural, electronic, phase diagram, and optical properties of $CdSe_xTe_{1-x}$ semiconducting alloys,” *J. Mater. Sci.*, vol. 46, pp. 3855–3861, 2011.

[33] J. J. Li *et al.*, “CdSe/CdTe type-II superlattices grown on GaSb (001) substrates by molecular beam epitaxy,” *Appl. Phys. Lett.*, vol. 100, no. 12, pp. 15–18, 2012.

[34] N. Matsumura, T. Sakamoto, and J. Saraie, “Growth conditions in molecular beam epitaxy for controlling CdSeTe epilayer composition,” *J. Cryst. Growth*, vol. 251, pp. 602–606, 2003.

[35] E. Yablonovitch, T. Gmitter, J. P. Harbison, and R. Bhat, “Extreme selectivity in the lift-off of epitaxial GaAs films,” *Appl. Phys. Lett.*, vol. 51, no. 26, pp. 2222–2224, 1987.

[36] Z. Y. He, C. M. Campbell, M. B. Lassise, Z. Y. Lin, J. J. Becker, and Y. H. Zhang, “Monolithically integrated CdTe/InSb visible/midwave-infrared two-color photodetectors,” *Infrared Phys. Technol.*, vol. 97, pp. 58–62, 2019.

[37] J. Fan *et al.*, "Molecular beam epitaxial growth of high-reflectivity and broad-bandwidth ZnTe/GaSb distributed Bragg reflectors," *J. Vac. Sci. Technol. B Microelectron. Nanom. Struct.*, vol. 31, no. 3, p. 03C109, 2013.

[38] J. W. Matthews and A. E. Blakeslee, "Defects in epitaxial multilayers," *J. Cryst. Growth*, vol. 27, pp. 118–125, 1974.

[39] N. J. Ekins-Daukes, K. Kawaguchi, and J. Zhang, "Strain-Balanced Criteria for Multiple Quantum Well Structures and Its Signature in X-ray Rocking Curves," *Cryst. Growth Des.*, vol. 2, no. 4, pp. 287–292, 2002.

[40] S. Liu *et al.*, "Impact of substrate temperature on the structural and optical properties of strain-balanced InAs/InAsSb type-II superlattices grown by molecular beam epitaxy," *Appl. Phys. Lett.*, vol. 102, p. 071903, 2013.

[41] H. Li *et al.*, "A calibration method for group V fluxes and impact of V/III flux ratio on the growth of InAs/InAsSb type-II superlattices by molecular beam epitaxy," *J. Cryst. Growth*, vol. 378, pp. 145–149, 2013.

[42] Z.-Y. Lin, S. Liu, E. H. Steenbergen, and Y.-H. Zhang, "Influence of carrier concentration on the minority carrier lifetime in mid-wavelength infrared InAs/InAsSb superlattices," *Appl. Phys. Lett.*, vol. 107, p. 201107, 2015.

[43] B. V. Olson *et al.*, "Identification of dominant recombination mechanisms in narrow-bandgap InAs / InAsSb type-II superlattices and InAsSb alloys," *Appl. Phys. Express*, vol. 103, p. 052106, 2013.

[44] L. Höglund *et al.*, "Influence of radiative and non-radiative recombination on the minority carrier lifetime in midwave infrared InAs/InAsSb superlattices," *Appl. Phys. Lett.*, vol. 103, p. 221908, 2013.

[45] A. E. Brown, N. Baril, D. Zuo, L. A. Almeida, J. Arias, and S. Bandara, "Characterization of n-Type and p-Type Long-Wave InAs/InAsSb Superlattices," *J. Electron. Mater.*, vol. 46, no. 9, pp. 5367–5373, 2017.

[46] Y. Lin *et al.*, "Minority carrier lifetime in beryllium-doped InAs/InAsSb strained layer superlattices," *J. Electron. Mater.*, vol. 43, no. 9, pp. 3184–3190, 2014.

[47] B. C. Connelly *et al.*, "Dependence of minority carrier lifetime of Be-doped InAs/InAsSb type-II infrared superlattices on temperature and doping density," *Phys. Status Solidi Basic Res.*, vol. 253, no. 4, pp. 630–634, 2016.

[48] A. D. Prins, M. K. Lewis, Z. L. Bushell, S. J. Sweeney, S. Liu, and Y. H. Zhang, "Evidence for a defect level above the conduction band edge of InAs/InAsSb type-II superlattices for applications in efficient infrared photodetectors," *Appl. Phys. Lett.*, vol. 106, p. 171111, 2015.

[49] H. S. Kim *et al.*, "Long-wave infrared nBn photodetectors based on InAs/InAsSb type-II superlattices," *Appl. Phys. Lett.*, vol. 101, p. 161114, 2012.

[50] R. Chevallier, A. Haddadi, and M. Razeghi, "Dark current reduction in microjunction-based double electron barrier type-II InAs/InAsSb superlattice long-wavelength infrared photodetectors," *Sci. Rep.*, vol. 7, p. 12617, 2017.

[51] D. Wu, A. Dehzangi, and M. Razeghi, "Demonstration of mid-wavelength infrared nBn photodetectors based on type-II InAs/$InAs_{1-x}Sb_x$ superlattice grown by metal-organic chemical vapor deposition," *Appl. Phys. Lett.*, vol. 115, no. 6, pp. 1–6, 2019.

[52] D. Wu, A. Dehzangi, J. Li, and M. Razeghi, "High performance Zn-diffused planar mid-wavelength infrared type-II InAs/$InAs_{1-x}Sb_x$ superlattice photodetector by MOCVD," *Appl. Phys. Lett.*, vol. 116, no. 16, 2020.

[53] D. Wu, J. Li, A. Dehzangi, and M. Razeghi, "Mid-wavelength infrared high operating temperature pBn photodetectors based on type-II InAs/InAsSb superlattice," *AIP Adv.*, vol. 10, no. 2, 2020.

[54] G. Deng *et al.*, "High operating temperature pBn barrier mid-wavelength infrared photodetectors and focal plane array based on InAs/InAsSb strained layer superlattices," *Opt. Express*, vol. 28, no. 12, p. 17611, 2020.

[55] U. Zavala-Moran *et al.*, "Structural, optical and electrical characterizations of midwave infrared Ga-free type-II InAs/InAsSb superlattice barrier photodetector," *Photonics*, vol. 7, no. 3, p. 76, 2020.

[56] D. Z. Ting *et al.*, "InAs/InAsSb Type-II Superlattice Mid-Wavelength Infrared Focal Plane Array With Significantly Higher Operating Temperature Than InSb," *IEEE Photonics J.*, vol. 10, no. 6, 2018.

[57] D. Zuo *et al.*, "Direct minority carrier transport characterization of InAs/InAsSb superlattice nBn photodetectors," *Appl. Phys. Lett.*, vol. 106, p. 071107, 2015.

[58] B. Deveaud, A. Chomette, B. Lambert, A. Regreny, R. Romestain, and P. Edel, "Picosecond luminescence approach to vertical transport in GaAs/GaAlAs superlattices," *Solid State Commun.*, vol. 57, no. 11, pp. 885–889, 1986.

[59] B. Deveaud, J. Shah, T. C. Damen, and W. T. Tsang, “Capture of electrons and holes in quantum wells,” *Appl. Phys. Lett.*, vol. 52, no. 22, pp. 1886–1888, 1988.

[60] A. Chomette, B. Deveaud, J. Y. Emery, A. Regreny, and B. Lambert, “Vertical transport in GaAs/GaAlAs superlattices observed by photoluminescence,” *Solid State Commun.*, vol. 54, no. 1, pp. 75–78, 1985.

[61] B. Lambert, B. Deveaud, A. Chomette, A. Regreny, and B. Sermage, “Density-dependent transition from electron to ambipolar vertical transport in short-period GaAs- AlGaAs superlattices,” *Semicond. Sci. Technol.*, vol. 4, pp. 513–517, 1989.

[62] B. Deveaud, J. Shah, T. C. Damen, B. Lambert, A. Chomette, and A. Regreny, “Optical Studies of Perpendicular Transport in Semiconductor Superlattices,” *IEEE J. Quantum Electron.*, vol. 24, no. 8, pp. 1641–1651, 1988.

[63] A. Nakamura, K. Fujiwara, Y. Tokuda, T. Nakayama, and M. Hirai, “Dynamics of photoexcited carriers sinking into an enlarged well in a GaAs/AlAs short-period superlattice,” *Phys. Rev. B*, vol. 34, no. 12, pp. 9019–9022, 1986.

[64] F. Piazza, L. Pavesi, A. Vinattieri, J. Martines-Pastor, and M. Colocci, “Influence of miniband widths and interface disorder on vertical transport in superlattice,” *Phys. Rev. B*, vol. 47, no. 16, p. 10625, 1993.

[65] T. Amand *et al.*, “Optical detection of vertical transport in GaAs/$Al_xGa_{1-x}As$ superlattices: Stationary and dynamical approaches,” *Phys. Rev. B*, vol. 47, no. 12, p. 7155, 1993.

[66] B. V. Olson, L. M. Murray, J. P. Prineas, M. E. Flatté, J. T. Olesberg, and T. F. Boggess, “All-optical measurement of vertical charge carrier transport in mid-wave infrared InAs/GaSb type-II superlattices,” *Appl. Phys. Lett.*, vol. 102, p. 202101, 2013.

[67] K. Toprasertpong *et al.*, “Microscopic observation of carrier-transport dynamics in quantum-structure solar cells using a time-of-flight technique,” *Appl. Phys. Lett.*, vol. 107, p. 043901, 2015.

[68] N. Yoon *et al.*, “Modified electron beam induced current technique for In(Ga)As/InAsSb superlattice infrared detectors,” *J. Appl. Phys.*, vol. 122, no. 7, 2017.

[69] B. V Olson *et al.*, “Vertical Hole Transport and Carrier Localization in InAs/$InAs_{1-x}Sb_x$ Type-II Superlattice Heterojunction Bipolar Transistors,” *Phys. Rev. Appl.*, vol. 7, p. 024016, 2017.

[70] A. Yèche *et al.*, "Development of Electron Beam Induced Current for diffusion length determination of VLWIR HgCdTe and MWIR T2SL based photodetectors," *Infrared Phys. Technol.*, vol. 95, pp. 170–176, 2018.

[71] D. R. Rhiger and E. P. Smith, "Carrier Transport in the Valence Band of nBn III–V Superlattice Infrared Detectors," *J. Electron. Mater.*, vol. 14, 2019.

[72] L. K. Casias *et al.*, "Vertical carrier transport in strain-balanced InAs/InAsSb type-II superlattice material," *Appl. Phys. Lett.*, vol. 116, no. 18, p. 182109, 2020.

[73] C.-Y. Tsai, Y. Zhang, Z. Ju, and Y.-H. Zhang, "Study of vertical hole transport in InAs/InAsSb type-II superlattices by steady-state and time-resolved photoluminescence spectroscopy," *Appl. Phys. Lett.*, vol. 116, no. 20, p. 201108, 2020.

[74] P. T. Webster *et al.*, "Absorption properties of type-II InAs/InAsSb superlattices measured by spectroscopic ellipsometry," *Appl. Phys. Lett.*, vol. 106, p. 061907, 2015.

[75] E. H. Steenbergen, J. A. Massengale, G. Ariyawansa, and Y.-H. Zhang, "Evidence of carrier localization in photoluminescence spectroscopy studies of mid-wavelength infrared InAs/$InAs_{1-x}Sb_x$ type-II superlattices," *J. Lumin.*, vol. 178, pp. 451–456, 2016.

[76] P. T. Webster *et al.*, "Measurement of InAsSb bandgap energy and InAs/InAsSb band edge positions using spectroscopic ellipsometry and photoluminescence spectroscopy," *J. Appl. Phys.*, vol. 118, p. 245706, 2015.

[77] S. Safa, A. Asgari, and L. Faraone, "A study of vertical and in-plane electron mobility due to interface roughness scattering at low temperature in InAs/GaSb type-II superlattices," *J. Appl. Phys.*, vol. 114, p. 053712, 2013.

[78] Z.-Y. Lin and Y.-H. Zhang, "Real-time baseline correction technique for infrared time-resolved photoluminesecnce," US 9,927,363 B2, 2018.

[79] E. H. Steenbergen, *InAsSb-based photodetectors*. Elsevier Ltd., 2020.

[80] A. Haddadi, G. Chen, R. Chevallier, A. M. Hoang, and M. Razeghi, "InAs/$InAs_{1-x}Sb_x$ type-II superlattices for high performance long wavelength infrared detection," *Appl. Phys. Lett.*, vol. 105, no. 12, 2014.

[81] A. Haddadi, A. Dehzangi, S. Adhikary, R. Chevallier, and M. Razeghi, "Background-limited long wavelength infrared InAs/$InAs_{1-x}Sb_x$ type-II superlattice-based photodetectors operating at 110 K," *APL Mater.*, vol. 5, no. 3, pp. 1–6, 2017.

[82] D. Z. Y. Ting *et al.*, "A high-performance long wavelength superlattice complementary barrier infrared detector," *Appl. Phys. Lett.*, vol. 95, no. 2, pp. 2007–2010, 2009.

[83] O. O. Cellek, Z.-Y. He, Z.-Y. Lin, H. S. Kim, S. Liu, and Y.-H. Zhang, "InAs/InAsSb type-II superlattice infrared nBn photodetectors and their potential for operation at high temperatures," *Quantum Sens. Nanophotonic Devices X*, vol. 8631, no. February 2013, p. 86311I, 2013.

[84] D. H. Wu, A. Dehzangi, Y. Y. Zhang, and M. Razeghi, "Demonstration of long wavelength infrared type-II InAs/$InAs_{1-x}Sb_x$ superlattices photodiodes on GaSb substrate grown by metalorganic chemical vapor deposition," *Appl. Phys. Lett.*, vol. 112, no. 24, 2018.

[85] A. Kuhn, A. Chevy, and M. J. Naud, "Preparation and some physical properties of magnesium telluride single crystals," *J. Cryst. Growth*, vol. 9, pp. 263–265, 1971.

[86] A. Waag, H. Heinke, S. Scholl, C. R. Becker, and G. Landwehr, "Growth of MgTe and $Cd_{1-x}Mg_xTe$ thin films by molecular beam epitaxy," *J. Cryst. Growth*, vol. 131, no. 3–4, pp. 607–611, 1993.

[87] C. M. Campbell, C.-Y. Tsai, J. Ding, and Y.-H. Zhang, "Epitaxial Lift Off of II-VI Thin Films Using Water-Soluble MgTe," *IEEE J. Photovoltaics*, vol. 9, no. 6, pp. 1834–1838, 2019.

[88] M. B. Lassise, P. Wang, B. D. Tracy, G. Chen, D. J. Smith, and Y.-H. Zhang, "Growth of II-VI/III-V heterovalent quantum structures," *J. Vac. Sci. Technol. B, Nanotechnol. Microelectron. Mater. Process. Meas. Phenom.*, vol. 36, p. 02D110, 2018.

[89] M. B. Lassise, T. T. McCarthy, B. D. Tracy, D. J. Smith, and Y. H. Zhang, "Molecular beam epitaxial growth and structural properties of hetero-crystalline and heterovalent PbTe/CdTe/InSb structures," *J. Appl. Phys.*, vol. 126, p. 045708, 2019.

[90] J. J. Becker *et al.*, "Monocrystalline 1.7-eV-Bandgap MgCdTe Solar Cell with 11.2% Efficiency," *IEEE J. Photovoltaics*, vol. 8, no. 2, pp. 581–586, 2018.

[91] J. Fan, X. Liu, J. K. Furdyna, and Y. H. Zhang, "ZnTe/GaSb distributed Bragg reflectors grown on GaSb for mid-wave infrared optoelectronic applications," *Appl. Phys. Lett.*, vol. 101, no. 12, pp. 1–4, 2012.

[92] M. Konagai, M. Sugimoto, and K. Takahashi, "High efficiency GaAs thin film solar cells by peeled film technology," *J. Cryst. Growth*, vol. 45, no. C, pp. 277–280, 1978.

[93] A. Van Geelen, P. R. Hageman, G. J. Bauhuis, P. C. Van Rijsingen, P. Schmidt, and L. J. Giling, "Epitaxial lift-off GaAs solar cell from a reusable GaAs substrate," *Mater. Sci. Eng. B*, vol. 45, no. 1–3, pp. 162–171, 1997.

[94] J. J. Schermer *et al.*, "High rate epitaxial lift-off of InGaP films from GaAs substrates," *Appl. Phys. Lett.*, vol. 76, no. 15, pp. 2131–2133, 2000.

[95] C. W. Cheng, K. T. Shiu, N. Li, S. J. Han, L. Shi, and D. K. Sadana, "Epitaxial lift-off process for gallium arsenide substrate reuse and flexible electronics," *Nat. Commun.*, vol. 4, p. 1577, 2013.

[96] A. T. J. Van Niftrik, J. J. Schermer, G. J. Bauhuis, P. Mulder, P. K. Larsen, and J. J. Kelly, "A diffusion and reaction related model of the epitaxial lift-off process," *J. Electrochem. Soc.*, vol. 154, no. 11, pp. 629–635, 2007.

[97] J. Scott Ward *et al.*, "Techno-economic analysis of three different substrate removal and reuse strategies for III-V solar cells," *Prog. Photovolt Res. Appl.*, vol. 24, pp. 1284–1292, 2016.

[98] J. J. Schemer, P. Mulder, G. J. Bauhuis, P. K. Larsen, G. Oomen, and E. Bongers, "Thin-film GaAs epitaxial lift-off solar cells for space applications," *Prog. Photovoltaics Res. Appl.*, vol. 13, no. 7, pp. 587–596, 2005.

[99] S. Moon, K. Kim, Y. Kim, J. Heo, and J. Lee, "Highly efficient single-junction GaAs thin-film solar cell on flexible substrate," *Sci. Rep.*, vol. 6, no. July, pp. 1–6, 2016.

[100] C.-Y. Yeh, Z. W. Lu, S. Froyen, and A. Zunger, "Zinc-blende–wurtzite polytropism in semiconductors," *Phys. Rev. B*, vol. 46, no. 16, pp. 10086–10097, 1992.

[101] J. H. Yang, S. Chen, W. J. Yin, X. G. Gong, A. Walsh, and S. H. Wei, "Electronic structure and phase stability of MgTe, ZnTe, CdTe, and their alloys in the B3, B4, and B8 structures," *Phys. Rev. B*, vol. 79, no. 245202, 2009.

[102] S. Adachi, *Properties of Semiconductor Alloys : Group-IV , III – V and II – VI Semiconductors*. 2009.

[103] J. M. Hartmann *et al.*, “CdTe/MgTe heterostructures: Growth by atomic layer epitaxy and determination of MgTe parameters,” *J. Appl. Phys.*, vol. 80, no. 11, pp. 6257–6265, 1996.